ON THE NONLINEAR EVOLUTION OF INTERNAL GRAVITY WAVES

CENTRE FOR NEWFOUNDLAND STUDIES

TOTAL OF 10 PAGES ONLY
MAY BE XEROXED

(Without Author's Permission)

LIREN YAN

ON THE NONLINEAR EVOLUTION OF INTERNAL GRAVITY WAVES

By

©Liren Yan, B.Sc.

A thesis submitted to the School of Graduate

Studies in partial fulfillment of the

requirements for the degree of

Master of Science

Department of Physics

Memorial University of Newfoundland

October, 1993

St. John's Newfoundland Canada

National Library of Canada
Bibliothèque nationale du Canada

Acquisitions and Bibliographic Services Branch
Direction des acquisitions et des services bibliographiques

395 Wellington Street
Ottawa, Ontario
K1A 0N4

395, rue Wellington
Ottawa (Ontario)
K1A 0N4

Your file Votre référence

Our file Notre référence

The author has granted an irrevocable non-exclusive licence allowing the National Library of Canada to reproduce, loan, distribute or sell copies of his/her thesis by any means and in any form or format, making this thesis available to interested persons.

L'auteur a accordé une licence irrévocable et non exclusive permettant à la Bibliothèque nationale du Canada de reproduire, prêter, distribuer ou vendre des copies de sa thèse de quelque manière et sous quelque forme que ce soit pour mettre des exemplaires de cette thèse à la disposition des personnes intéressées.

The author retains ownership of the copyright in his/her thesis. Neither the thesis nor substantial extracts from it may be printed or otherwise reproduced without his/her permission.

L'auteur conserve la propriété du droit d'auteur qui protège sa thèse. Ni la thèse ni des extraits substantiels de celle-ci ne doivent être imprimés ou autrement reproduits sans son autorisation.

ISBN 0-315-91587-0

Canada

Abstract

The purpose of this thesis is to compare the nonlinear evolution of internal gravity waves obtained from a fully nonlinear primitive equation model with the evolution predicted by weakly nonlinear theories (i.e., the KdV and mKdV equations). In order to focus on the nonlinear evolution, we consider the idealized case of an inviscid, incompressible Boussinesq fluid of constant depth with simple stratifications. In such an environment, the evolution of internal waves is theoretically analyzed up to second order in amplitude by the method of asymptotic expansion following Lee & Beardsley [1974]. The resulting governing equation is the mKdV equation. Meanwhile, the evolution of the same system is simulated by a fully nonlinear, inviscid numerical model. The model is believed to be reliable (Lamb [1993 a,b]) and thus can be used to quantitatively verify the derived theory. The theory is compared against the model results. An initial depression is generated and the nonlinear steepening of the wave front and its subsequent evolution into an undular bore is investigated for different stratifications and wave amplitudes. It is found that the theory is in very good quantitative agreement with the model results. The mKdV equation generally improves the first-order KdV results for waves with nondimensional amplitude ϵ up to 0.07. For small waves with $\epsilon < 0.02$, the second order nonlinearity is not crucial. The

mKdV equation is not appropriate for waves with ϵ larger than 0.07. These results provide further evidence that the fully nonlinear primitive equation model is reliable and give some indication of when the KdV and mKdV equations correctly predict the wave evolution. It is also shown that after the undular bore begins to form, rotation has a minor effect on its subsequent evolution.

Acknowledgements

I am grateful to the following people who gave me guidance, support and assistance during the course of this thesis work.

1. Dr. K. G. Lamb, my supervisor, introduced me to the field of nonlinear internal gravity waves. He outlined the research idea, helped me to understand and to analyze the physics of the present topic. His continual guidance contributed a great deal to the completion of my thesis work. Dr. Lamb also kindly provided me with financial support throughout the course of this work (a part of the support is from NSERC Operating/Research Grants awarded to K. G. Lamb).

2. Dr. R. J. Greatbatch offered many enlightening advices when I encountered difficulties, and generously supported me during the first two years (a part of the support is from NSERC Operating/Research Grants awarded to R. J. Greatbatch).

3. Dr. R. J. Greatbatch, Dr. A. E. Hay and Dr. J. de Bruyn provided some very constructive suggestions in making this thesis clearer and more concise.

4. A. Goulding and P. Fardy gave me a lot of help with the computer system. H. Halide shared with me his experience of using Latex, Xfig, etc.

5. School of Graduate Studies and Department of Physics provided generous financial assistance for this work through Graduate Fellowship and Departmental assistantship, respectively.

Contents

List of Figures

List of Tables

Chapter 1

Introduction

Internal gravity waves (denoted as IGWs hereafter) occur within subsurface layers of the ocean where the water is stratified because of temperature and salinity variations. These waves play a significant role in transporting momentum and energy within the ocean and can be an important source of mixing. It has been realized that IGWs and their side effects deserve careful attention, for they can significantly influence ocean current measurement, underwater navigation, antisubmarine warfare operations and even the feeding of marine animals (see Osborne & Burch [1980]).

Over the past two decades, there have been many reports of observations of large internal waves occuring in the ocean. These waves are usually in the form of interfacial undular bores, solitons or solitary waves, typified by large amplitude and

steepness. Most of them are generated by intense tidal flow over abrupt underwater topography, and propagate in packets of several large amplitude waves ranked in order with the largest wave leading the group. Halpern [1971 a,b], Haury *et al.* [1979] and Chereskin [1983] reported such wave formations observed in Massachussetts Bay. Farmer & Smith [1980 a,b] in Knight Inlet, Osborne & Burch [1980] in the Andaman Sea and Apel *et al.* [1985] in the Sulu Sea and Sandstrom & Elliott [1984] on the Scotian Shelf all observed similar wave patterns evolving from either a thermocline depression or a lee wave train formed by subcritical tidal flow near a sea sill. There are also laboratory experiments which reproduced similar wave formations in a two-layer fluid system, e.g. Maxworthy [1979], Koop & Butler [1981], Segur & Hammack [1982]. La Violette *et al.* [1990] discussed photographs taken over the Georges Bank from the U.S. space shuttles, which clearly reveal the surface signatures of internal wave packets propagating away from the bank edge.

At the same time, theoretical investigations of IGWs have been carried out with various focuses. In the framework of weakly nonlinear shallow water theory, Benney [1966], Lee & Beardsley [1974], Ono [1975] , Kubota [1978] derived nonlinear theoretical models for IGW evolution in stratified and/or sheared fluid of shallow, finite and infinite depths, respectively. These theories say that the evolution of weakly nonlinear IGWs is governed by equations of KdV type (KdV stands for the

Korteweg-de Vries equation), in which the associated nonlinearity and dispersion are totally determined by the environmental equilibrium state. Lee & Beardsley [1974] qualitatively reproduced the main features of tidally generated large amplitude wave trains observed in Massachussetts Bay. Maxworthy [1979], Farmer & Smith [1980] and Hibiya [1986] investigated the generation mechanism of internal wave trains through tidal-topographic interaction. Koop & Butler [1981], Segur & Hammack [1982], and Cummins & LeBlond [1984] tested the range of validity of the KdV, Benjamin-Ono and Kubota solitary solutions against experiments and observations of internal solitary waves, focusing on the wave shape and amplitude-wavelength scaling relationship. They found that the KdV theory has a larger range of validity than the theory might imply; in particular, it is not strictly limited to shallow water. Liu *et al.* [1985] modified Kubota's model by incorporating spreading and dissipation effects into the model, thus formulated the evolution of the internal packets observed in Sulu Sea. The comparison shows that the simulated propagation speed of the front, the number of solitons, their amplitudes and lengths are in good qualitative agreement with the data.

As pointed out by Ostrovsky & Stepanyants [1989], a thorough theoretical description of IGW evolution processes in real oceans is a rather difficult problem. The KdV-type theories used are two dimensional and include only first or possibly sec-

ond order nonlinear and dispersive effects (and possibly parameterized radiation and dissipation effects). In contrast, the observed waves are three dimensional and are affected by many hydrodynamical factors, such as the variations of shear, stratification, topography, radiation, bottom/eddy dissipation, tide, etc. It is also difficult to follow the space-time evolution of a wave for comparison with theories. This makes good quantitative comparisons difficult. Thus, the comparisons are only qualitative. Although it is possible now to obtain a general pattern of propagating IGWs from aircraft and satellites, reliable simultaneous hydrological data are still rarely available for the formulation of theoretical models. All of these present significant obstacles to the understanding of the nature of observed IGW motions.

Numerical modelling of IGW evolution in an idealized ocean could be a preliminary solution of the problem. By taking into consideration important factors one by one, their roles in IGW evolution can be better understood. A reliable model can be used to quantitatively verify the existing theories which are usually derived under idealized conditions. In contrast, field measurements are temporally or spatially sparse and affected by a number of physical processes. Hence, they are only useful for qualitative comparisons. There are also some advantages of numerical modelling over laboratory experiments for the cases considered here. For example, a numerical model can be run in an inviscid mode or at large, realistic Reynolds numbers. It also

allows greater control of the physical processes that can influence the wave evolution, and can incorporate more realistic background conditions. In addition, a complete data set can be obtained.

In this thesis work, we investigate the nonlinear evolution of an isopycnal depression. The depression steepens because of nonlinearity and then evolves into an undular bore through dispersive effects. This process is simulated with a fully nonlinear primitive equation model (Lamb [1993 a,b]) which solves the inviscid, incompressible Boussinesq equations. The KdV and mKdV equations appropriate to these equations are then derived following Benney [1966] and Lee & Beardsley [1974]. The evolution predicted by the KdV and mKdV equations is then compared with the evolution given by the fully nonlinear primitive equation model. Any differences in the evolutions can only be due to the approximations made in deriving the KdV and mKdV equations, to numerical error in numerically solving the KdV and mKdV equations, or to numerical error in the model. The numerical errors can be reduced by sufficiently high resolution. The theoretical evolutions are compared with the model results for several hydrological backgrounds and wave amplitudes, and also for a case with rotation included. In order to see the improvement made by mKdV, comparisons between the model and the first-order KdV theory are also given.

In chapter 2, the numerical model used is briefly introduced, and then the

domain geometry and the hydrological environment, in which the model is run and the theory is derived, are given. In chapter 3, after a brief review of long wave theories, we give a detailed derivation of the mKdV equation, together with the associated vertical mode functions and coefficients. Then, the numerical method used to solve the KdV and mKdV equations is described. The theory is compared with the model in chapter 4, along with in-situ and general discussions. The conclusions are in Chapter 5.

Chapter 2

Numerical Simulation

In this chapter we briefly introduce the numerical model which has been used in this study to simulate IGWs. Weakly nonlinear theoretical results will be compared to the fully nonlinear results obtained with this model. This model was developed by Kevin Lamb [1993 a,b] and will be referred to as IGWsim in this thesis (standing for Internal Gravity Wave Simulation). The model is run within a fixed physical domain and for different background states. Some of the results will be given later in this chapter as examples.

2.1 The Numerical Model

IGWsim solves the time dependent, inviscid, incompressible Boussinesq equations

$$\vec{U}_t + (\vec{U} \cdot \vec{\nabla})\vec{U} = -\vec{\nabla}p - \rho\vec{g}, \tag{2.1}$$

$$\rho_t + \vec{U} \cdot \vec{\nabla}\rho = 0, \tag{2.2}$$

$$\vec{\nabla} \cdot \vec{U} = 0. \tag{2.3}$$

Here $\vec{U}$ is the velocity vector with horizontal and vertical components (u, w). (x, z) are the corresponding coordinates with z measured positive upward and $\vec{\nabla}$ is the gradient operator $(\partial/\partial x, \partial/\partial z)$. The fluid density is given by $\rho_0(1+\rho)$ and $\rho_0(gz+p)$ is the pressure. $\vec{g}$ is the vector $(0, g)$ with g being the gravitational acceleration. Note that $\rho_0 g$ balances the constant hydrostatic part of the pressure gradient, and the Boussinesq approximation removes the factor of $1 + \rho$ on the left side of (2.1).

The equations are solved in a two dimensional domain bounded below by a given topography and above by a rigid lid as shown in figure 2.1. At the upper and lower boundaries inviscid boundary conditions (no normal flow) are used. The flow is forced by specifying $\vec{U}_t$ at the left boundary. An outflow boundary condition is specified at the right boundary (see Bell & Marcus [1992], Lamb [1993 a,b]).

The numerical method used to solve these equations is the second-order pro-

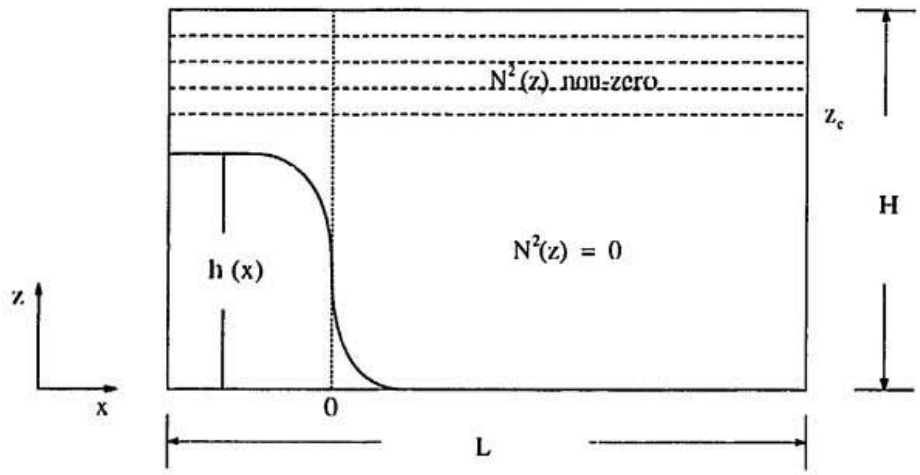

Figure 2.1: The sketch of physical domain.

jection method developed by Bell *et al.* [1989 a,b] and Bell & Marcus [1992]. The theory of the method is based on the following:

i. Hodge decomposition: Any vector field $\vec{V}$ can be decomposed into a divergence free component and a gradient part, i.e.

$$\vec{V} = \vec{V}^d + \vec{\nabla}\varphi, \tag{2.4}$$

where $\vec{\nabla} \cdot \vec{V}^d = 0$ and φ is a scalar field. This decomposition is unique given appropriate boundary conditions for $\vec{V}^d$ (e.g., $\vec{V}^d \cdot \vec{n} = 0$).

By rewriting the momentum equation (2.1) as

$$\vec{U}_t + \vec{\nabla}p = \vec{V} \equiv -(\vec{U} \cdot \vec{\nabla})\vec{U} - \rho\vec{g}, \tag{2.5}$$

one sees that, with suitable boundary conditions and because of equation (2.3, $\vec{U}_t$ is

the divergence-free component of the vector $\vec{V}$ and the pressure gradient $\vec{\nabla}p$ is the corresponding gradient part.

ii. Orthogonality: For any vector $\vec{V}$ and scalar φ, we have

$$\iint_A \varphi\vec{\nabla}\cdot\vec{V}dA = -\iint_A \vec{V}\cdot\vec{\nabla}\varphi dA + \oint_{\partial A}\varphi\vec{V}\cdot\vec{n}dl, \tag{2.6}$$

where A is the computational domain, ∂A its boundary and l is the element length of the boundary. In particular, for a divergence-free $\vec{V}^d$, we have

$$\iint_A \vec{V}^d\cdot\vec{\nabla}\varphi dA = \oint_{\partial A}\varphi\vec{V}^d\cdot\vec{n}dl. \tag{2.7}$$

Thus, if $\vec{V}^d$ has a zero Dirichlet boundary condition, $\vec{V}^d$ and $\vec{\nabla}\varphi$ are orthogonal within the domain.

For our problem, if a divergence-free boundary velocity field satisfying the given boundary condition is subtracted from the momentum equation, (2.5) reduces to

$$\vec{U}_t^I + \vec{\nabla}p = \vec{V}^I = \vec{V} - \vec{U}_t^B, \tag{2.8}$$

where $\vec{U}_t^I = \vec{U}_t - \vec{U}_t^B$ has zero Dirichlet boundary condition. According to the above, $\vec{U}_t^I$ is orthogonal to $\vec{\nabla}p$.

iii. Projection: The projection is defined by specifying a basis of divergence-free vectors $\vec{\Psi}^n$ with zero Dirichlet boundary. Then $\vec{\Psi}^n$ is orthogonal to $\vec{\nabla}p$. From (2.8)

we have

$$\iint_A \vec{\Psi}^n \cdot \vec{U}_t^I dA = \iint_A \vec{\Psi}^n \cdot \vec{V}^I dA. \tag{2.9}$$

(2.9) indicates that the orthogonality property eliminates the scalar gradient part entirely from the problem. It will be seen that because of this property boundary conditions for the pressure are not required in solving this problem.

Now suppose $\vec{U}_t^I$ has k dimensions. It then can be written as

$$\vec{U}_t^I = \sum_{n=1}^{k} \sigma_n \vec{\Psi}^n. \tag{2.10}$$

Substituting into (2.9) gives a linear system with k equations and k unknown $\sigma's$, i.e.,

$$\sum_{m=1}^{k} \sigma_m \iint_A \vec{\Psi}^m \cdot \vec{\Psi}^n dA = \iint_A \vec{\Psi}^n \cdot \vec{V}^I dA, \tag{2.11}$$

with n going from 1 to k. Therefore, for any known $\vec{V}^I$, we can determine the σ_m's and consequently the divergence free component $\vec{U}_t^I$. This is what the so called projection means. Let P denote this projection operation. Then we express the projection as

$$P(\vec{V}^I) = \vec{U}_t^I. \tag{2.12}$$

Our interior divergence-free velocity field $\vec{U}_t^I$ is obtained by projecting $\vec{U}_t - \vec{U}_t^B$. The desired $\vec{U}_t$ is then recovered by adding back the known divergence-free boundary field $\vec{U}_t^B$.

In the following, a brief overview of the method is given. One should consult the above mentioned papers for more details.

2.1.1 Grid scheme

To begin with, we first introduce the grid scheme used (figure 2.2), which provides the most natural setting for the handling of the convective terms in the system.

$\vec{U}, \rho$ and $\vec{\nabla} p$ are defined at the vector grid points which include the interior vector grid points located at cell centres and the boundary vector grid points at the midpoints of cell edges lying along the boundaries. The latter are used to specify boundary conditions. The scalar grid points are located at cell corners where scalar fields (such as $\vec{\nabla} \cdot \vec{U}$ and the χ^n defined later) are defined. The exception to this is ρ which is given at the vector grid points.

2.1.2 Transformation

The model calculation is not carried out in the above domain. Instead, the physical domain in (x, z) space is mapped onto a rectangular computational domain in (ξ, η) space so that any given quadrilateral grid cell in (x, z) becomes a unit square cell in (ξ, η). This makes the model more flexible in that it can take any grid mesh given in

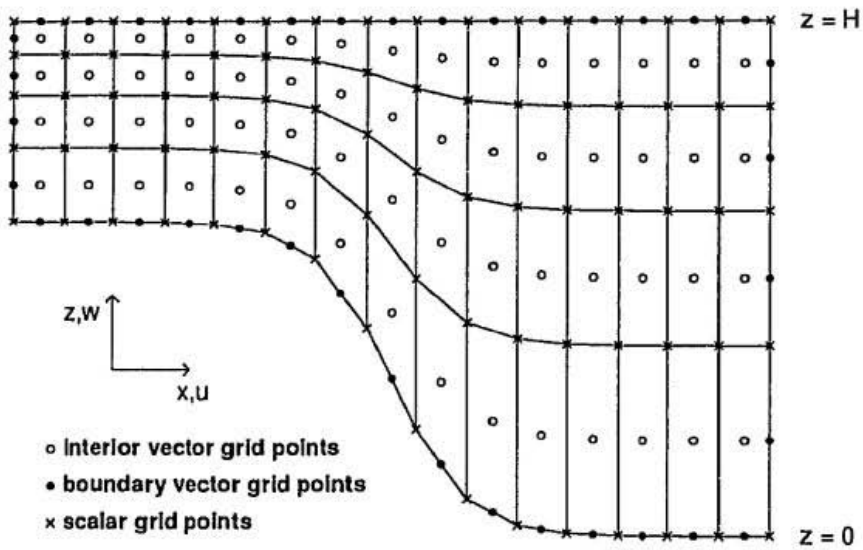

Figure 2.2: Grid scheme with quadrilateral grid cells in (x, z) space.

(x, z) and do the calculation in the same way on the unit square grid mesh in (ξ, η). This is done by a coordinate transformation

$$x = x(\xi, \eta), \tag{2.13}$$

$$z = z(\xi, \eta). \tag{2.14}$$

The corresponding Jacobian is defined as

$$J = \frac{\partial(x, z)}{\partial(\xi, \eta)} = \begin{vmatrix} x_\xi & z_\xi \\ x_\eta & z_\eta \end{vmatrix} \tag{2.15}$$

From (2.13) and (2.14) we have

$$\begin{pmatrix} \xi_x & \eta_x \\ \xi_z & \eta_z \end{pmatrix} = \frac{1}{J} \begin{pmatrix} z_\eta & -z_\xi \\ -x_\eta & x_\xi \end{pmatrix} = \frac{T^t}{J}, \tag{2.16}$$

where T is defined as

$$T = \begin{pmatrix} z_\eta & -x_\eta \\ -z_\xi & x_\xi \end{pmatrix}. \tag{2.17}$$

The relations between the original and transformed divergence operator is

$$\begin{aligned} \vec{\nabla} \cdot \vec{U} &= \frac{1}{J}(z_\eta u_\xi + x_\xi v_\eta - x_\eta u_\eta - z_\xi v_\xi) && (2.18) \\ &= \frac{1}{J} \hat{\nabla} \cdot T\vec{U}. && (2.19) \end{aligned}$$

Therefore, the original equation system in (x, z) reduces to the following in (ξ, η):

$$\begin{aligned} \vec{U}_t + \frac{1}{J}(\vec{U} \cdot \hat{\nabla})\vec{U} &= -\vec{\nabla} p - \rho \vec{g}, && (2.20) \\ \rho_t + \frac{1}{J}\vec{U} \cdot \hat{\nabla}\rho &= 0, && (2.21) \\ \hat{\nabla} \cdot \vec{U} &= 0, && (2.22) \end{aligned}$$

where $\hat{\nabla} \equiv (\partial/\partial\xi, \partial/\partial\eta)$ and

$$\vec{U} = T\vec{U}. \tag{2.23}$$

Note that $\vec{\nabla} p = (p_x(\xi, \eta), p_z(\xi, \eta))$, instead of $\frac{T^t}{J}\hat{\nabla} p$, has been used, since only the pressure gradient is needed in the calculation.

Only the coordinates of the dual grid in (x, z) space need to be provided. The appropriate differences of the dual grid coordinates are used to evaluate the elements of the T matrix and the grid point coordinates of (ξ, η). This ensures that the method preserves a uniform flow (see Bell *et al.* [1989b]).

2.1.3 Numerical Algorithm

To solve the above system, we rewrite the momentum equation (2.20) in the decomposition form as in (2.5):

$$\vec{U}_t + \vec{\nabla} p = \vec{V}, \tag{2.24}$$

where

$$\vec{V} = -\frac{1}{J}(\vec{U} \cdot \vec{\nabla})\vec{U} - \rho\vec{g},$$

then subtract off a boundary velocity field $\vec{U}_t^B$ and project $\vec{V} - \vec{U}_t^B$:

$$\vec{U}_t = P(\vec{V} - \vec{U}_t^B) + \vec{U}_t^B. \tag{2.25}$$

According to the theory, (2.25) means that the non-divergence-free vector $\vec{V} - \vec{U}_t^B$ is decomposed by the projection into a divergence-free component $\vec{U}_t - \vec{U}_t^B$ which has zero Dirichlet boundary condition, and a scalar gradient part $\vec{\nabla} p$. The desired updating velocity field is then recovered by adding back the boundary field $\vec{U}_t^B$. The orthogonal property of the projection P eliminates the pressure entirely from the

system, and the equations are integrated as a velocity evolution system within the space of a divergence-free vector field. This theoretically explains why no boundary condition is needed for the pressure.

Directly discretizing (2.25) using a second-order differencing is possible, but the resulting linear system is poorly conditioned (see Bell *et al.* [1989]). Therefore, the following approach is used to treat the nonlinear convective terms.

In order to have a scheme which is second-order in time we discretize (2.25) using a centered time differencing. The nonlinear convective terms at the half time step $n + \frac{1}{2}$ are calculated using an explicit second-order Godunov procedure (a modified Piecewise Parabolic Method) described by Bell *et al.* [1989b]. Values at the midpoints of the cell edges at the half time level are evaluated by Taylor expansions of the known values at the cell centres at time n. The time derivatives appearing in the Taylor expansions are then eliminated by using the governing equation, thus time lagged pressure gradients are introduced here (this is the only place where the pressure gradient is used). Two kinds of spatial derivatives appear in the resulting expressions: normal and transverse derivatives (with respect to the cell edges). The normal derivatives are evaluated using monotonicity-limited central differences which prevent introducing new maxima or minima into the flow field, while the transverse derivatives are evaluated via a modified upwind scheme. For each cell edge there are

two cell centres to extrapolate from. The appropriate choice is the cell centre upwind of the cell edge. With the values at the cell edges known at the half time level, the convective terms are calculated using centred differencing in space. An example of this procedure is shown below for the term $[\vec{U}\cdot\vec{\nabla}u]^{n+\frac{1}{2}}$ (the transformation is dropped here, since it introduces only coefficients and makes no difference to the algorithm. It should also be noted that $\vec{U}^{n+\frac{1}{2}}$, which is the extrapolation from the divergence-free velocity field at time n and involves lagged pressure, is not divergence-free).

$[\vec{U}\cdot\vec{\nabla}u]^{n+\frac{1}{2}}$ is discretized as

$$
\begin{aligned}
&(\vec{U}\cdot\vec{\nabla}u)^{n+\frac{1}{2}} \\
&= \frac{1}{2}(u^{n+\frac{1}{2}}_{i+\frac{1}{2},j}+u^{n+\frac{1}{2}}_{i-\frac{1}{2},j})\frac{u^{n+\frac{1}{2}}_{i+\frac{1}{2},j}-u^{n+\frac{1}{2}}_{i-\frac{1}{2},j}}{\Delta x}+\frac{1}{2}(w^{n+\frac{1}{2}}_{i,j+\frac{1}{2}}+w^{n+\frac{1}{2}}_{i,j-\frac{1}{2}})\frac{u^{n+\frac{1}{2}}_{i,j+\frac{1}{2}}-u^{n+\frac{1}{2}}_{i,j-\frac{1}{2}}}{\Delta z} \qquad (2.26)
\end{aligned}
$$

Note that the centred differencing used here indicates the second order accuracy in space.

Extrapolating from $\vec{U}^n_{i,j}$ (see figure 2.3) gives four mid-edged, half time values for each $\vec{U}^n_{i,j}$, which are denoted by L, R, B, T (for left, right, bottom and top, respectively). For instance, extrapolating from the left, $u^{n+\frac{1}{2},L}_{i+\frac{1}{2},j}$ is given by

$$
\begin{aligned}
u^{n+\frac{1}{2},L}_{i+\frac{1}{2},j} &= u^n_{ij}+\frac{\Delta x}{2}u^n_{x,ij}+\frac{\Delta t}{2}u^n_{t,ij} \\
&= u^n_{ij}+\frac{\Delta x}{2}u^n_{x,ij}+\frac{\Delta t}{2}(-u^n_{ij}u^n_{x,ij}-w^n_{ij}u^n_{z,ij}-p^{n-\frac{1}{2}}_{x,ij})
\end{aligned}
$$

$$= u_{ij}^n + \left(\frac{\Delta x}{2} - \frac{\Delta t}{2} u_{ij}^n\right) u_{x,ij}^n - \frac{\Delta t}{2} w_{ij}^n u_{z,ij}^n - \frac{\Delta t}{2} p_{x,ij}^{n-\frac{1}{2}}. \qquad (2.27)$$

The governing equation for u has been used to eliminate the time derivative. This introduces the time lagged pressure gradient.

The normal derivative and transverse derivative $u_{x,ij}^n$ and $u_{z,ij}^n$ in (2.27) are treated in different ways as mentioned before. Details will not be given here. Readers should refer to Bell *et al.* [1989 a,b]. The purpose of the treatments is to prevent introducing spurious oscillations or instabilities, even for discontinuous data. The normal derivatives involve central differencing, which again leads to the second order accuracy in space.

The values of, for instance, $(u_{i+\frac{1}{2},j}^{n+\frac{1}{2}}, w_{i+\frac{1}{2},j}^{n+\frac{1}{2}})$ are chosen from the corresponding extrapolated mid-edge values by the following:

$$u_{i+\frac{1}{2},j}^{n+\frac{1}{2}} = \begin{cases} u_{i+\frac{1}{2},j}^{n+\frac{1}{2},L} & \text{if} \quad u_{i+\frac{1}{2},j}^{n+\frac{1}{2},L} \geq 0 \quad \text{and} \quad u_{i+\frac{1}{2},j}^{n+\frac{1}{2},L} + u_{i+\frac{1}{2},j}^{n+\frac{1}{2},R} \geq 0 \\ 0 & \text{if} \quad u_{i+\frac{1}{2},j}^{n+\frac{1}{2},L} < 0 \quad \text{and} \quad u_{i+\frac{1}{2},j}^{n+\frac{1}{2},R} > 0 \\ u_{i+\frac{1}{2},j}^{n+\frac{1}{2},R} & \text{otherwise} \end{cases} \qquad (2.28)$$

$$w_{i+\frac{1}{2},j}^{n+\frac{1}{2}} = \begin{cases} w_{i+\frac{1}{2},j}^{n+\frac{1}{2},L} & \text{if} \quad u_{i+\frac{1}{2},j}^{n+\frac{1}{2}} > 0 \\ w_{i+\frac{1}{2},j}^{n+\frac{1}{2},R} & \text{if} \quad u_{i+\frac{1}{2},j}^{n+\frac{1}{2}} < 0 \\ \frac{1}{2}(w_{i+\frac{1}{2},j}^{n+\frac{1}{2},L} + w_{i+\frac{1}{2},j}^{n+\frac{1}{2},R}) & \text{if} \quad u_{i+\frac{1}{2},j}^{n+\frac{1}{2}} = 0 \end{cases} \qquad (2.29)$$

It is seen that at L, R edges, the vertical component w is treated as an advected

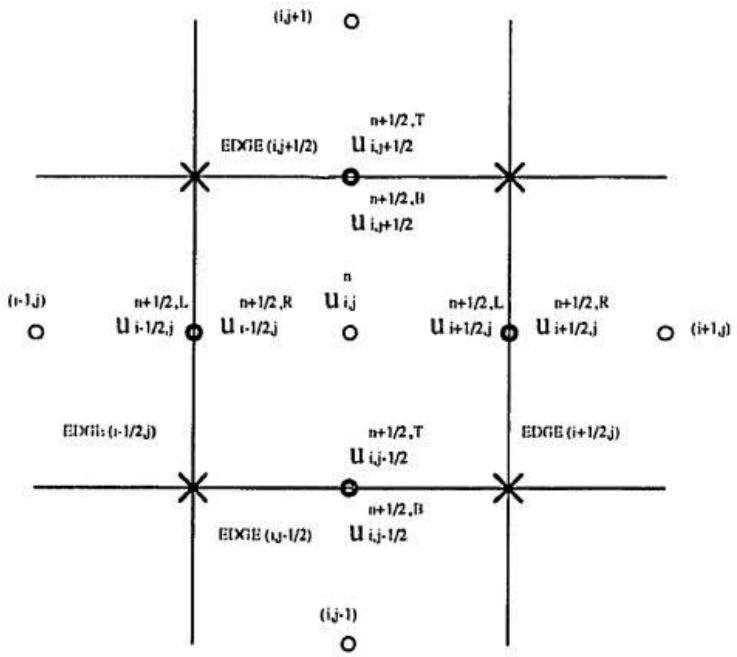

Figure 2.3:
L denotes the extrapolation of (u_{ij}^n, v_{ij}^n) to the left side of edge $(i+\frac{1}{2}, j)$;
R denotes the extrapolation of (u_{ij}^n, v_{ij}^n) to the right side of edge $(i-\frac{1}{2}, j)$;
B denotes the extrapolation of (u_{ij}^n, v_{ij}^n) to the bottom side of edge $(i, j+\frac{1}{2})$;
T denotes the extrapolation of (u_{ij}^n, v_{ij}^n) to the top side of edge $(i, j-\frac{1}{2})$.

tracer. If $u^{n+\frac{1}{2}}_{i+\frac{1}{2},j} > 0$, $w^{n+\frac{1}{2}}_{i+\frac{1}{2},j}$ is only affected by those values on the left side of the edges. Thus, it is natural to set it equal to $w^{n+\frac{1}{2},L}_{i+\frac{1}{2},j}$ which is extrapolated from the left side.

By the substitution of the obtained mid-edge half-time values into (2.26), the velocity convective term is evaluated. The density advective term is calculated in a similar manner.

The velocity, density and pressure are then updated by solving the following time forwarding equations

$$\frac{\rho^{n+1}-\rho^n}{\Delta t} = -\frac{1}{J}(\vec{U}\cdot\tilde{\nabla}\rho)^{n+\frac{1}{2}} \tag{2.30}$$

$$\begin{aligned}\frac{\vec{U}^{n+1}-\vec{U}^n}{\Delta t} &= P(\vec{V}^{n+\frac{1}{2}}-\vec{U}^B_t)+\vec{U}^B_t \\ &= P\left(\frac{1}{J}(\vec{U}\cdot\tilde{\nabla}\vec{U})^{n+\frac{1}{2}}-\frac{\rho^{n+1}-\rho^n}{2}\vec{g}-\vec{U}^B_t\right)+\vec{U}^B_t \end{aligned} \tag{2.31}$$

$$\vec{\nabla}p^{n+\frac{1}{2}} = (I-P)(\vec{V}^{n+\frac{1}{2}}-\vec{U}^B_t). \tag{2.32}$$

Since centred time differencing is used, the scheme is also second order accurate in time. The flow field influences the density field through advection, and the influenced density field feeds back into the velocity field. This coupling is reflected in (2.30) and (2.31). Since the hydrostatic approximation has not been made, the pressure is affected by both the velocity and density as expressed in (2.32).

The projection is then discretized, which involves solving a linear equation

system for the σ_m's defined in (2.11). The associated basis of discretized divergence-free vectors which are zero on Dirichlet boundary is specified by

$$\vec{\Psi}^n \equiv \tilde{\nabla}^{\perp}\chi^n \equiv (\chi^n_\eta, -\chi^n_\xi) \tag{2.33}$$

where n goes from 1 to $I(J-1)$, χ^n is the basis of discretized scalar fields with zero Dirichlet boundary, which has a constant value on one scalar point indexed by n and is zero elsewhere.

Thus, the discretized projection can be rewritten as

$$P\vec{\sigma} = \vec{S}, \tag{2.34}$$

where P is the projection matrix given by $P_{mn} = (\vec{\Psi}^m, \vec{\Psi}^n)_v$, $\vec{\sigma}$ represents $I(J-1)$ unknowns, and $\vec{S}$ is $(\vec{\Psi}^n, \vec{V}^{n+\frac{1}{2}} - \vec{U}^B_t)_v$. (Readers should refer to Bell *et al.* [1989 a,b] for more details about the dimension of the discretized velocity field, the definitions of discretized gradient, divergence and vector inner production, etc).

P is a positive, symmetric matrix which is block tridiagonal. (2.34) is solved using a standard block tridiagonal solver (Golub & Van Loan [1989]). Note that the P matrix is fixed once calculated, since the basis vectors are independent of time.

The system is updated by (2.30) to (2.32). For the explicit Godunov scheme used, a linear constant-coefficient analysis shows that for stability, the time step must

satisfy a CFL condition (Courant-Friedrichs-Lewy condition), i.e.

$$dt \leq s\ min\left(\frac{1}{\tilde{u}}, \frac{1}{\tilde{v}}.\right) \tag{2.35}$$

where s is a safety factor taken as 0.5. The stiffness of the gravitational forcing term requires a more restrictive time step. In practice, for our nonlinear model, dt is taken considerably smaller than the value given by the standard CFL estimate.

2.2 Domain geometry and background state

2.2.1 Domain geometry

The two dimensional physical domain, as shown in figure 2.1, is confined by a rigid upper boundary at $z = H$ and a bank edge topography at $z = h(x)$. The bank edge is simulated by a hyperbolic function given by

$$h(x) = a_1(1 - \tanh a_2(x - a_3)), \tag{2.36}$$

where a_1 is half the height of the bank top, a_2 is a slope parameter and a_3 is the centre of the bank edge. z_c is the height above which the fluid is significantly stratified.

For such a system, the controlling parameters are the geometric ratio a_1/H, the bank slope a_2, and the dynamical parameter $G = Hg/U^2$ (G is the square of the

inverse Froude number for SGWs. It has no direct relevance to supercriticality or subcriticality of IGWs), which will appear in the non-dimensional equation system (see chapter 3), where U is the velocity scale. For fixed ratios and different U and H, if G is the same, the flow pattern will be the same but on a different time scale.

In our runs, the geometric parameters themselves are usually fixed as $H = 360\,\mathrm{m}$, $L = 80\,\mathrm{km}$, $z_c = 260\,\mathrm{m}$, $a_1 = 220\,\mathrm{m}$, $a_2 = 0.000375$ and $a_3 = 0.25 * L$. The only parameter controlling the flow is the dynamical G, which depends on U only (since H is fixed). Therefore, different U will result in different flow patterns.

Our primary purpose in specifying a bank geometry is to generate an initial wave through flow-topography interaction. Therefore, when the bank can not produce a desired initial wave, we will use a flat bottom and artificially specify an initial wave.

2.2.2 Background state

Two kinds of density profiles are used in the present study. For convenience, instead of giving the density profiles, we present below the associated stratifications defined by

$$N^2(z) = -\bar{\rho}_z g. \tag{2.37}$$

The first is given by a hyperbolic function of the form

$$N_1^2(z) = \frac{N_0^2(1 + \tanh q(z - z_c))}{2}, \qquad 0 \le z \le H \tag{2.38}$$

where q is a slope parameter and N_0^2 is the characteristic value of the stratification which is set to $0.002/s^2$. z_c is the height above which the fluid is significantly stratified. When $q \to \infty$, $N_1^2(z)$ approaches a stepwise function. Figure 2.4 (a) shows $N_1^2(z)$ with a small $q = 0.007$ and a large $q = 10$. The model is run for both q values. The mode-one baroclinic phase speed associated with $N_1^2(z)$ is about 2.5 m/s for both q values, while the mode-two speed is about 0.95 m/s.

Secondly, we consider a density stratification of the form

$$\begin{aligned} N_2^2(z) &= g\left\{ \frac{0.0034}{35} \exp \frac{z - H + 10}{35} - \frac{0.9(z - H + 80)}{5\left[1 + \frac{(z-H+80)^2}{5000}\right]^2} \right. \\ &= \left. + \frac{0.05(z - H + 200)}{\left[1 + \frac{(z-H+200)^2}{2000}\right]^2} \right\}, \end{aligned} \tag{2.39}$$

which is shown in figure 2.4 (b). The mode-one baroclinic phase speed associated with $N_2^2(z)$ is about 1 m/s, and the mode-two phase speed is about 0.5 m/s.

These two stratification profiles approximate observed density profiles on the Scotian Shelf ($N_1^2(z)$ with small q) and at the edge of Georges Bank ($N_2^2(z)$) where large amplitude nonlinear waves have been observed (Sandstrom & Elliott [1984], Loder *et al.* [1992] and La Violette *et al.* [1990]).

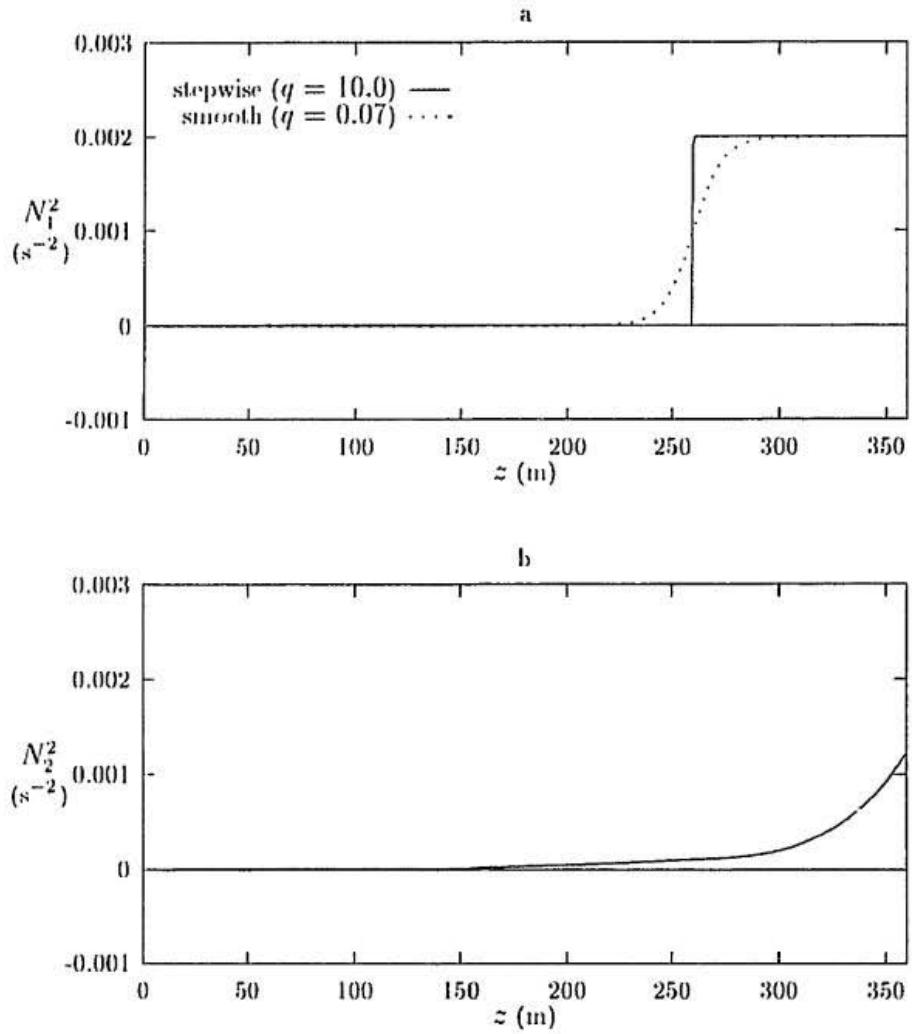

Figure 2.4: The density stratifications used. (a). Stepwise and smooth $N_1^2(z)$, the values of q are indicated by keys. (b). $N_2^2(z)$.

Besides the density stratifications, the fluid needs to be driven from rest so that IGWs can be generated through the interaction between the flow and topography. This is achieved by initializing the model with a uniform rightward flow u in the shallow flat region. The amplitude of the generated IGWs depends on u and the bank slope given by a_2. Other geometric parameters are never changed.

The theory derived in the next chapter is essentially for IGWs with small to moderate amplitude. We want to know how far the theory can be extended for IGWs with larger amplitude. Therefore, the model is run for three different u which produce small, moderate and large IGWs. Specifically, u is set to 0.417 m/s, 0.833 m/s and 5.556 m/s, and the corresponding runs will be referred to as the weak, moderate and strong forcing cases, respectively.

2.2.3 Running strategy

In order to obtain the desired flow patterns in the fixed domain within a specified evolution time, some parameters such as the background velocity u, the bank slope a_2, deceleration time, etc. have to be adjusted.

When $\bar{u}$ is large, the flow on the top of the bank might become supercritical. The IGWs can not propagate upstream and wave energy accumulates over the bank

edge. Such a situation will cause strong overturning which results in large drops in the time step and ultimately in large numerical errors. To avoid this, we decelerate the fluid after the IGWs are generated and the wave front has become detached from the topography. This has no effect on the subsequent evolution of the wave front. The terminal values of $\bar{u}$ for the three forcing cases are listed in Table 4.1.

For the strong forcing case, since the generated initial depression has a large amplitude, the nonlinear effect will quickly steepen the wave front, thus resulting in the development of an undular bore before the front can propagate away from the bank. What we need is a smooth initial depression with only a mode-one wave which is detached from the bank so that the theory can be applied to it and its theoretical evolution can be seen clearly. This can be done by using a smaller bank slope a_2. Then the generated depression will have a smoother front and propagate away from the bank before developing ripples.

2.3 Running the Model

Usually, the model is run for a time length of about $T = 16000$s (approximately four and half days), the output (the velocity field, the density field and the pressure field) is stored at an interval of 1600s and is labeled by output number 1 to 10. Figure 2.5-

2.8 are some of the run results with background states indicated in the captions. A depression in isopycnals in the deep flat region evolve into an undular bore about 10000s later. Note that only the density field of the output is presented, since the theory derived later will be compared with the density perturbations only.

The code IGWsim was originally written to investigate the waves generated by tidal flow across a bank edge. Because of this it was straightforward to generate a depression via this mechanism. Later on, for runs with the stratification $N_2^2(z)$, it was found that it was hard to generate an initial depression that was steep enough to form an undular bore before it left the computational domain. This difficulty was partially due to strong overturning at the bank edge. Therefore, for the runs with $N_2^2(z)$, the initial depression is not generated by flow over a bank edge. Instead, we simply initialize the model with a mode-one linear wave in a flat bottom domain by the use of the first order perturbation derived later.

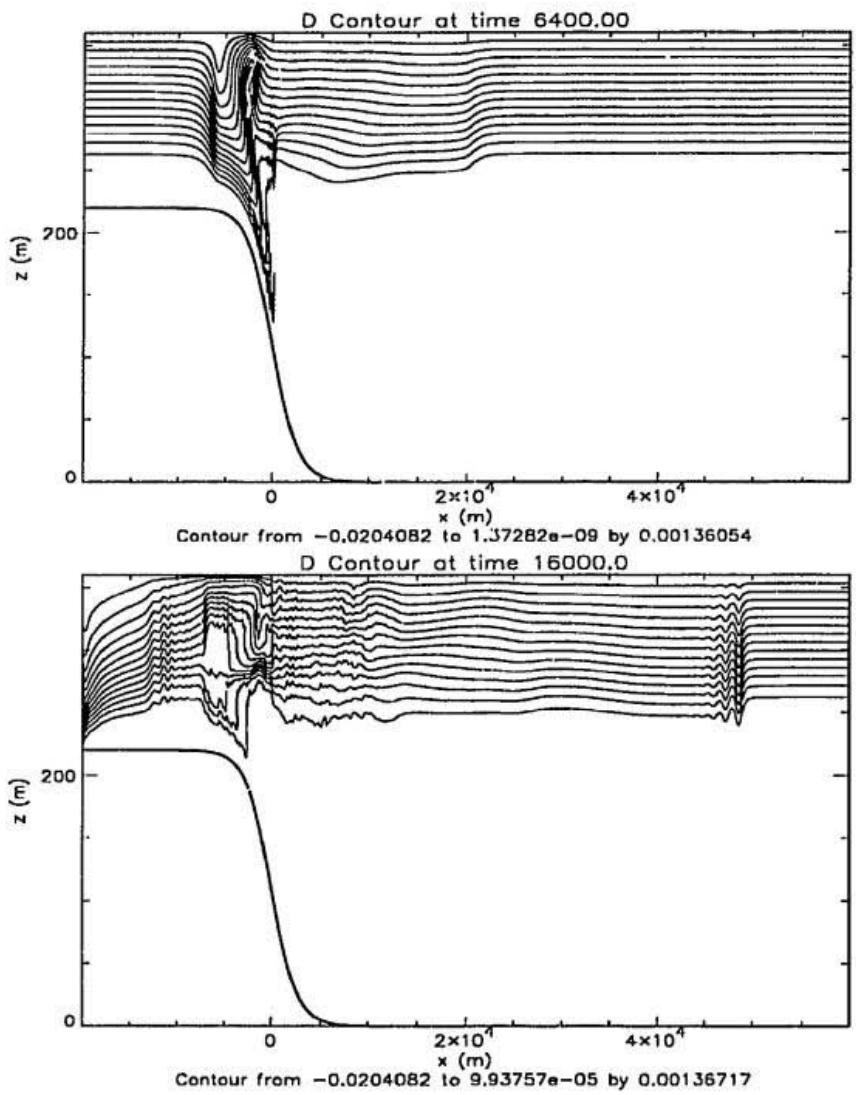

Figure 2.5: Density contours for smooth $N_1^2(z)$ and moderate forcing. The upper one is at output 4 and the lower is at output 10.

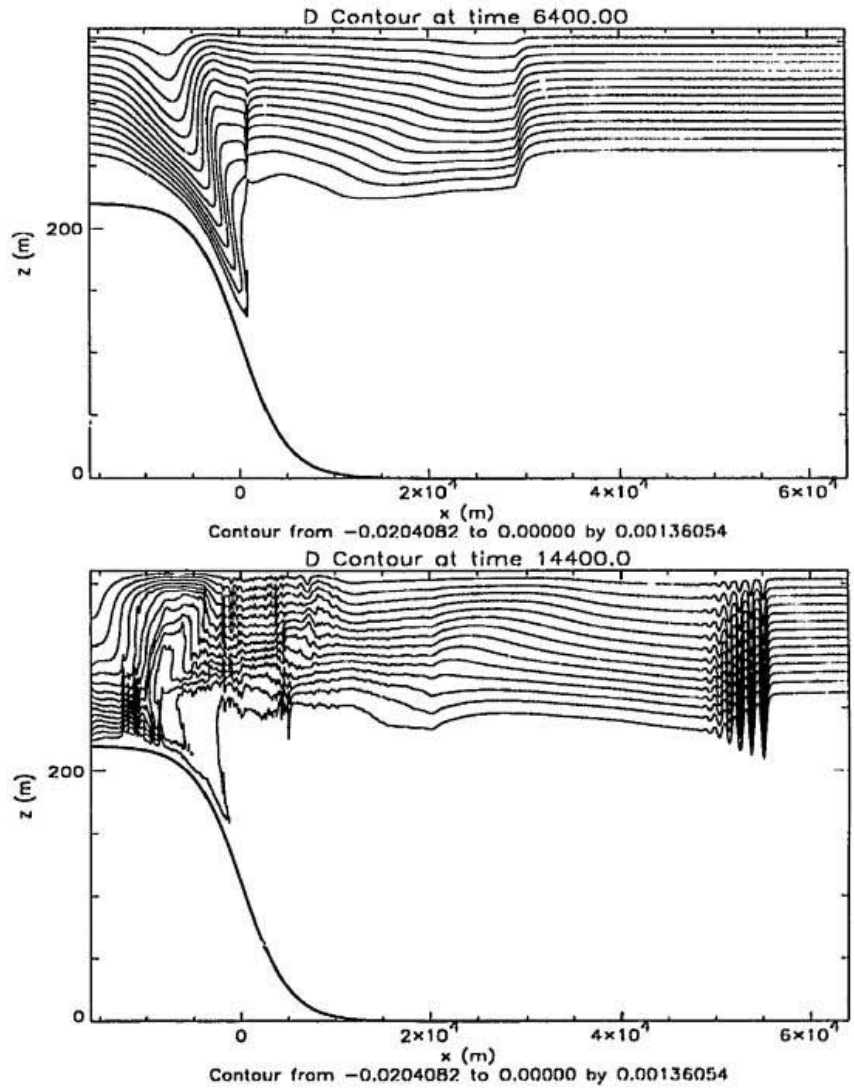

Figure 2.6: Density contours for smooth $N_1^2(z)$ and strong forcing. The upper one is at output 4 and the lower is at output 9.

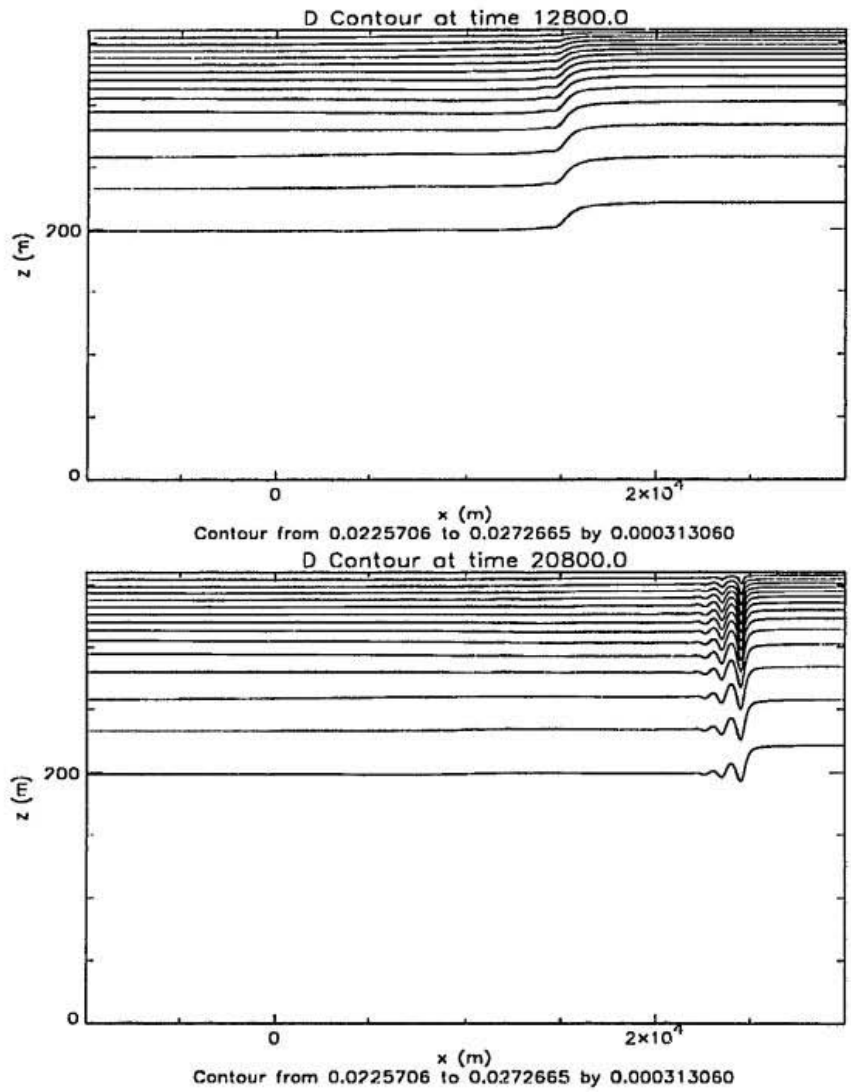

Figure 2.7: Density contours for $N_2^2(z)$ and strong forcing. The upper one is at output 8 and the lower is at output 13.

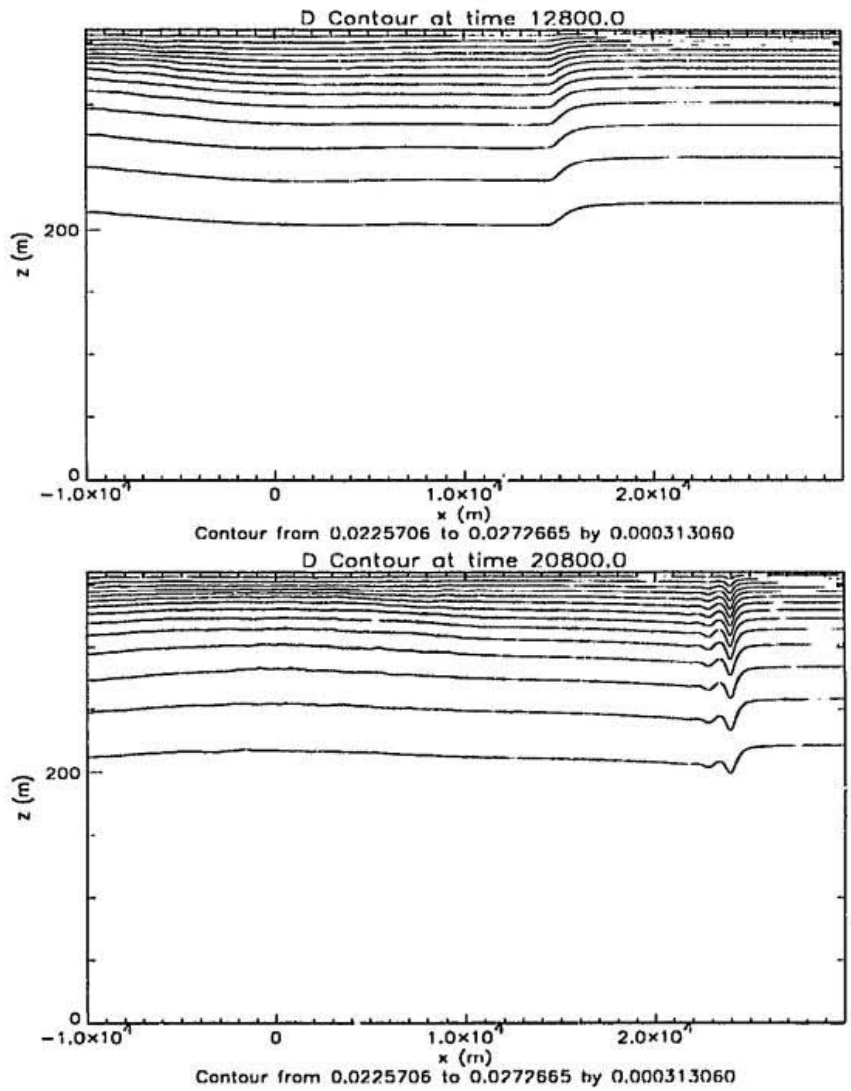

Figure 2.8: Density contours for $N_2^2(z)$ and strong forcing, with rotation included. The upper one is at output 8 and the lower is at output 13.

Chapter 3

Nonlinear Theory of Long Internal Gravity Waves

3.1 Introduction

The nonlinear theory of IGWs is an extension of the surface gravity wave (denoted as SGWs hereafter) theory. In the classical problems concerning SGWs, the fluid is homogeneous and incompressible and the motion is taken to be irrotatonal. On these basic assumptions, two distinct theories have been developed:

(A). An infinitesimal amplitude theory which leads to the linearization of Euler's equations and results in linear dispersive SGWs. This theory is the zeroth term (or

the zeroth order solution) in an asymptotic expansion in powers of the perturbation parameter $\epsilon = a/H$ with a and H denoting the wave amplitude and the undisturbed depth of the fluid. The theory was also extended to finite amplitude waves by the perturbation method. The basic idea is that the higher order terms in the expansion can be regarded as correction terms to the zeroth order linear solution for a situation where finite amplitude waves occur and the nonlinearity can not be neglected.

(B). A long-wave (or shallow water) theory for waves which are long compared to the undisturbed depth of the fluid. This theory is based upon the smallness of the controlling scale parameter $\mu = H^2/L^2$ where L is the typical wavelength. In the limit $\mu \to 0$ the flow becomes hydrostatic and the perturbation quantities are independent of depth. The result is a nonlinear shallow water equation system. In this theory, it is found that an initial disturbance tends to be distorted and break, a phenomenon absent in the linear wave theory.

The two theories can be combined. This leads to nonlinear, dispersive waves for a homogeneous fluid.

It is well known, through the pioneering work of Scott Russell [1837, 1844], Rayleigh [1876], Stokes [1847, 1880], and Korteweg and deVries [1895], that long nonlinear SGWs in a homogeneous shallow fluid depend crucially on two parameters, i.e., the nonlinearity ϵ and the dispersivity μ. When $\epsilon/\mu \gg 1$, the nonlinear effect

dominates and the waves tend to steepen and break, while if $\epsilon/\mu \ll 1$, the dispersive effect dominates and the waves tend to be linear dispersive ones. When $\epsilon/\mu \sim 1$ the two opposite effects tend to cancel each other. In this case a class of finite amplitude wave profiles of permanent form can be obtained, e.g., solitary or cnoidal waves.

The above theories can be extended to vertically trapped waves in stratified shear flows. Long [1956, 1965, 1972] has shown that long nonlinear IGWs are possible in a bounded stratified fluid. Benjamin [1966] found that permanent IGWs are also possible in shear flows with stratification. Benney [1966] extended Benjamin's work to include the time dependent properties by introducing a two-parameter (ϵ and μ) expansion method. By this method, he derived the KdV equation which governs the long nonlinear IGWs on isopycnals. Lee & Beardsley [1974] further developed this method by including in the perturbation expansion a third parameter measuring the non-Boussinesq effect, and thus obtained a KdV type equation which involves three small parameters. A modified KdV with a second order term in ϵ (a cubic term) was also derived in their paper, in the case of IGWs with large amplitudes.

In this section, long nonlinear IGWs on isopycnals in an inviscid, stratified, Boussinesq fluid with shear flow confined by rigid boundaries are investigated. By the method of two-parameter perturbation expansion developed by Benney, Lee and Beardsley, a modified KdV (mKdV) equation with the cubic term is rederived. This

equation is supposed to describe the evolution of the long nonlinear isopycnal wave profiles with large amplitudes.

3.2 Derivation of Modified KdV Equation

Consider an incompressible, inviscid, nondiffusive, stratified fluid with a shear flow in a two-dimensional domain confined by flat rigid boundaries.

The governing equations for the system are Euler's equations,

$$\rho(u_t + uu_x + wu_z) = -p_x, \tag{3.1}$$

$$\rho(w_t + uw_x + ww_z) = -p_z - \rho g, \tag{3.2}$$

$$\rho_t + u\rho_x + w\rho_z = 0, \tag{3.3}$$

$$u_x + w_z = 0, \tag{3.4}$$

with no-normal-flow boundary condition,

$$w(0) = w(H) = 0, \tag{3.5}$$

where ρ is the density, p is the pressure, u and w are the horizontal and vertical velocities, respectively, g is the acceleration due to gravity, and the subscripts denote partial differentiation. The vertical coordinate z is directed upward with zero at the bottom, and the horizontal coordinate x is directed to the right.

An exact solution of (3.1)-(3.5) is the basic state:

$$\rho = \bar{\rho}(z), \tag{3.6}$$

$$p = \bar{p}(z), \tag{3.7}$$

$$\vec{u} = \vec{\bar{u}} = (\bar{u}(z), 0, 0), \tag{3.8}$$

with

$$\frac{d\bar{p}}{dz} = -\bar{\rho}g, \tag{3.9}$$

where $\vec{\bar{u}}(z)$ is the shear flow, $\bar{\rho}(z)$ and $\bar{p}(z)$ are the undisturbed density and pressure distributions.

We now consider small perturbations about this basic state. Introducing perturbations in $\epsilon = a/H$ which is assumed small,

$$\vec{u} = \vec{\bar{u}} + \epsilon\vec{u}', \ \rho = \bar{\rho} + \epsilon\rho', \ p = \bar{p} + \epsilon p', \ w = \epsilon w', \tag{3.10}$$

and substituting this into (3.1) through (3.4) we have

$$(\bar{\rho} + \epsilon\rho')(u'_t + \bar{u}u'_x + \bar{u}_z w') + (\epsilon\bar{\rho} + \epsilon^2\rho')(u'u'_x + w'u'_z) = -p'_x, \tag{3.11}$$

$$(\bar{\rho} + \epsilon\rho')(w'_t + \bar{u}w'_x) + (\epsilon\bar{\rho} + \epsilon^2\rho')(u'w'_x + w'w'_z) = -p'_z - \rho' g, \tag{3.12}$$

$$\rho'_t + \bar{u}\rho'_x + w'\bar{\rho}_z + \epsilon(u'\rho'_x + w'\rho'_z) = 0, \tag{3.13}$$

$$u'_x + w'_z = 0. \tag{3.14}$$

We nondimensionalize this system by

$$x = L\hat{x},\ z = H\hat{z},\ t = \frac{L}{U}\hat{t},\ p' = \rho_0\hat{p},$$

$$u' = U\hat{u},\ w' = \frac{UH}{L}\hat{w},\ p' = \rho_0 Hg\hat{p},\ u = U\hat{u}, \tag{3.15}$$

where the scaling factor $W = UH/L$ comes from the equation of continuity (3.3), and $T = L/U$ is the convection time scale. Then we have the nondimensional equations (with the hats dropped):

$$(\bar{\rho} + \epsilon\rho)(u_t + \bar{u}u_x + \bar{u}_z w) + (\epsilon\bar{\rho} + \epsilon^2\rho)(uu_x + wu_z) = -Gp_x, \tag{3.16}$$

$$\mu(\bar{\rho} + \epsilon\rho)(w_t + \bar{u}w_x) + \mu(\epsilon\bar{\rho} + \epsilon^2\rho)(uw_x + ww_z) = -G(p_z + \rho), \tag{3.17}$$

$$\rho_t + \bar{u}\rho_x + w\bar{\rho}_z + \epsilon(u\rho_x + w\rho_z) = 0, \tag{3.18}$$

$$u_x + w_z = 0, \tag{3.19}$$

where $G = gH/U^2$ is the square of the inverse Froude number (see section 2.2.2) and $\mu = H^2/L^2$. Note that now all variables without an overbar are perturbation variables.

We now make the Boussinesq approximation which leads to the disappearance of the factor $\bar{\rho} + \epsilon\rho$ in the equation system (3.16) and (3.17). This is based on the fact that the water density in the ocean has only small variations ($< 0.3\,\%$) about a constant non-dimensional value of 1. The incompressibility of the fluid allows us to

introduce a perturbation streamfunction ψ, such that

$$\begin{aligned} u &= \psi_z, \\ w &= -\psi_x, \end{aligned} \tag{3.20}$$

After substituting these two and eliminating p in (3.16) and (3.17), we get equations for ρ and ψ:

$$\begin{aligned} &\left(\frac{\partial}{\partial t} + \bar{u}\frac{\partial}{\partial x}\right)\psi_{zz} - \bar{u}_{zz}\psi_x + \epsilon(\psi_z\psi_{zzx} - \psi_x\psi_{zzz}) \\ &+\mu\left(\frac{\partial}{\partial t} + \bar{u}\frac{\partial}{\partial x}\right)\psi_{xx} + \mu\epsilon(\psi_z\psi_{xxx} - \psi_x\psi_{xxz}) - G\rho_x = 0 \end{aligned} \tag{3.21}$$

$$\left(\frac{\partial}{\partial t} + \bar{u}\frac{\partial}{\partial x}\right)\rho - \bar{\rho}_z\psi_x + \epsilon(\psi_z\rho_x - \psi_x\rho_z) = 0 \tag{3.22}$$

$$\psi_x(x,0;t) = \psi_x(x,1;t) = 0 \tag{3.23}$$

Equation (3.23) says that the streamfunction ψ is constant along boundaries. This system of equations involves three parameters G, ϵ and μ.

For the long nonlinear IGWs considered here, we assume that the parameter μ, along with ϵ, is small. G is assumed to be $O(1)$. Thus, we can search for an asymptotic expansion solution of the form

$$\begin{aligned} \psi = &\psi^{0,0}(x,z;t) + \epsilon\psi^{1,0}(x,z;t) + \mu\psi^{0,1}(x,z;t) \\ &+\epsilon^2\psi^{2,0}(x,z;t) + \epsilon\mu\psi^{1,1}(x,z;t)\ldots, \end{aligned} \tag{3.24}$$

$$\rho = \rho^{0,0}(x,z;t) + \epsilon\rho^{1,0}(x,z;t) + \mu\rho^{0,1}(x,z;t)$$
$$+\epsilon^2\rho^{2,0}(x,z;t) + \epsilon\mu\rho^{1,1}(x,z;t)\ldots. \tag{3.25}$$

Substituting these into (3.21), (3.22) and (3.23) gives:

The $O(1)$ problem:

$$(\frac{\partial}{\partial t} + \bar{u}\frac{\partial}{\partial x})\psi^{0,0}_{zz} - \bar{u}_{zz}\psi^{0,0}_x - G\rho^{0,0}_x = 0, \tag{3.26}$$
$$(\frac{\partial}{\partial t} + \bar{u}\frac{\partial}{\partial x})\rho^{0,0} - \bar{\rho}_z\psi^{0,0}_x = 0, \tag{3.27}$$
$$\psi^{0,0}_x(x,0;t) = \psi^{0,0}_x(x,1;t) = 0. \tag{3.28}$$

The $O(\epsilon)$ problem:

$$(\frac{\partial}{\partial t} + \bar{u}\frac{\partial}{\partial x})\psi^{1,0}_{zz} - \bar{u}_{zz}\psi^{1,0}_x - G\rho^{1,0}_x = \psi^{0,0}_x\psi^{0,0}_{zzz} - \psi^{0,0}_z\psi^{0,0}_{zzx}, \tag{3.29}$$
$$(\frac{\partial}{\partial t} + \bar{u}\frac{\partial}{\partial x})\rho^{1,0} - \bar{\rho}_z\psi^{1,0}_x = \psi^{0,0}_x\rho^{0,0}_z - \psi^{0,0}_z\rho^{0,0}_x, \tag{3.30}$$
$$\psi^{1,0}_x(x,0;t) = \psi^{1,0}_x(x,1;t) = 0. \tag{3.31}$$

The $O(\mu)$ problem:

$$(\frac{\partial}{\partial t} + \bar{u}\frac{\partial}{\partial x})\psi^{0,1}_{zz} - \bar{u}_{zz}\psi^{0,1}_x - G\rho^{0,1}_x = -(\frac{\partial}{\partial t} + u\frac{\partial}{\partial x})\psi^{0,0}_{xx}, \tag{3.32}$$
$$(\frac{\partial}{\partial t} + \bar{u}\frac{\partial}{\partial x})\rho^{0,1} - \bar{\rho}_z\psi^{0,1}_x = 0, \tag{3.33}$$
$$\psi^{0,1}_x(x,0;t) = \psi^{0,1}_x(x,1;t) = 0. \tag{3.34}$$

The $O(\epsilon^2)$ problem:

$$
\begin{aligned}
(\frac{\partial}{\partial t}+\bar{u}\frac{\partial}{\partial x})\psi^{\cdot\cdot 0}_{zz}-\bar{u}_{zz}\psi^{2,0}_{x}-G\rho^{2,0}_{x} &= (\psi^{0,0}_{x}\psi^{1,0}_{zzz}+\psi^{0,0}_{zzz}\psi^{1,0}_{x}) \\
&\quad -(\psi^{0,0}_{z}\psi^{1,0}_{zzx}+\psi^{0,0}_{zzx}\psi^{1,0}_{z}) \qquad (3.35)\\
(\frac{\partial}{\partial t}+\bar{u}\frac{\partial}{\partial x})\rho^{2,0}-\bar{\rho}_{z}\psi^{2,0}_{x} &= (\psi^{0,0}_{x}\rho^{1,0}_{z}+\rho^{0,0}_{z}\psi^{1,0}_{x}) \\
&\quad -(\psi^{0,0}_{z}\rho^{1,0}_{x}+\rho^{0,0}_{x}\psi^{1,0}_{z}) \qquad (3.36)\\
\psi^{2,0}_{x}(x,0;t)=\psi^{2,0}_{x}(x,1;t) &= 0 \qquad (3.37)
\end{aligned}
$$

In the following, we will discuss and solve the above problems one by one up to the second order in ϵ.

3.2.1 The $O(1)$ problem.

A simple manipulation of (3.26) and (3.27) gives

$$
(\frac{\partial}{\partial t}+\bar{u}\frac{\partial}{\partial x})^2\psi^{0,0}_{zz}-\bar{u}_{zz}(\frac{\partial}{\partial t}+\bar{u}\frac{\partial}{\partial x})\psi^{0,0}_{x}-G\bar{\rho}_{z}\psi^{0,0}_{xx}=0, \qquad (3.38)
$$

with the boundary condition as before.

The equation (3.38) has an infinite number of solutions, most of which are difficult to find and to deal with. It would be nice if it had a separable solution, because this kind of solution is easy to handle. To see whether there exist such

solutions, we assume

$$\psi^{0,0} = A(x,t)\phi(z), \tag{3.39}$$

and substitute this into (3.38). This gives

$$G\bar{\rho}_z\phi = \left[\frac{(\frac{\partial}{\partial t} + \bar{u}\frac{\partial}{\partial x})^2 A}{A_{xx}}\right]\phi_{zz} - \left[\frac{A_{xt} + \bar{u}A_{xx}}{A_{xx}}\right]\bar{u}_{zz}\phi. \tag{3.40}$$

The left side of this equation is a function of z only, so the right side must be as well. This requires that

$$\frac{A_{xt}}{A_{xx}} + \bar{u}(z) = f_1(z), \tag{3.41}$$

$$\frac{(\frac{\partial}{\partial t} + \bar{u}\frac{\partial}{\partial x})^2 A}{A_{xx}} = f_2(z), \tag{3.42}$$

where f_1 and f_2 are functions of z only. From (3.41), it is obvious that we must have $A_{xt} = -cA_{xx}$ for some constant c. This leads to

$$A_t = -cA_x + T(t). \tag{3.43}$$

Substitution into (3.42) shows that $dT(t)/dt$ must be a constant. We are not interested in solutions which become unbounded as t increases, so we must set $T = 0$. Thus, for a separable solution, A must satisfy the linear nondispersive wave equation

$$A_t = -cA_x. \tag{3.44}$$

As for the value of c and the vertical mode $\phi(z)$, we need to solve the corresponding eigenvalue problem which is obtained by substituting (3.44) into (3.38)

$$\phi_{zz} - \left[\frac{\bar{u}_{zz}}{(\bar{u}-c)} + \frac{G\bar{\rho}_z}{(\bar{u}-c)^2}\right]\phi = 0, \tag{3.45}$$

$$\phi(0) = \phi(1) = 0. \tag{3.46}$$

This eigenvalue problem is solvable, at least numerically. Imposing the condition $u(z) \neq c$ for any z (i.e., no critical layers), there is a discrete, infinite spectrum of eigenvalues $c_1 > c_2 > c_3 > \cdots$ with corresponding eigenfunctions $\phi_1, \phi_2, \cdots$. The solution c_n, $\phi_n(z)$ is the mode-n linear wave. The nondispersive aspect of the zero order solution is a result of $\mu \ll 1$ (i.e., the long wave approximation).

From (3.27) we immediately see that $\rho^{0,0}$ also has the separable solution

$$\rho^{0,0} = A(x,t)D_n(z), \tag{3.47}$$

where

$$D_n = \frac{\bar{\rho}_z}{\bar{u}-c_n}\phi_n. \tag{3.48}$$

3.2.2 The $O(\epsilon)$ problem.

We again choose to seek separable solutions for $O(\epsilon)$ problem (3.29) to (3.31). Therefore, we assume

$$\psi^{1,0} = A^{1,0}(x,t)\phi^{1,0}(z), \tag{3.49}$$

$$\rho^{1,0} = B^{1,0}(x,t)D^{1,0}(z). \tag{3.50}$$

Substituting the $O(1)$ solution into the right hand side of (3.29) and (3.30), we see that

$$\psi_x^{0,0}\psi_{zzz}^{0,0} - \psi_z^{0,0}\psi_{zzx}^{0,0} = AA_x(\phi\phi_{zzz} - \phi_z\phi_{zz}), \tag{3.51}$$

$$\psi_x^{0,0}\rho_z^{0,0} - \psi_z^{0,0}\rho_x^{0,0} = AA_x(\phi^2(\frac{\rho_z}{\bar{u}-c})_z). \tag{3.52}$$

Since the inhomogeneous terms have the separable AA_x factor, we want $\psi_x^{1,0}, \rho_x^{1,0}, \psi_t^{1,0}$ and $\rho_t^{1,0}$ to have the factor as well. By taking

$$A^{1,0} = B^{1,0} = A^2(x,t), \tag{3.53}$$

we get the required separable form.

Substituting $\psi^{1,0}, \rho^{1,0}$ into (3.29) and (3.30), and eliminating $D^{1,0}(z)$, we end up with an equation system for $\phi^{1,0}$:

$$(\bar{u}-c)^2\phi_{zz}^{1,0} - [(\bar{u}-c)\bar{u}_{zz} + G\rho_z]\phi^{1,0} =$$

$$\frac{1}{2}\left[(\bar{u}-c)(\phi\phi_{zzz}-\phi_z\phi_{zz})+G\phi^2\left(\frac{\bar{\rho}_z}{\bar{u}-c}\right)_z\right], \tag{3.54}$$

$$\phi^{1,0}(0)=\phi^{1,0}(1)=0. \tag{3.55}$$

Note that the operator on the left side of (3.54), which acts on $\phi^{1,0}$, is the same as that for the $O(1)$ problem (3.45). Thus (3.54) is an inhomogeneous form of the eigenvalue problem (3.45). Now the question is whether equation (3.54) has a solution which satisfies the given boundary condition.

Multiplying (3.54) by $\phi/(\bar{u}-c)^2$ and then using (3.45) we get

$$\frac{d}{dz}(\phi_z^{1,0}\phi-\phi_z\phi^{1,0})=J(z), \tag{3.56}$$

where

$$J(z)=\frac{(\bar{u}-c)^{-2}}{2}[(\bar{u}-c)(\phi\phi_{zzz}-\phi_z\phi_{zz})+G\phi^2(\frac{\bar{\rho}_z}{\bar{u}-c})_z]\phi. \tag{3.57}$$

Here we have assumed nonzero $(\bar{u}-c)$.

Due to the associated boundary conditions of ϕ and $\phi^{1,0}$, integrating (3.56) from 0 to 1 gives

$$\int_0^1 J(z)dz=0. \tag{3.58}$$

Thus, in order for there to be a separable solution condition (3.58) must be satisfied. One special case for which this is true is the one with $\bar{u}=$ constant and $\bar{\rho}_z=$ constant. But in general, (3.58) is not satisfied.

If (3.58) is not satisfied the problem may be fixed by assuming that A does not strictly propagate at constant speed without changing its shape as represented by $A_t = -cA_x$. Benney [1966] suggested that the evolution equation (3.44) be modified by adding an $O(\epsilon)$ correction of the form

$$A_t = -cA_x + \epsilon Q(x,t). \tag{3.59}$$

We now must return to the $O(1)$ problem. This time we substitute (3.59), instead of (3.44), into (3.40). This gives

$$[(\bar{u}-c)\phi_{zz} - \bar{u}_{zz}\phi - gD]A_x = -\epsilon Q(x,t)\phi_{zz}, \tag{3.60}$$

$$[(\bar{u}-c)D - \bar{\rho}_z\phi]A_x = -\epsilon Q(x,t)D. \tag{3.61}$$

This is the same problem as we had in (3.45) except with additional $O(\epsilon)$ terms appearing on the right side which are not at the same order as those on the left side. These $O(\epsilon)$ terms belong in the $O(\epsilon)$ problem. Thus the $O(1)$ problem is still given by (3.45) and (3.46). However in the $O(\epsilon)$ problem, the right sides of (3.51) and (3.52) become

$$AA_x(\phi\phi_{zzz} - \phi_z\phi_{zz}) - Q(x,t)\phi_{zz}, \tag{3.62}$$

$$AA_x\phi^2\left(\frac{\bar{\rho}_z}{\bar{u}-c}\right)_z - Q(x,t)D, \tag{3.63}$$

respectively. A separable solution now requires that $Q \propto AA_x$. This clearly indicates that the assumed shape change, or the phase speed deviation, is due to the nonlinear effect arising from the AA_x term. Following Benney[1966] we let the proportionality constant be $2r$ so that (3.59) becomes

$$A_t = -cA_x + \epsilon 2rAA_x. \tag{3.64}$$

Physically, the effect of the new term is to introduce an $O(\epsilon)$ correction to the propagation speed, which is now $(c - \epsilon 2rA)$.

Now the $O(\epsilon)$ problem becomes

$$(\bar{u} - c)\phi^{1,0}_{zz} - \bar{u}_{zz}\phi^{1,0} - GD^{1,0} = \frac{1}{2}(\phi\phi_{zzz} - \phi_z\phi_{zz}) - r\phi_{zz}, \tag{3.65}$$

$$(\bar{u} - c)D^{1,0} - \bar{\rho}_z\phi^{1,0} = \frac{\phi^2}{2}\left(\frac{\bar{\rho}_z}{\bar{u} - c}\right)_z - rD, \tag{3.66}$$

$$\phi^{1,0}(0) = \phi^{1,0}(1) = 0, \tag{3.67}$$

or alternatively,

$$\phi^{1,0}_{zz} - \left[\frac{\bar{u}_{zz}}{\bar{u} - c} + \frac{G\bar{\rho}_z}{(\bar{u} - c)^2}\right]\phi^{1,0} = \frac{\phi\phi_{zzz} - \phi_z\phi_{zz}}{2(\bar{u} - c)} + \frac{G\phi^2}{2(\bar{u} - c)^2}\left(\frac{\bar{\rho}_z}{\bar{u} - c}\right)_z - r\left(\frac{\phi_{zz}}{\bar{u} - c} + \frac{G\bar{\rho}_z}{(\bar{u} - c)^3}\phi\right), \tag{3.68}$$

$$\phi^{1,0}(0) = \phi^{1,0}(1) = 0, \tag{3.69}$$

and

$$D^{1,0} = \frac{1}{u-c}\left[\rho_z \phi^{1,0} + \frac{\phi^2}{2}\left(\frac{\rho_z}{u-c}\right)_z - r\frac{\rho_z \phi}{u-c}\right], \tag{3.70}$$

with the corresponding

$$\begin{aligned} J(z) &= \frac{1}{2}\left[\frac{\phi\phi_{zzz} - \phi_z\phi_{zz}}{u-c} + \frac{Gi\phi^2}{(u-c)^2}\left(\frac{\rho_z}{u-c}\right)_z\right]\phi \\ &\quad - r\left[\frac{\phi_{zz}}{u-c} + \frac{Gi\rho_z\phi}{(u-c)^3}\right]\phi. \end{aligned} \tag{3.71}$$

The satisfaction of the condition (3.58) now gives

$$r = \frac{I_r}{I} \tag{3.72}$$

where

$$I_r = \frac{1}{2}\int_0^1 \left[\frac{\phi\phi_{zzz} - \phi_z\phi_{zz}}{u-c} + \frac{Gi\phi^2}{(u-c)^2}\left(\frac{\rho_z}{u-c}\right)_z\right]\phi dz, \tag{3.73}$$

$$I = \int_0^1 \left[\frac{\phi_{zz}\phi}{u-c} + \frac{Gi\phi^2\rho_z}{(u-c)^3}\right]dz. \tag{3.74}$$

Thus, with r calculated by using the solution ϕ of the eigenvalue problem (3.45), the $O(\epsilon)$ problem for $\phi^{1,0}$ and $D^{1,0}$ is solvable.

3.2.3 The $O(\mu)$ problem.

The procedure adopted in this problem is the same as in the previous problem. So only an outline is presented here.

We again want to seek a separable solution for the system (3.32) to (3.34), so we set

$$\psi^{0,1} = A^{0,1}(x,t)\phi^{0,1}(z), \tag{3.75}$$

$$\rho^{0,1} = B^{0,1}(x,t)D^{0,1}(z). \tag{3.76}$$

Substituting $\psi^{0,0}$ into the equations (3.32) and (3.33) suggests that

$$A^{0,1} = B^{0,1} = A_{xx}. \tag{3.77}$$

The substitution of this separable form and the elimination of $D^{0,1}$ gives

$$(\bar{u}-c)^2\phi^{0,1}_{zz} - [(\bar{u}-c)\bar{u}_{zz} + G'\bar{\rho}_z]\phi^{0,1} = -(\bar{u}-c)^2\phi \tag{3.78}$$

$$\phi^{0,1}(0) = \phi^{0,1}(1) = 0 \tag{3.79}$$

where only the leading order term of A_t (namely $-cA_x$) has been used. Note again that (3.78) is the inhomogeneous form of (3.45). By the same procedure used for the $O(\epsilon)$ problem, the existance of a solution of (3.78) requires

$$\int_0^1 J(z)dz = 0,$$

where

$$J(z) = -\phi^2(z), \tag{3.80}$$

which certainly can not be satisfied unless $\phi = 0$.

To solve this dilemma we set

$$A_t = -cA_x + 2\alpha rAA_x + \mu R(x,t), \tag{3.81}$$

with μR as another factor causing the deviation from linear nondispersive waves.

With (3.77) and (3.81) substituted in (3.32) and (3.33), the forcing terms of the $O(\mu)$ problem become

$$-(\bar{u}-c)\phi A_{xxx} - R\phi_{zz}, \tag{3.82}$$

$$-R\frac{\bar{\rho}_z}{\bar{u}-c}\phi, \tag{3.83}$$

which indicate that for a separable solution we should have $R = sA_{xxx}$ with s being a constant. This in fact implies that the new term in the evolution equation for A results in dispersion.

Then the $O(\mu)$ problem becomes

$$(\bar{u}-c)\phi^{0,1}_{zz} - \bar{u}_{zz}\phi^{0,1} - GD^{0,1} = -(u-c)\phi - s\phi_{zz}, \tag{3.84}$$

$$(\bar{u}-c)D^{0,1} - \bar{\rho}_z\phi^{0,1} = -sD, \tag{3.85}$$

$$\phi^{0,1}(0) = \phi^{0,1}(1) = 0, \tag{3.86}$$

or alternatively,

$$\phi^{0,1}_{zz} - \left[\frac{\bar{u}_{zz}}{(\bar{u}-c)} + \frac{G\bar{\rho}_z}{(\bar{u}-c)^2}\right]\phi^{0,1} = -\phi - s\left[\frac{\phi_{zz}}{(\bar{u}-c)} + \frac{G\rho_z}{(u-c)^3}\phi\right], \tag{3.87}$$

$$\phi^{0,1}(0) = \phi^{0,1}(1) = 0, \tag{3.88}$$

and

$$D^{0,1} = \frac{\bar{\rho}_z}{(\bar{u}-c)}\phi^{0,1} - s\frac{\bar{\rho}_z}{(\bar{u}-c)^2}\phi, \tag{3.89}$$

and consequently, $J(z)$ is now

$$J(z) = -\phi^2 - s\left[\frac{\phi_{zz}\phi}{\bar{u}-c} + \frac{G\bar{\rho}_z\phi^2}{(\bar{u}-c)^3}\right]. \tag{3.90}$$

Thus the condition $\int_0^1 J dz = 0$ gives

$$s = \frac{I_s}{I} \tag{3.91}$$

where

$$I_s = -\int_0^1 \phi^2 dz, \tag{3.92}$$

and I is the same as in (3.74). With this value of s and a wave profile evolving according to

$$A_t = -cA_x + 2\alpha r A A_x + \mu s A_{xxx}, \tag{3.93}$$

the $O(\mu)$ problem for $\phi^{0,1}$ and $D^{0,1}$ is solvable. Equation (3.93) is the KdV equation which describes the time development of long waves under the combined effect of the first order nonlinearity and dispersivity.

3.2.4 The $O(\epsilon^2)$ problem.

In the last section, we derived the KdV equation which is of first order in ϵ and μ and therefore is good for IGWs with small or moderate amplitude. But in the ocean, as reported by many authors, IGWs frequently have amplitudes which are quite large. For these IGWs a second-order amplitude effect must be included. This leads to the derivation of modified KdV equations as was done by Lee & Beardsley[1974]. In this section, following Lee and Beardsley, we solve the $O(\epsilon^2)$ problem and obtain a modified KdV equation (will be denoted as mKdV hereafter).

Substituting the previous results $\psi^{0,0}$, $\psi^{1,0}$ and $\psi^{0,1}$ into the right side of the $O(\epsilon^2)$ problem (3.35) and (3.36), we see that

$$\psi^{0,0}_x\psi^{1,0}_{zzz} + \psi^{0,0}_{zzz}\psi^{1,0}_x = A^2A_x(\phi\phi^{1,0}_{zzz} + 2\phi_{zzz}\phi^{1,0}), \tag{3.94}$$

$$\psi^{0,0}_z\psi^{1,0}_{zzx} + \psi^{0,0}_{zzx}\psi^{1,0}_z = A^2A_x(2\phi_z\phi^{1,0}_{zz} + \phi_{zz}\phi^{1,0}_z), \tag{3.95}$$

and so on. Thus we are inspired to set the following form for a separable solution

$$\psi^{2,0} = A^3\phi^{2,0}, \tag{3.96}$$

$$\rho^{2,0} = A^3D^{2,0}. \tag{3.97}$$

By the substitution of (3.93) and (3.96) and (3.97) into the $O(\epsilon^2)$ problem (3.35) to (3.37), we obtain the equation system for $\phi^{2,0}$ and the corresponding condition for

the existence of separable solutions as we did before. But again that condition is not always satisfied. By the same argument as before, another term representing an even slower change in the wave shape is introduced into the equation governing A

$$A_t = -cA_x + c2rAA_x + \mu sA_{xxx} + \epsilon^2 M(x,t). \tag{3.98}$$

Now we substitute (3.98) and all the obtained results of the lower order problems into the full perturbation equation of the form

$$O(1) + \epsilon O(\epsilon) + \mu O(\mu) + \epsilon^2 O(\epsilon^2)\cdots \tag{3.99}$$

where $O(1)$ to $O(\epsilon^2)$ denote the corresponding hierarchy perturbation equation systems. Properly arranging the terms with the same order, we find the equations for the $O(\epsilon^2)$ problem

$$\begin{aligned} &3A^2A_x[(u-c)\phi^{2,0}_{zz} - u_{zz}\phi^{2,0} - GD^{2,0}] = \\ &\quad[(\phi\phi^{1,0}_{zzz} + 2\phi_{zzz}\phi^{1,0}) - (2\phi_z\phi^{1,0}_{zz} + \phi_{zz}\phi^{1,0}_z) - 4r\phi^{1,0}_{zz}]A^2A_x \\ &\quad - M\phi_{zz}, \end{aligned} \tag{3.100}$$

$$\begin{aligned} &3A^2A_x[(u-c)D^{2,0} - \bar{\rho}_z\phi^{2,0}] = \\ &\quad[(\phi D^{1,0}_z + 2D_z\phi^{1,0}) - (2\phi_z D^{1,0} + D\phi^{1,0}_z - 4rD^{1,0})]A^2A_x \\ &\quad - MD, \end{aligned} \tag{3.101}$$

where the terms involving r are from $O(\epsilon)$ problem because of their higher order, as the terms involving M do from the zero order problem. This requires that $M \propto A^2 A_x$ for a separable solution. Let

$$M(x,t) = \lambda A^2 A_x, \tag{3.102}$$

we then get the equation system for $\phi^{2,0}$ and $D^{2,0}$

$$(\bar{u}-c)\phi^{2,0}_{zz} - \bar{u}_{zz}\phi^{2,0} - GD^{2,0} = \frac{1}{3}(\phi\phi^{1,0}_{zzz} + 2\phi_{zzz}\phi^{1,0} - 2\phi_z\phi^{1,0}_{zz} - \phi_{zz}\phi^{1,0}_z - 4r\phi^{1,0}_{zz} - \lambda\phi_{zz}), \tag{3.103}$$

$$(\bar{u}-c)D^{2,0} - \bar{\rho}_z\phi^{2,0} = \frac{1}{3}(\phi D^{1,0}_z + 2D_z\phi^{1,0} - 2\phi_z D^{1,0} - D\phi^{1,0}_z - 4rD^{1,0} - \lambda D), \tag{3.104}$$

$$\phi^{2,0}(0) = \phi^{2,0}(1) = 0. \tag{3.105}$$

With $D^{2,0}$ eliminated, these are rewritten as

$$\phi^{2,0}_{zz} - \left[\frac{\bar{u}_{zz}}{(\bar{u}-c)} + \frac{G\bar{\rho}_z}{(\bar{u}-c)^2}\right]\phi^{2,0} = \frac{1}{3(\bar{u}-c)}(\phi\phi^{1,0}_{zzz} + 2\phi_{zzz}\phi^{1,0} - 2\phi_z\phi^{1,0}_{zz} - \phi_{zz}\phi^{1,0}_z - 4r\phi^{1,0}_{zz} - \lambda\phi_{zz}) + \frac{G}{3(\bar{u}-c)^2}(\phi D^{1,0}_z + 2D_z\phi^{1,0} - 2\phi_z D^{1,0} - D\phi^{1,0}_z - 4rD^{1,0} - \lambda D), \tag{3.106}$$

$$\phi^{2,0}(0) = \phi^{2,0}(1) = 0, \tag{3.107}$$

and

$$D^{2,0} = \frac{\bar{\rho}_z}{(\bar{u}-c)}\phi^{2,0} + \frac{1}{3(\bar{u}-c)}(\phi D_z^{1,0} + 2D_z\phi^{1,0} - 2\phi_z D^{1,0} - D\phi_z^{1,0} - 4rD^{1,0} - \lambda D). \quad (3.108)$$

Another form of (3.106) is

$$\frac{d}{dz}(\phi_z^{2,0}\phi - \phi_z\phi^{2,0}) = J(z),$$

with $J(z)$ being

$$J(z) = \frac{\phi}{3(\bar{u}-c)}(\phi\phi_{zzz}^{1,0} + 2\phi_{zzz}\phi^{1,0} - 2\phi_z\phi_{zz}^{1,0} - \phi_{zz}\phi_z^{1,0} - 4r\phi_{zz}^{1,0} - \lambda\phi_{zz}) + \frac{G\phi}{3(\bar{u}-c)^2}(\phi D_z^{1,0} + 2D_z\phi^{1,0} - 2\phi_z D^{1,0} - D\phi_z^{1,0} - 4rD^{1,0} - \lambda D). \quad (3.109)$$

Then by the condition $\int_0^1 J dz = 0$, and substituting (3.48) and (3.70) for D and $D^{1,0}$, we immediately get

$$\lambda = \frac{I_\Lambda}{I}, \quad (3.110)$$

where

$$\begin{aligned} I_\Lambda = & \int_0^1 \frac{1}{\bar{u}-c}(\phi^2\phi_{zzz}^{1,0} + 2\phi_{zzz}\phi^{1,0}\phi - 2\phi_z\phi_{zz}^{1,0}\phi - \phi_{zz}\phi_z^{1,0}\phi - 4r\phi_{zz}^{1,0}\phi)dz \\ & + G\int_0^1 \frac{1}{(\bar{u}-c)^2}\left\{3\left(\frac{\bar{\rho}_z}{\bar{u}-c}\right)_z\phi^{1,0}\phi^2 + \left(\frac{\bar{\rho}_z}{\bar{u}-c}\right)_{zz}\frac{\phi^4}{2(\bar{u}-c)}\right. \\ & + \left(\frac{\bar{\rho}_z}{\bar{u}-c}\right)_z\left(\frac{1}{\bar{u}-c}\right)_z\frac{\phi^4}{2} + r\frac{\bar{\rho}_z\phi_z\phi^2}{(\bar{u}-c)^2} - r\left(\frac{\bar{\rho}_z}{(\bar{u}-c)^2}\right)_z\phi^3 \\ & \left. -4r\left(\frac{\bar{\rho}_z}{\bar{u}-c}\right)\phi\phi^{1,0} - 2r\left(\frac{\bar{\rho}_z}{\bar{u}-c}\right)_z\left(\frac{\phi^3}{\bar{u}-c}\right) + \frac{4r^2\bar{\rho}_z\phi^2}{(\bar{u}-c)^2}\right\}dz, \end{aligned} \quad (3.111)$$

and I is again given by (3.74). Thus the problem (3.106) to (3.108) for $\phi^{2,0}$ and $D^{2,0}$ can be solved. Note that coefficients r, s and λ have the same denominator I.

3.2.5 Summary.

Using the method of the perturbation expansion in powers of the two small parameters, we have found the approximate solution for long nonlinear IGWs in a stratified fluid with shear flow confined by flat rigid boundaries in a two dimensional domain. For long nonlinear IGWs with finite amplitudes, the second-order nonlinear term in ϵ may be big enough to play an important role in the overall nonlinear effect and therefore can not be neglected. Thus we choose to have the solution consisting of the perturbation solutions up to the second order in ϵ and neglect all the other higher order terms which are much smaller due to the smallness of μ. To summarize, the perturbation streamfunction is given by

$$\psi = A\phi + \epsilon A^2\phi^{1,0} + \mu A_{xx}\phi^{0,1} + \epsilon^2 A^3\phi^{2,0}, \tag{3.112}$$

while the perturbation density is

$$\rho = AD + \epsilon A^2 D^{1,0} + \mu A_{xx} D^{0,1} + \epsilon^2 A^3 D^{2,0}. \tag{3.113}$$

A is governed by

$$A_t + cA_x - \epsilon 2rAA_x - \mu sA_{xxx} - \epsilon^2 \lambda A^2 A_x = 0. \tag{3.114}$$

c, ϕ are determined by the eigenvalue problem (3.45)-(3.46) which has a countably infinite set of solutions $(c_n,\ \phi_n)$ with $c_1 > c_2 > c_3 \cdots$. The other variables $\phi^{1,0}(z)$, $\phi^{0,1}(z)$, $\phi^{2,0}(z)$, $D(z)$, $D^{1,0}(z)$, $D^{0,1}(z)$, $D^{2,0}(z)$ and the constants r, s and λ are given in terms of c and ϕ. Since we are only interested in the mode-one wave $(n = 1)$ which propagates the fastest, we do not use the subscript n and refer all quantities to those associated with the first mode only.

Waves can travel in either the positive or negative direction. The solution (3.112)-(3.114) should have the appropriate symmetry. It is easy to check whether (3.114) does this. Suppose we have a solution for some $\bar{u}(z)$ and $N^2(z)$ which describes a wave propagating in the positive direction. Then we should obtain a solution describing a wave propagating in the negative direction by letting $x \to -x$, $c \to -c$ and $u \to -\bar{u}$. Examining (3.72) and (3.91), we find that r remains the same and s changes sign. For λ, we note by (3.45), (3.48), (3.68) and (3.70) that ϕ and $D^{1,0}$ are independent of the sign while $D, \phi^{1,0}$ depend on the sign, which ends up with the expression of λ, i.e., (3.110), depending on the sign. On the other hand, $A(x,t)$ will change sign itself since $u = \psi_z$ changes sign, as well as the derivatives with respect to x. With all these incorporated into (3.114), it is found that the resulting equation is exactly the same, i.e., it does hold for the propagation in both directions.

The equation (3.114) is the mKdV equation which describes the case when

the wave amplitudes are large. As stated at the beginning of this chapter, it is controlled by the two parameters ϵ and μ, one of which comes from the extension of the infinitesimal theory and the other from long-wave theory. When $\epsilon \gg \mu$, the waves are dominantly nonlinear and tend to steepen and break; when $\mu \gg \epsilon$, we have linear dispersive waves. Note however that this dispersive term is not the same dispersive term one obtains from the linear nonhydrostatic equations. The dispersion is only an approximate dispersion valid in the long-wave limit.

3.3 Application to our special case.

The theory and the nondimensional formulation derived in the above section is a general result for flows with any stratification and shear velocity. Our purpose is to examine to what extent this theory predicts the evolution of long waves in the fully nonlinear numerical model (IGWsim). Therefore, we need to select some particular case and apply the theory to it for comparison. In our numerical experiments described in chapter 2 the background flow is, instead of shear, a uniform velocity field. Thus, in this section, we will apply the theory to such a flow, and calculate the corresponding eigenvalue (linear phase speed), vertical modes and coefficients. This work involves the following: first, the equations and expressions are simplified

by setting $\bar{u} = constant$; second, dimensions of variables and coefficients are defined, and the whole system is transformed back to the physical domain accordingly; third, a summary of all dimensional equation systems and formulations, based on which numerical solutions are sought, is given for convenient reference; and finally, some solutions are presented as examples.

3.3.1 Simplification of r, s, λ expressions.

For the simple hydrology considered here, i.e. constant $\bar{u}$, all terms involving derivatives of $(\bar{u}-c)$ in the relevant equations and expressions vanish. Taking the derivative of (3.45) with respect to z and multiplying it by ϕ we have

$$\phi\phi_{zzz} - \phi_{zz}\phi_z = \frac{G'\bar{\rho}_{zz}}{(\bar{u}-c)^2}\phi^2. \tag{3.115}$$

Substituting this into (3.73) and partially integrating it and (3.74) as well, we get

$$r = \frac{I_r}{I} = \frac{-\frac{3}{2}\int_0^1 \phi_z^3 dz}{2\int_0^1 \phi_z^2 dz}, \tag{3.116}$$

and similarly,

$$s = \frac{I_s}{I} = \frac{(\bar{u}-c)\int_0^1 \phi^2 dz}{2\int_0^1 \phi_z^2 dz}. \tag{3.117}$$

As for λ, we first eliminate the terms involving $\phi_{zzz}, \phi_{zzz}^{1,0}$ by partial integration, then substitute these and the expressions for $\phi_{zz}^{1,0}, \phi_{zz}$ ((3.45) and (3.68)) into the expression

(3.110), thus finally expressing I_λ in terms of ϕ, ϕ_z, $\phi^{1,0}$, $\phi_z^{1,0}$ and $\bar{\rho}_z$:

$$\begin{aligned} I_\lambda &= \frac{1}{(\bar{u}-c)^3}\int_0^1 \left\{ -12G\bar{\rho}_z\,\phi\phi_z\phi^{1,0} - 6G\bar{\rho}_z\,\phi^2\phi_z^{1,0} + \frac{6(G\rho_z)^2}{(u-c)^3}\phi^4 \right. \\ &\quad + \frac{18G\bar{\rho}_z}{(\bar{u}-c)}\phi^2\phi_z^2 + \frac{30rG\bar{\rho}_z}{(\bar{u}-c)}\phi^2\phi_z - 8rG\rho_z\,\phi\phi^{1,0} \\ &\quad \left. + \frac{12r^2G\bar{\rho}_z}{(\bar{u}-c)}\phi^2 \right\} dz, \end{aligned} \tag{3.118}$$

and consequently,

$$\lambda = \frac{I_\lambda}{I}. \tag{3.119}$$

3.3.2 Conversion to dimensional form.

We must remember that the numerical simulation is in the described physical domain while the above theoretical analysis is carried out dimensionlessly. In order to compare them later we now convert the analysis to dimensional form. This can be done quite easily. Remember that one controlling parameter G and one scaling parameter μ were introduced when we did nondimensionalization. Now by replacing $G\rho_z$ with $-N^2$ and μ with 1 in the previous section, and regarding all variables as dimensional, we can immediately obtain the dimensional form of the system. The dimensions of the three coefficients r, s and λ depend on how we define the dimensions for the vertical modes. Doing this dimensional analysis checks the dimensional consistency of the mKdV equation. In the following, we first define the dimensions of the variables in the zero

order problem. Based on this, the dimensions of other variables and coefficients are found. Then we implement conversion and summarize the dimensional system.

The stream function perturbation has a volume flux dimensional scale ϵUH, and the density perturbation of course has a density dimensional scale of $\epsilon\rho_0$. These, by the dimensionless forms (3.24) and (3.25), can be written as

$$\begin{aligned}
\psi_p^* &= \epsilon\psi^* = \epsilon UH\psi \\
&= (\epsilon UHA)\phi + (\epsilon UHA)^2\frac{\phi^{1,0}}{UH} + (\epsilon UHA)_{xx}\frac{\phi^{0,1}H^2}{L^2} \\
&\quad +(\epsilon UHA)^3\frac{\phi^{2,0}}{(UH)^2}\cdots \\
&= A^*\phi + A^{*2}\phi^{1,0*} + A^*_{x^*x^*}\phi^{0,1*} + A^{*3}\phi^{2,0*}\cdots, \qquad (3.120)
\end{aligned}$$

$$\begin{aligned}
\rho_p^* &= \epsilon\rho^* = \epsilon\rho_0\rho \\
&= (\epsilon UHA)\frac{\rho_0 D}{UH} + (\epsilon UHA)^2\frac{\rho_0 D^{1,0}}{(UH)^2} + (\epsilon UHA)_{xx}\frac{\rho_0 D^{0,1}H}{UL^2} \\
&\quad +(\epsilon UHA)^3\frac{\rho_0 D^{2,0}}{(UH)^3}\cdots \\
&= A^*D^* + A^{*2}D^{1,0*} + A^*_{x^*x^*}D^{0,1*} + A^{*3}D^{2,0*}\cdots, \qquad (3.121)
\end{aligned}$$

where "ϵ" represents the dimensional form and the subscript p stands for perturbation. Obviously, the dimensional scales of the quantities in the above are:

$$[A^*] = \epsilon UH,\ [\phi] = 1,\ [\phi^{1,0*}] = 1/UH,$$

$$[\phi^{0,1*}] = H^2,\ [\phi^{2,0*}] = 1/(UH)^2,\ [D^*] = \rho_0/UH,$$

$$[D^{1,0*}] = \rho_0/(UH)^2,\ [D^{0,1*}] = \rho_0 H/U,\ [D^{2,0*}] = \rho_0/(UH)^3, \qquad (3.122)$$

where [ ] denotes the dimensional scale of a variable. Actually, we are free to choose a dimension for A^*. When this is done, the dimensions of vertical modes $\phi^{i,j*}, D^{i,j*}$ are determined consequently. What we did here is to first define the dimensional scale of A^* as that of the stream perturbation, thus leave ϕ dimensionless with a scale of one, and then determine the dimensional scales of others.

Using

$$z = z^*/H,\ (\bar{u} - c) = (\bar{u}^* - c^*)/U,\ \partial/\partial z = H\partial/\partial z^*,$$

$$\frac{G\bar{\rho}_z}{(\bar{u} - c)^2}\phi = \phi_{zz} = H^2\phi_{z^*z^*} = -H^2\frac{N^2}{(u^* - c^*)^2}\phi,$$

and the above results, we can rewrite r, s, λ expressions as

$$r = -\frac{3}{4}\frac{\int_0^H \phi_{z^*}^3 dz^*}{\int_0^H \phi_{z^*}^2 dz^*}H = r^* H, \qquad (3.123)$$

$$s = \frac{(\bar{u}^* - c^*)}{2}\frac{\int_0^H \phi^2 dz^*}{\int_0^H \phi_{z^*}^2 dz^*}\frac{1}{UH^2} = \frac{s^*}{UH^2}, \qquad (3.124)$$

and similarly

$$\lambda = \lambda^* UH^2. \qquad (3.125)$$

These indicate that r^*, s^*, λ^* are defined as those calculated by using dimensional quantities and thus have the dimensions $1/H, UH^2$ and $1/UH^2$, respectively.

Up to this point, the dimensions for the whole system have been defined. The conversion of the system back to the physical domain can be done by substituting $-N^2$ for $G\bar{\rho}_z$, 1 for μ, and regarding all variables in the system as dimensional ones. Next, for convenience and clearness, the whole dimensionalized system, based on which the theoretical calculations are carried out for our particular case, is summarized in the following (with "$*$" dropped):

the perturbations at some level z are

$$\psi_p = A\phi + A^2\phi^{1,0} + A_{xx}\phi^{0,1} + A^3\phi^{2,0}\cdots \tag{3.126}$$

$$\rho_p = AD + A^2D^{1,0} + A_{xx}D^{0,1} + A^3D^{2,0}\cdots, \tag{3.127}$$

where the wave profile A is governed by

$$A_t + cA_x - 2rAA_x - sA_{xxx} - \lambda A^2A_x = 0. \tag{3.128}$$

The nonlinear and dispersive coefficients are:

$$r = \frac{-\frac{3}{2}\int_0^H \phi_z^3 dz}{2\int_0^H \phi_z^2 dz}, \tag{3.129}$$

$$s = (\bar{u}-c)\frac{\int_0^H \phi^2 dz}{2\int_0^H \phi_z^2 dz}, \tag{3.130}$$

$$\lambda = \frac{I_\lambda}{2\int_0^H \phi_z^2 dz}, \tag{3.131}$$

with

$$I_\lambda = -\frac{1}{(\bar{u}-c)^2}\int_0^H \left[12N^2\phi\phi_z\phi^{1,0} + 6N^2\phi^2\phi_z^{1,0} + \frac{6(N^2)^2}{(\bar{u}-c)^3}\phi^4\right.$$

$$-\frac{18N^2}{(\bar{u}-c)}\phi^2\phi_z^2-\frac{30rN^2}{(\bar{u}-c)}\phi^2\phi_z+8rN^2\phi\phi^{1,0}$$
$$-\frac{12r^2N^2}{(\bar{u}-c)}\phi^2\Bigg]dz. \tag{3.132}$$

The vertical modes appearing in these expressions are determined from:

$$\left.\begin{aligned}\phi_{zz}+\tfrac{N^2}{(\bar{u}-c)^2}\phi &= 0\\ \phi(0)=\phi(H) &= 0\end{aligned}\right\}, \tag{3.133}$$

which also gives the eigenvalue c (only the largest eigenvalue c corresponding to the mode-one wave is considered here) that appears in the mKdV as the linear phase speed;

$$\left.\begin{aligned}\phi^{1,0}_{zz}+\tfrac{N^2}{(\bar{u}-c)^2}\phi^{1,0} &= -\tfrac{(N^2)_z}{(\bar{u}-c)^3}\phi^2+r\tfrac{2N^2}{(u-c)^3}\phi\\ \phi^{1,0}(0)=\phi^{1,0}(H) &= 0\end{aligned}\right\}; \tag{3.134}$$

$$\left.\begin{aligned}\phi^{0,1}_{zz}+\tfrac{N^2}{(\bar{u}-c)^2}\phi^{0,1} &= -\phi+s\tfrac{2N^2}{(u-c)^3}\phi\\ \phi^{0,1}(0)=\phi^{0,1}(H) &= 0\end{aligned}\right\}; \tag{3.135}$$

$$\left.\begin{aligned}\phi^{2,0}_{zz}+\tfrac{N^2}{(\bar{u}-c)^2}\phi^{2,0} &= -2\tfrac{(N^2)_z}{(\bar{u}-c)^3}\phi\phi^{1,0}-\tfrac{(N^2)_{zz}}{2(u-c)^4}\phi^3\\ &\quad +3r\tfrac{(N^2)_z}{(u-c)^4}\phi^2-r\tfrac{N^2}{(u-c)^4}\phi\phi_z\\ &\quad +r\tfrac{8N^2}{3(u-c)^3}\phi^{1,0}-r^2\tfrac{4N^2}{(u-c)^4}\phi\\ &\quad +\lambda\tfrac{2N^2}{3(\bar{u}-c)^3}\phi\\ \phi^{2,0}(0)=\phi^{2,0}(H) &= 0\end{aligned}\right\}, \tag{3.136}$$

and

$$D = \frac{\bar{\rho}_z}{(\bar{u}-c)}\phi, \tag{3.137}$$

$$D^{1,0} = \frac{1}{(\bar{u}-c)}\left[\bar{\rho}_z\phi^{1,0} + \frac{\bar{\rho}_{zz}}{2(\bar{u}-c)}\phi^2 - r\frac{\bar{\rho}_z}{(\bar{u}-c)}\phi\right], \tag{3.138}$$

$$D^{0,1} = \frac{\bar{\rho}_z}{(\bar{u}-c)}\phi^{0,1} - s\frac{\bar{\rho}_z}{(\bar{u}-c)^2}\phi, \tag{3.139}$$

$$\begin{aligned} D^{2,0} = & \frac{\bar{\rho}_z}{(\bar{u}-c)}\phi^{2,0} \\ & + \frac{1}{3(\bar{u}-c)}(\phi D_z^{1,0} + 2D_z\phi^{1,0} - 2\phi_z D^{1,0} - D\phi_z^{1,0} - 4rD^{1,0} - \lambda D), \end{aligned} \tag{3.140}$$

where the correctness of the coefficients r, s, λ ensures the solvability of the above inhomogeneous equation systems.

Solving this problem, one would adopt a solution procedure like this: first, solve the eigenvalue problem (3.133); second, calculate r, s, λ and solve (3.134) to (3.136) for the other vertical modes; and third, solve the mKdV equation (3.128) for a given initial wave profile. These will be done in the following two sections.

3.4 Solution for vertical modes.

The four problems (3.133) to (3.136) are solved numerically using a C-code EIG. Note that for each of them, there are an infinite number of solutions. A unique solution

can be selected by imposing a further condition. The solution to (3.133) is uniquely determined by setting $\max(\phi) = 1$. The general solution of (3.134) has the form

$$\phi^{1,0} = \phi^{1,0*} + \alpha^{1,0}\phi, \tag{3.141}$$

where $\phi^{1,0*}$ is a particular solution determined by a boundary condition

$$\phi^{1,0*}(0) = \phi_z^{1,0*}(0) = 0, \tag{3.142}$$

$\alpha^{1,0}$ is an arbitrary constant, the selection of which will be discussed in more detail in the next chapter, in conjunction with the measurement of wave profiles. The general solutions of (3.135) and (3.136) have a form similar to (3.141). The numerical solutions of (3.134) to (3.136) are obtained by integrating from $z = 0$ with two boundary conditions like (3.142). The values of r, s and λ given by (3.116), (3.117) and (3.119) guarantee that $\phi^{1,0}$, $\phi^{0,1}$, $\phi^{2,0}$ are zero at $z = H$. Note that only ϕ and $\phi^{1,0}$ are required in order to evaluate r, s, λ. We will see later that $\phi^{1,0}$ is also needed to obtain the initial wave profile from the output of the model IGWsim. Although $\phi^{0,1}$ and $\phi^{2,0}$ are not used in any formulae, the equations for them are integrated to verify the correctness of the coefficients. Note that ϕ is the first vertical normal mode while $\phi^{1,0}$, $\phi^{0,1}$ and $\phi^{2,0}$ are in general combinations of all the linear vertical modes $\phi_n(z)$.

Figure 3.1-3.4 are the plots of the vertical modes for the case with the stepwise $N_1^2(z)$ given by (2.38), $H = 360\,\mathrm{m}$ and $z_r = 260\,\mathrm{m}$. It can be seen that $\phi(H), \phi^{1,0}(H), \phi^{0,1}(H)$ and $\phi^{2,0}(H)$ are zero, indicating that r, s and λ are calculated to sufficient accuracy.

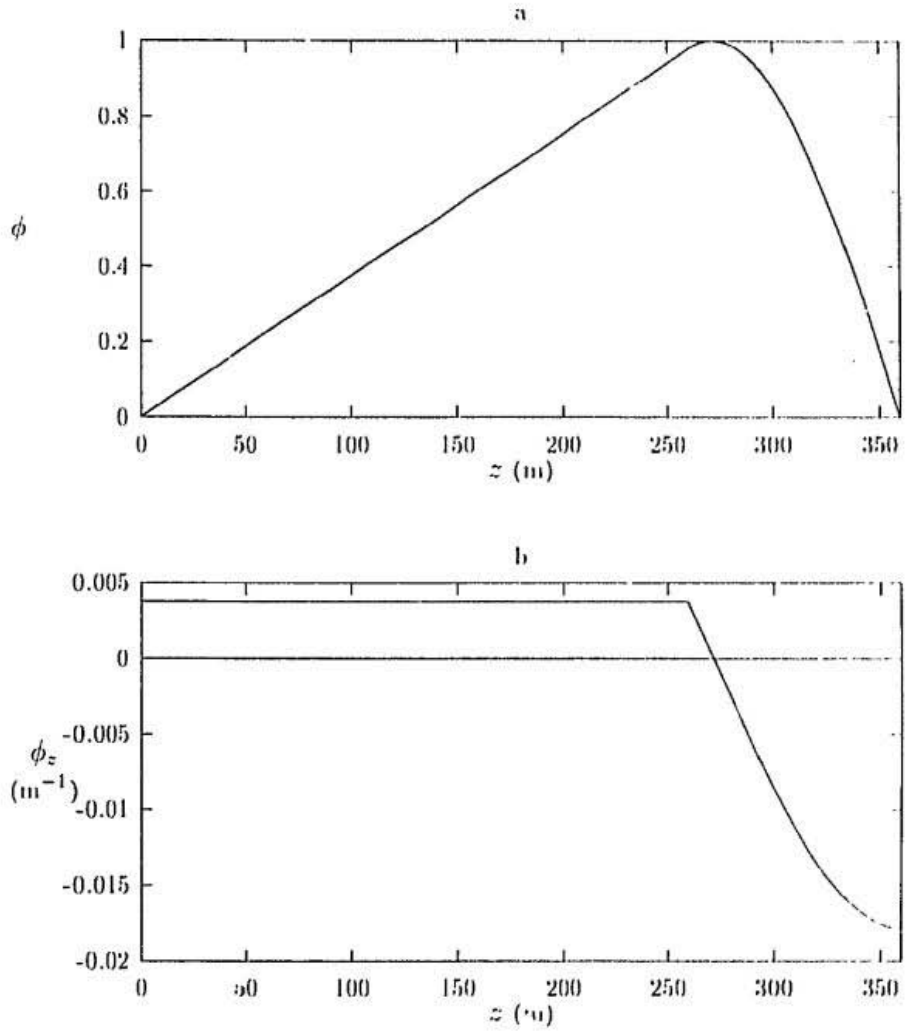

Figure 3.1: Zero-order vertical mode (mode-one only). (a). $\phi(z)$. (b). $\phi_z(z)$.

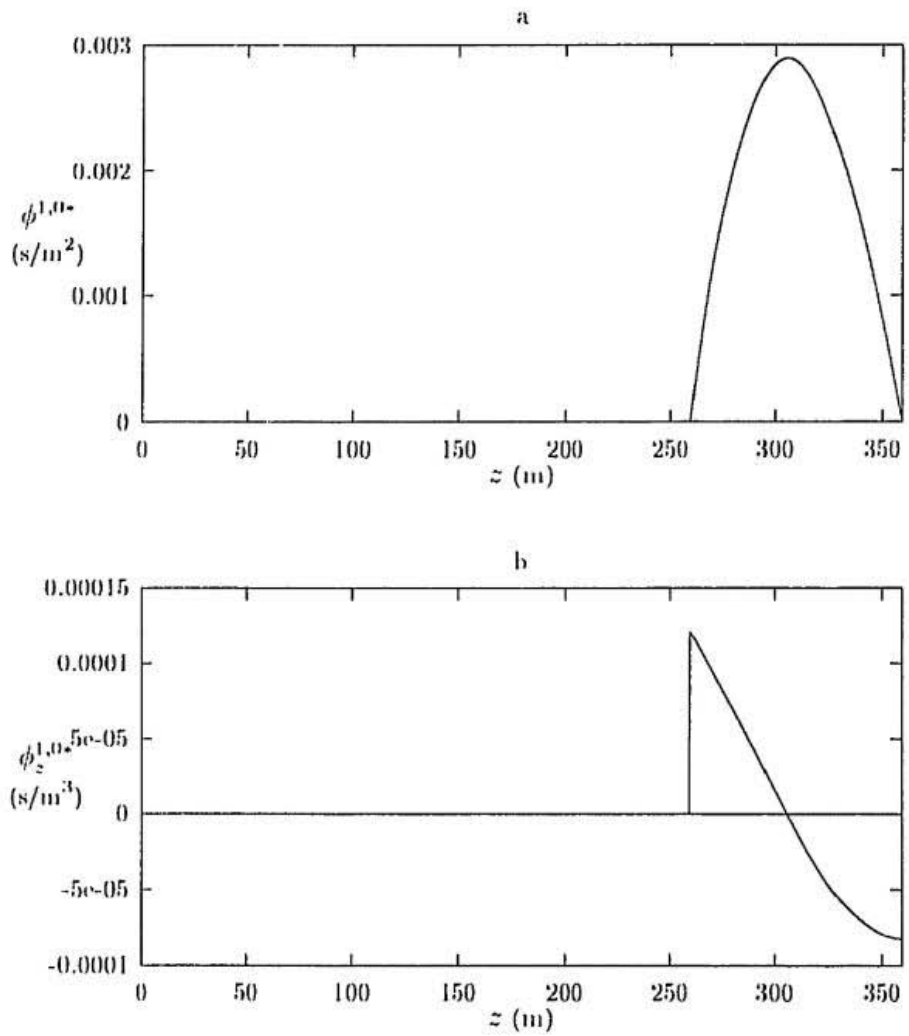

Figure 3.2: First-order vertical mode (mode-one only). (a). $\phi^{1,0*}(z)$. (b). $\phi_z^{1,0*}(z)$.

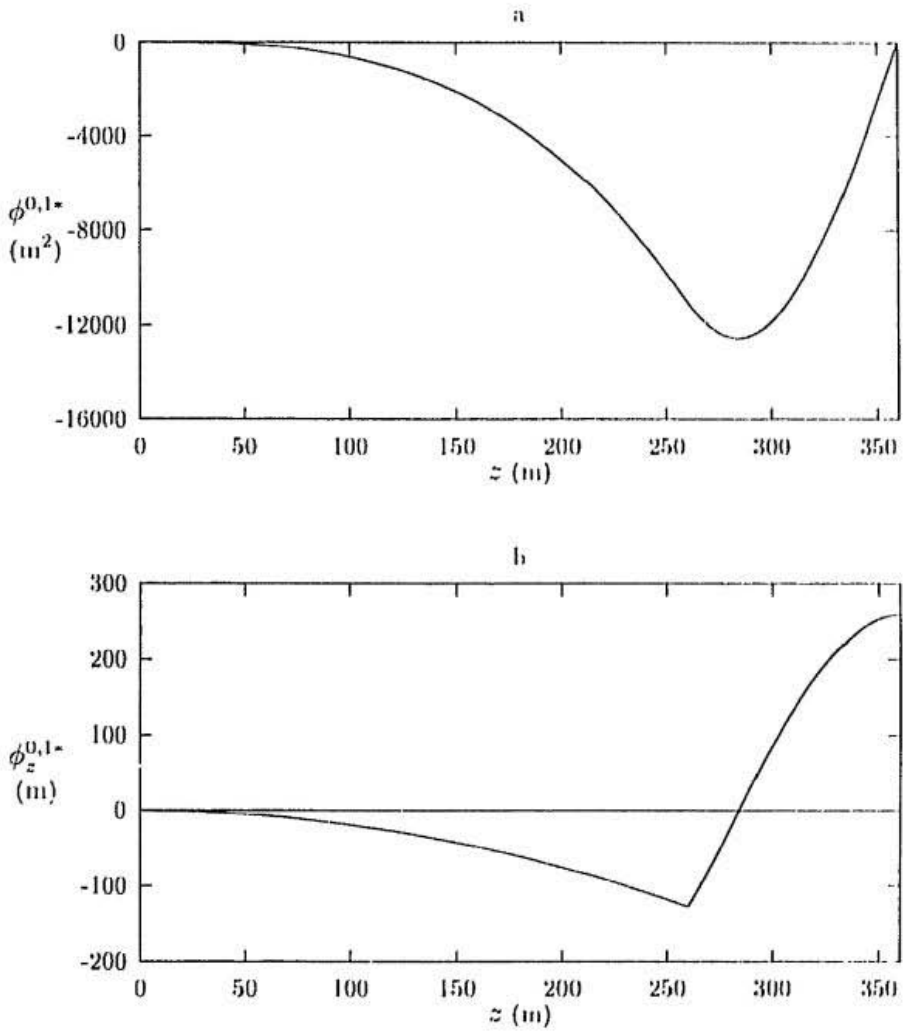

Figure 3.3: First-order vertical mode (mode-one only). (a). $\phi^{0,1*}(z)$. (b). $\phi_z^{0,1*}(z)$.

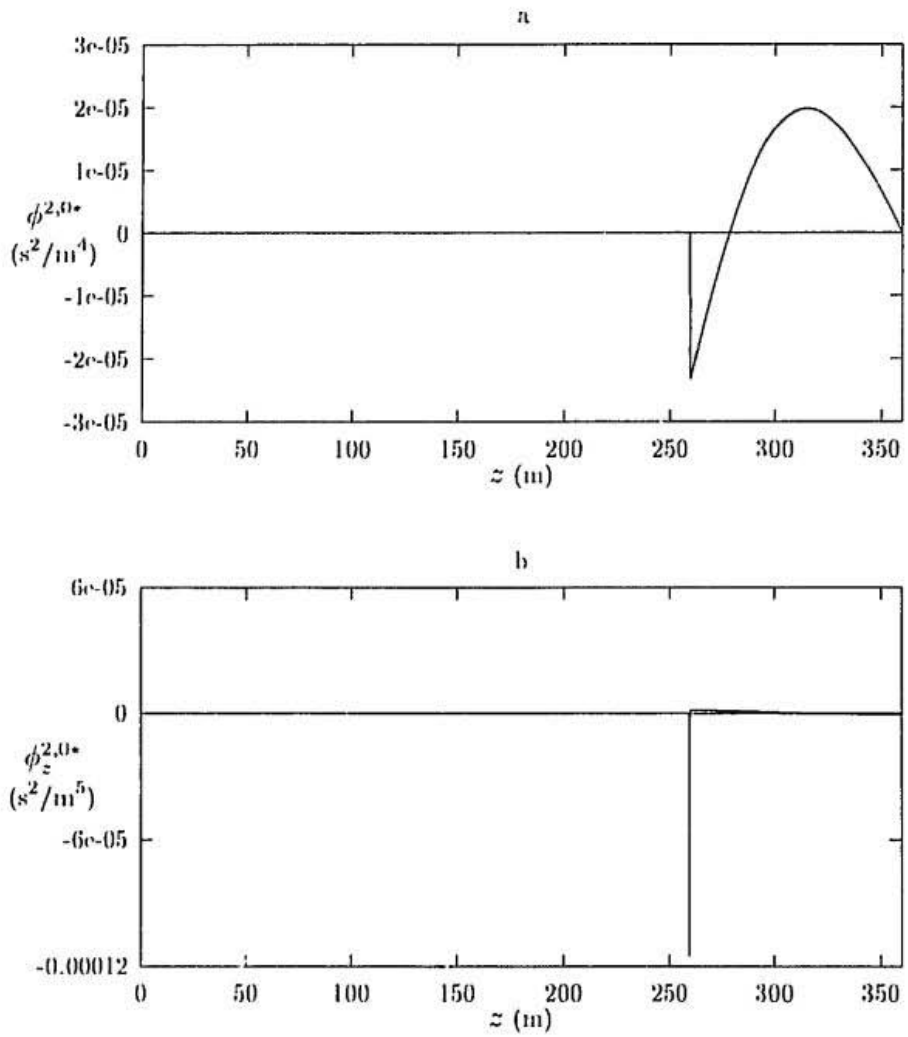

Figure 3.4: Second-order vertical mode (mode-one only). (a). $\phi^{2,0*}(z)$. (b). $\phi_z^{2,0*}(z)$.

3.5 Numerical solution of mKdV equation

Up to now, we have theoretically shown that, to $O(\epsilon^2)$, the evolution of long nonlinear perturbation waves is governed by the mKdV equation (3.128), and have correctly calculated the associated coefficients. To compare this theory with the model results, we must solve this time dependent mKdV equation on a given initial wave profile. This is done numerically using the pseudospectral method developed by Fornberg & Whitham [1978]. This method uses a Fourier transform treatment of the space dependence, together with a leap-frog scheme in time. In this section, this method is briefly described and then applied to our problem.

3.5.1 Numerical method.

For simplicity, let us drop the advection term cA_x in (3.128), which can be eliminated by changing to a reference frame moving with speed c. Thus we have the basic mKdV equation of the form

$$A_t - 2rAA_x - sA_{xxx} - \lambda A^2 A_x = 0. \tag{3.143}$$

When discretized, A_t is approximated by the leap-frog scheme with a truncation error of the order of $O(\Delta t^2)$

$$\frac{A(x,t+\Delta t)-A(x,t-\Delta t)}{2\Delta t}=A_t+O(\Delta t^2), \tag{3.144}$$

where Δt is the time increment, the restriction on the size of Δt will be specified later. The space derivative terms are handled in a spectral way. First, the computational space domain $[l_1,l_2]$ is discretized by $2N$ equidistant points with a spacing $\Delta x = L/(2N)$, where $L=l_2-l_1$. Then forward and backward Fast Fourier Transforming (FFT hereafter) are performed on the domain according to

$$\begin{aligned}\breve{A}(k_n,t) &= F\{A(x_j,t)\}\\ &= \frac{1}{\sqrt{2N}}\sum_{j=0}^{2N-1}A(j\Delta x,t)e^{-ik_n(j\Delta x)},\end{aligned} \tag{3.145}$$

and

$$\begin{aligned}A(x_j,t)=A(j\Delta x,t) &= F^{-1}\{\breve{A}(k_n,t)\}\\ &= \frac{1}{\sqrt{2N}}\sum_{n=0}^{2N-1}\breve{A}(k_n,t)e^{-ik_n(j\Delta x)},\end{aligned} \tag{3.146}$$

where F and F^{-1} denote the forward and backward FFT, respectively, A and $\breve{A}$ are the Fourier pair, and the wavenumber is given by

$$k_n=\frac{2\pi}{L}n,\quad n=0,1,\cdots 2N-1.$$

Note that to ensure the efficiency of the FFT, the number of grid points needs to be a power of 2.

The idea is to forward time step in the physical domain instead of in the spectral domain, thus saving computing expenditure. Therefore, derivatives are taken of (3.146) with respect to x to give

$$A_x(x,t) = F^{-1}\left\{\frac{\partial}{\partial x}F\{A\}\right\} = i\,F^{-1}\{k_n F\{A\}\}, \tag{3.147}$$

$$A_{xxx}(x,t) = F^{-1}\left\{\frac{\partial^3}{\partial x^3}F\{A\}\right\} = -i\,F^{-1}\{k_n^3 F\{A\}\}. \tag{3.148}$$

One advantage of this approximation is that information from all of the discretized points, instead of from only several surrounding points as in the usual finite differencing scheme, has been used. This will give a more accurate solution.

Discretizing (3.143) by the use of (3.144), (3.147) and (3.148), we have

$$A(x,t+\Delta t) - A(x,t-\Delta t) - 4\Delta t\, r\, A F^{-1}\{i\,k_n F\{A\}\}$$
$$+2\Delta t\, s\, F^{-1}\{i\,k_n^3 F\{A\}\} - 2\Delta t\,\lambda\, A^2 F^{-1}\{i\,k_n F\{A\}\} = 0. \tag{3.149}$$

Fornberg & Whitham [1978] then modified this equation to

$$A(x,t+\Delta t) - A(x,t-\Delta t) - 4\Delta t\, r\, A F^{-1}\{i\,k_n F\{A\}\}$$
$$+2F^{-1}\{i\,\sin(k_n^3\, s\,\Delta t) F\{A\}\} - 2\Delta t\,\lambda\, A^2 F^{-1}\{i\,k_n F\{A\}\} = 0. \tag{3.150}$$

The reason for this modification is that it is more accurate for short wave components.

Since $k_n^3\, s\, \Delta t = \sin(k_n^3\, s\, \Delta t) + O(\Delta t^3)$, $k_n^3\, s\, \Delta t$ in the dispersive term has been replaced by $\sin(k_n^3\, s\, \Delta t)$. In our long wave consideration the maximum wave number $k_N = 2\pi/\Delta x$ involved is usually considerably smaller than one. The error introduced in this replacement is an order of magnitude smaller than the truncation error already introduced by the time discretization. This replacement has important significance, indeed. In general, a consistent difference approximation to (3.143) is accurate enough for low wave numbers (supposing it well satisfies the corresponding criteria), but it will lose accuracy rapidly for increasing wave numbers. At high wave numbers, the controlling scale parameter μ in the nondimensional form (3.113) becomes large over ϵ and the dispersive term dominates, thus the above differential and difference equations reduce to

$$A_t - sA_{xxx} = 0, \tag{3.151}$$

$$A(x, t + \Delta t) - A(x, t - \Delta t) + 2\Delta t\, s\, F^{-1}\{i\, k_n^3 F\{A\}\} = 0, \tag{3.152}$$

respectively, and the modified form becomes

$$A(x, t + \Delta t) - A(x, t - \Delta t) + 2F^{-1}\{i\, \sin(k_n^3\, s\, \Delta t) F\{A\}\} = 0. \tag{3.153}$$

The important difference between (3.152) and (3.153) is that the latter is not subject to any differencing error. That is, any solution of the differential equation (3.151), when discretized with any Δx and Δt, exactly satisfies the modified differencing

equation (3.153) as well, but not (3.152). This can be readily shown. Supposing one solution of (3.151) is $A = e^{ik_n(x-k_n^2 s t)}$. Discretizing it gives

$$A(x, t + \Delta t) = Ae^{-ik_n^3 s \Delta t},$$

$$A(x, t - \Delta t) = Ae^{+ik_n^3 s \Delta t},$$

$$F\{A\} = \delta(k_m - k_n)e^{-ik_n^3 s t},$$

$$F^{-1}\{\sin(k_n^3 s \Delta t)\delta(k_m - k_n)e^{-ik_n^3 s t}\} = A\sin(k_n^3 s \Delta t),$$

thus we immediately have (3.153). δ here denotes a Dirac delta function. So, the modified (3.153) is much better than (3.152) for high wave numbers.

Now it is quite clear that the reason we prefer the modified version (3.150) is that it is much better for high wave numbers and is as good as the original (3.149) for low wave numbers.

3.5.2 Stability.

The time step is determined via stability considerations. Instead of the nonlinear stability, which is hard to deal with, we consider here the linear stability problem corresponding to a linear model equation

$$A_t + 0A_x - sA_{xxx} = 0, \tag{3.154}$$

where θ, originally being $c_0 - 2rA - \lambda A^2$ (c_0 is the linear phase speed relative to the fluid) in the mKdV equation (3.128), is now treated as a constant. This simply assumes that during the integration of the mKdV equation, $c_0 - 2rA - \lambda A^2$ remains under some limit, say θ. Therefore, the condition to be imposed on the time step Δt for the linear model (3.154) is also valid for the corresponding mKdV equation (3.143).

(3.154) is discretized according to the above theory as

$$A(x, t + \Delta t) - A(x, t - \Delta t) + 2\,i\,\theta\,\Delta t F^{-1}\{k_n F\{A\}\}$$
$$-2\,i\,F^{-1}\{-\sin(k_n^3\, s\,\Delta t) F\{A\}\} \;=\; 0. \qquad (3.155)$$

We want to find the condition under which a given wave does not grow with time. Therefore, we substitute a wave of the form

$$A(x, t) = K^m\, e^{i k_n x} = K^{t/\Delta t} e^{i k_n x}$$

into the (3.155), where m is the number of time steps. This gives

$$K^2 - 2\,i\,f(\Delta t, k_n, \theta) K - 1 = 0, \qquad (3.156)$$

where

$$f(\Delta t, k_n, \theta) = \sin(-k_n^3\, s\,\Delta t) - k_n \theta \Delta t. \qquad (3.157)$$

The solutions of (3.156) are

$$K = i\,f \pm \sqrt{1 - f^2}. \tag{3.158}$$

The solution associated with the positive sign is the physical mode and the other is the computational mode. It is obvious that the scheme (3.155) is conditionally stable if and only if f is real and less than one in magnitude. Therefore, we need to find the largest Δt so that

$$|f(\Delta t, k_n, \theta)| < 1 \tag{3.159}$$

is true for all k_n, $n = 0, \pm 1, \cdots, \pm N$. The most severe constraint on Δt is for $k_N = \pm\pi/\Delta x$ which are the largest in magnitude.

We rewrite f as a function of $b = -s\,\Delta t\,k_N^3$

$$f(b, k_N, \theta) = \sin(b) - \frac{b\,\theta}{(-s)k_N^2}$$

and note that f is rapidly oscillating with b. Since θ and s always have the same sign, $f(b) = -f(-b)$. If $f = 0$ the corresponding wave would be a stationary, constant profile as a result of balancing between dispersion and advection. It can be expected that there exists a value of b_0, corresponding to the first intersection between f and either -1 or 1, beyond which the condition $|f| < 1$ might be violated. Figure 3.5 shows the plot of f for $(-s) > 0$ and $\theta > 0$. It can be seen that for any $b \prec b_0$ (3.159)

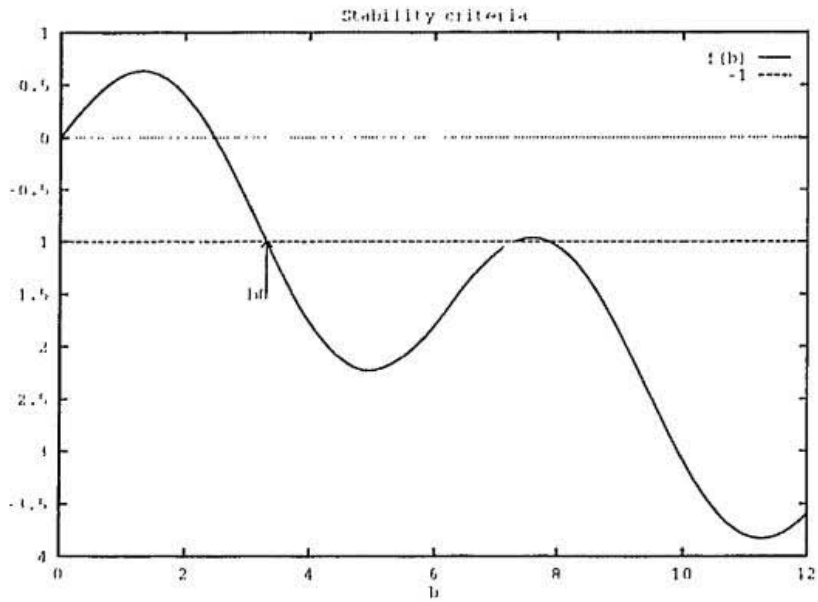

Figure 3.5: The plot of function $f(b, k_N, \theta)$. The first intersection b_0 with -1 is the criterion

is guaranteed, where b_0 is the first root of

$$\sin(b) - \frac{b\,\theta}{(-s)k_N^2} = -1.$$

Therefore, the stability condition is set up (for $k_N = +\pi/\Delta x$) as

$$\frac{\Delta t}{\Delta x^3} < \frac{b_0}{(-s)\pi^3} \tag{3.160}$$

In practice, Δt is taken as about a quarter of the value given by (3.150). Tests show this is adequate. The scheme will become unstable for Δt approaching the criterion.

3.5.3 Test.

A C program called KDV for solving KdV type equations has been coded according to the described numerical method. Because the leapfrog scheme requires initial conditions on the first two time levels, we first use a forward time step to advance the given initial wave. As for the well known weakness of the leapfrog scheme, i.e., the possibility of separation of the solution between two successive time levels, a coupling technique has been used. When we have calculated the solution up to levels $t - \Delta t$, t and $t + \Delta t$, we introduce half levels at $t - \frac{1}{2}\Delta t$ and $t + \frac{1}{2}\Delta t$, as averages of adjacent levels, and calculate one step up to level $t + \frac{3}{2}\Delta t$. Then averaging $t - \frac{1}{2}\Delta t$, $t + \frac{1}{2}\Delta t$ and $t + \frac{1}{2}\Delta t$, $t + \frac{3}{2}\Delta t$, we go back to levels t and $t + \Delta t$ and proceed the calculation from there. This process is repeated every 50 time steps.

Before the program KDV was used to solve our mKdV equation (3.128), it was tested against the situations where analytical solutions exist, such as an advection solution, a dispersive solution and solitons. Figure 3.6 shows that the numerical solutions are indistinguishable from the analytical solutions for a single propagating soliton and for two colliding solitons.

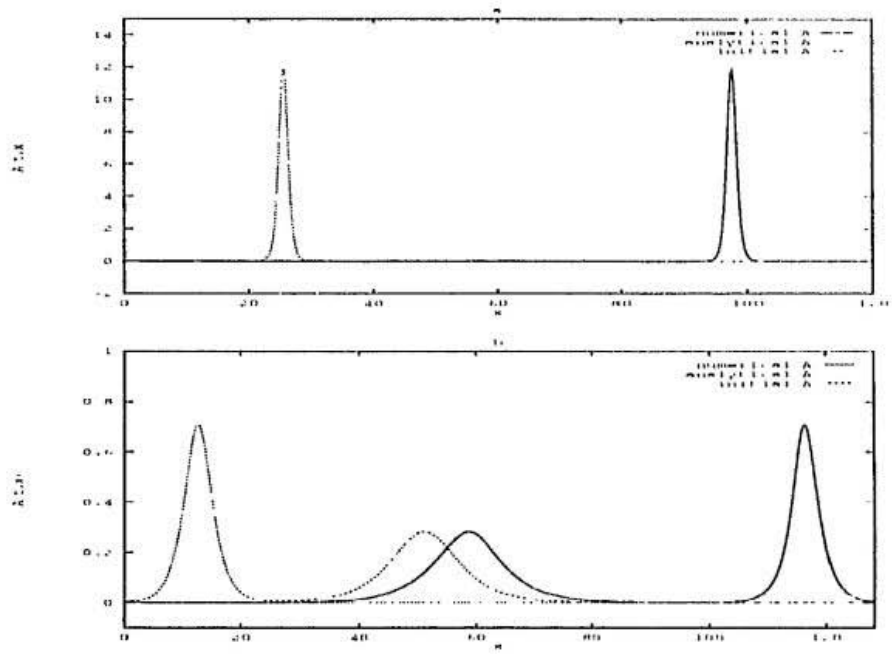

Figure 3.6: Tests of the numerical solutions (with 512 grid points and $dt = 0.001$) against the analytic solitary solutions. (a). Numerical and analytical solutions of KdV equation. Both evolve from the same initial wave and are indistinguishable after 18000 steps. (b). Numerical and analytical colliding soliton solutions of mKdV equation. The numerical wave profile is indistinguishable from the analytical solution after 400000 steps.

Chapter 4

Theory vs. Numerical Model

In chapter 2, the numerical model which is used to study the generation and evolution of IGWs was described. In chapter 3, the theoretical analysis of long, weakly nonlinear IGWs trapped in a horizontally uniform vertical extent was derived following Lee and Beardsley, which indicates that the evolution of the waves is governed by a mKdV equation. If this theory is valid, it should be able to produce the same features of IGWs as observed in the numerical experiments, such as a steep front, undular bore at the rear of the front, nonlinear propagation speed, etc.

We mentioned in the introduction of chapter 3 that the theory was developed by Long [1956, 1965, 1972] and Benjamin [1966], and extended by Benney [1966] and Lee & Beardsley [1974]. Benney derived a KdV equation for IGWs. Lee and

Beardsley obtained a mKdV equation which is a bit different from ours in that they included non-Boussinesq effects by introducing a third parameter. By comparing this theory with laboratory experiments and observation in Massachusetts Bay, Lee and Beardsley showed that the theory produces the main features of IGWs developed from a front. Since there was no observations of an initial wave profile their comparison was only qualitative. Gear & Grimshaw [1983] studied the second-order theory of solitons in shallow fluids and derived the second-order corrections to the wave profile and phase speed predicted by the first-order theory. The second-order correction should improve the first-order theory, but this was not verified by comparisons with observations, experimental or numerical results in their paper.

No one has conducted fully nonlinear numerical modelling of the problem using Euler's equations and quantitatively compared the model results with the theory. In this chapter such comparisons are carried out. We want to see whether there is good quantitative agreement with the model results and determine when, and how much, the second-order nonlinearity improves the first-order KdV theory. For this purpose, we first extract a temporal and horizontal variation $B(t,x) = A(t,x)/c_0$ (which we refer to as the wave profile) from the model output. $B(t,x)$ is determined by an infinite series and hence can not be computed exactly. Instead an approximate B profile is calculated. The approximation used to find B varies with z. Thus, strictly

speaking, B is a function of a parameter z_d where z_d is the value of z at which this approximation is made. The validity of the approximation is indicated by small variations of B with z_d. The extraction of B also involves the selection of $\alpha^{1,0}$ in (3.141), which was left unsolved in chapter 3. It is shown that only a semi-infinite range of values of $\alpha^{1,0}$ are possible. This is done in secton 4.1. In section 4.2, an efficient resolution of the model is selected based on test runs. Then in section 4.3 the derived theory is compared with the model results for different background states, and discussion follows.

In the following, the wave profiles are usually denoted by two numbers, e.g. $B330\_10$, etc. The first number (i.e., 330) indicates the height z_d at which the wave is measured, and the second (i.e., 10) is the output number indicating the time of evolution (actual time being 1600s multiplied by this number). Other subscripts may be attached when neccessary.

4.1 Extraction of wave profile

The model IGWsim stores the pressure gradient field, the density field and the velocity field. A wave profile must be extracted from the model output for comparison. This can be done by using perturbation expansions (3.126) and (3.127). Dividing (3.126)

by the propagation speed relative to the fluid ($c_0 = c - u$) and substituting (3.137) to (3.140) for $D^{i,j}$ in (3.127), we define η_ψ and η_d via

$$\eta_\psi = \frac{\psi_p}{c_0} = B\phi + B^2 c_0 \phi^{1,0} + B_{xx}\phi^{0,1} + B^3 c_0^2 \phi^{2,0} + \cdots \tag{4.1}$$

$$\begin{aligned}
\eta_d = \frac{g\rho_p}{N^2} &= B\phi + B^2 c_0 \left[\phi^{1,0} + \frac{r}{c_0}\phi - \frac{(N^2)_z}{2N^2 c_0}\phi^2\right] \\
&\quad + B_{xx}\left[\phi^{0,1} + \frac{s}{c_0}\phi\right] \\
&\quad + B^3 c_0^2 \left[\phi^2 + \frac{r}{3c_0^2}\phi\phi_z + \frac{4r}{3c_0}\phi^{1,0} + \frac{4r^2}{3c_0^2}\phi + \frac{\lambda}{3c_0}\phi \right. \\
&\quad \left. - \frac{(N^2)_z}{N^2 c_0}\phi\phi^{1,0} - \frac{r(N^2)_z}{N^2 c_0^2}\phi^2 - \frac{r(N^2)_z}{3N^2 c_0^2}\phi^2\phi_z\right] + \cdots \\
&= B\phi + B^2 E^{1,0} + B_{xx}E^{0,1} + B^3 E^{2,0} + \cdots .
\end{aligned} \tag{4.2}$$

where $B(t,x) = A/c_0$ has a length dimension and is governed by

$$B_t + cB_x - 2rc_0 BB_x - sB_{xxx} - \lambda c_0^2 B^2 B_x = 0, \tag{4.3}$$

which is the mKdV equation. Relations (4.1) and (4.2) are exact. The η_ψ and η_d on the left hand side can be viewed, to first order only, as the vertical displacement of streamlines and isopycnals respectively, which reach level z when disturbed.

Expressions (4.1) and (4.2) say that the perturbations can be expressed in terms of a depth independent wave profile $B(t,x)$ and the vertical modes $\phi^{i,j}$. It should be also pointed out that the theoretical derivation assumes that only a single mode is present. Nonlinear interaction between modes has been ignored. In general,

nonlinearity will result in the generation of higher mode waves from a mode-one wave. This is taken partially into account by the functions $E^{i,j}(z)$ which are in general linear combinations of all the vertical linear modes. We do not call $B(t,x)$ the vertical mode amplitude since, because of the nonlinear terms in (4.2), B is not a direct measure of the amplitude. As will be shown, $\phi^{1,0}$ is not unique and different choices of it give different Bs. Yet the wave amplitude is unchanged, as measured by the actual isopycnal displacements.

In the following, we will obtain B from the density perturbation rather than from the stream function perturbation. The reason is that the model output makes it easy to determine ρ_p. The stream function perturbation would be harder to calculate.

4.1.1 About the wave profile $B(t,x)$

We have shown in chapter 3 that the vertical modes $\phi^{i,j}$ have the form

$$\phi^{i,j} = \phi^{i,j*} + \alpha^{i,j}\phi, \tag{4.4}$$

where $\phi^{i,j*}$ are particular solutions of inhomogeneous equations determined by $\phi^{i,j*}(0) = \phi_z^{i,j*}(0) = 0$ and $\alpha^{i,j}$ are arbitrary constants multiplying the homogeneous solution ϕ. The involvement of $\alpha^{i,j}$ in $E^{i,j}$ indicates that different $\alpha^{i,j}$ define different B. To see

this, let us take $\alpha^{1,0}$ for example and assume other $\alpha^{i,j}$ fixed.

$$\begin{aligned}\eta_d &= B\phi + B^2 c_0\left[\phi^{1,0*} + (\alpha^{1,0} + \frac{r}{c_0})\phi - \frac{(N^2)_z}{2N^2 c_0}\phi^2\right] + B_{xx}E^{0,1} + B^3E^{2,0} + \cdots \\ &= (B + \alpha^{1,0}B^2)\phi + B^2 c_0 E^{1,0*} \\ &\quad + B_{xx}E^{0,1} + B^3E^{2,0} + \cdots, \end{aligned} \tag{4.5}$$

where $E^{1,0*}$ is $E^{1,0}$ with $\alpha^{1,0} = 0$. If B_0 is the solution for $\alpha^{1,0} = 0$ and B_α is the solution for a non-zero $\alpha^{1,0}$, it is quite clear that $B_0 \neq B_\alpha$ and

$$B_0 \approx B_\alpha + \alpha^{1,0}B_\alpha^2 \tag{4.6}$$

to the first order ($E^{0,1}$, $E^{2,0}$, etc are also changed which would introduce higher order corrections to (4.6)). The non-dimensional magnitude of B_0 and B_α are $O(\epsilon)$, therefore, the difference $\alpha^{1,0}B_\alpha^2$ has a magnitude of only $O(\epsilon^2)$ unless $\alpha^{1,0}$ is large. Indeed, the expansion theory is valid only if $B\phi \gg B^2E^{1,0}$, which is not true if $\alpha^{1,0}$ is too large. Varying the other $\alpha^{i,j}$'s will also modify B in a similar way.

Theoretically, B could be found for any arbitrarily chosen $\alpha^{i,j}$ provided that the magnitude of the terms in (4.2) descends with order. This would involve solving an infinite series in B (and B_{xx}, etc) for B. However, for a fixed $z = z_1$, it appears that the $\alpha^{i,j}$ can be chosen to make $E^{i,j}(z_1) = 0$ so that B is obtainable from the first one or two terms of the expansion. To show this clearly, we plot $E^{1,0}$, $E^{0,1}$ and

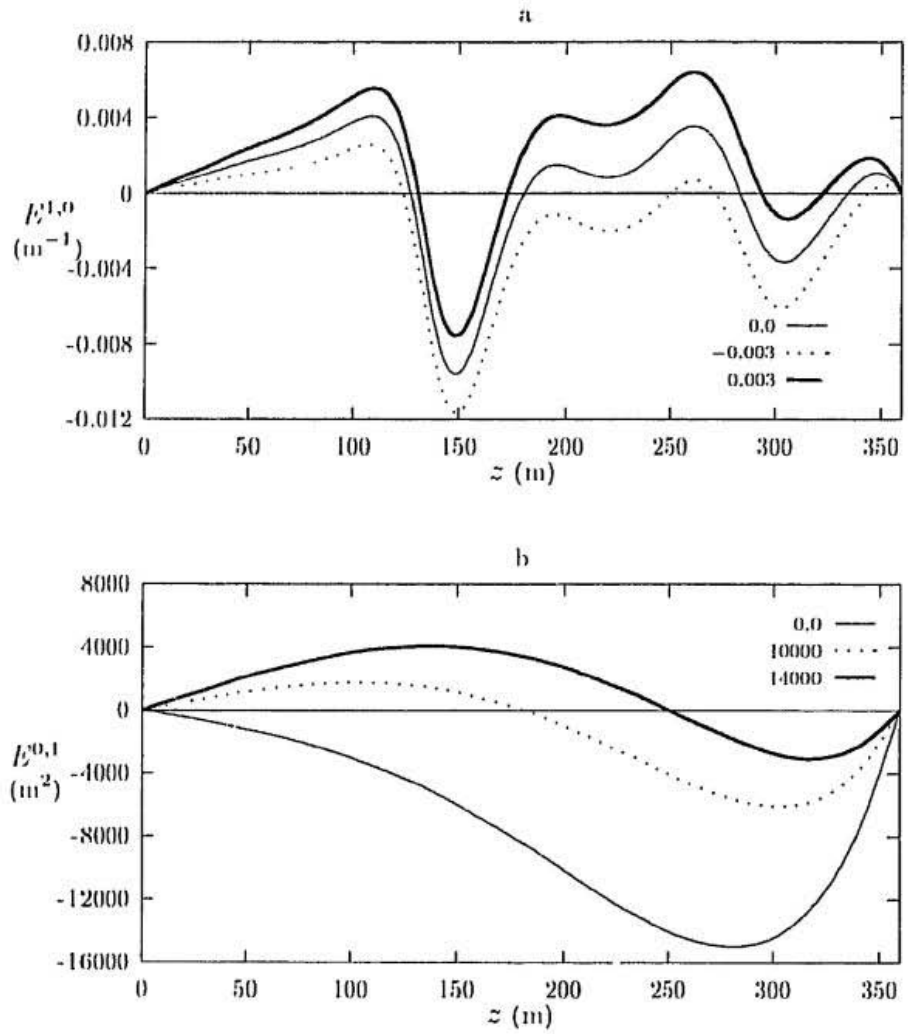

Figure 4.1: $E^{i,j}$ with $N_2^2(z)$ for different $\alpha^{i,j}$'s. (a). $E^{1,0}(z)$ for different values of $\alpha^{1,0}$. The $\alpha^{1,0}$ values are presented as the keys. (b). $E^{0,1}(z)$ for different values of $\alpha^{0,1}$ presented as the keys. $E^{0,1}$ is independent of $\alpha^{1,0}$. (c). $E^{2,0}(z)$ for different values of $\alpha^{2,0}$ presented as the keys, with $\alpha^{1,0} = -0.003$ fixed ($E^{2,0}$ depends on $\alpha^{1,0}$). Note that it is possible to let $E^{1,0}$,$E^{0,1}$ and $E^{2,0}$ have a common root.

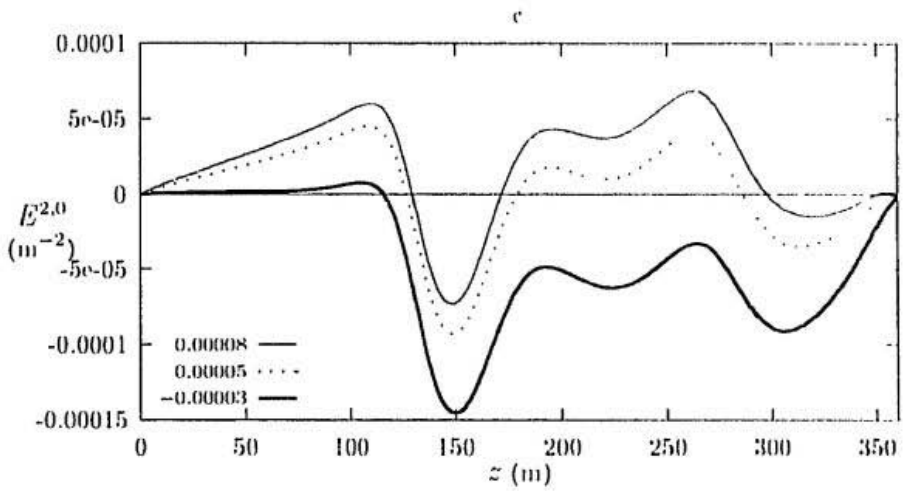

Figure 4.1: Continue.

$E^{2,0}$ with different $\alpha^{i,j}$ in figure 4.1, for the stratification $N_2^2(z)$ given by (2.39). It is seen that $E^{1,0}, E^{0,1}$ and $E^{2,0}$ have roots. Generally, the number of roots which $E^{1,0}$ and $E^{2,0}$ have depends upon the stratification $N^2(z)$ and $\alpha^{1,0}, \alpha^{2,0}$. $E^{0,1}$ has only one root. For a given $N^2(z)$, the roots vary as $\alpha^{1,0}, \alpha^{0,1}$ and $\alpha^{2,0}$ change (note that for certain $\alpha^{1,0}$ range $E^{1,0}$ may have no root at all). Thus, for a fixed $\alpha^{1,0}$, any depth, say z_1, could be a common root of $E^{0,1}$ and $E^{2,0}$ with properly selected $\alpha^{0,1}$ and $\alpha^{2,0}$ (z_1 could be a common root of $E^{1,0}$ as well). Similar discussion can be expected for higher order $E^{i,j}$ and $\alpha^{i,j}$. Therefore, at z_1, higher order terms in the expansion can

be made to vanish, and

$$\eta_d(t;\, x,\, z) = B\phi(z_1) + B^2 E^{1,0}(z_1) \tag{4.7}$$

(or $\eta_d = B\phi(z_1)$ if z_1 is also a root of $E^{1,0}$) defines the B profile for this particular $\alpha^{i,j}$ set. This procedure may be repeated at any other depth, say z_2, but the resulting B at z_2 will be different from that measured at z_1. This is because, although $\alpha^{1,0}$ is fixed, other $\alpha^{i,j}$ have to be adjusted to make z_2 a common root of $E^{i,j}$. These different $\alpha^{i,j}$ thus give a different B. In short, B profiles computed at any depth using (4.7) can be viewed as exact profiles for particular $\alpha^{i,j}$ sets.

From another point of view, if we keep $\alpha^{i,j}$ unchanged and assume that B_1 measured at some depth z_1 is the profile for this $\alpha^{i,j}$ set, B profiles approximated at other depths using the first two terms of (4.2) may then be regarded as approximations to B_1, since now the neglected higher order $E^{i,j}$ are non-zero.

Since our analysis is carried out up to the second order in ϵ, the resulting mKdV equation (4.3) depends only on $\alpha^{1,0}$ (λ is a function of $\alpha^{1,0}$), hence is an *approximate* evolution equation of the wave profile B. This approximation is independent of other $\alpha^{i,j}$. Because the evolution equation is an approximate one it is senseless to worry about obtaining B exactly. Thus no conclusion can be made concerning at which depth (or with which $\alpha^{i,j}$ set) a measured B should be best described by the theory.

The only restriction is that the $\alpha^{i,j}$s should not be too large (so that the asymptotic expansion holds). Naturally, differences between the theory and the model results are expected in comparison.

In (4.5) and (4.6), we have shown how different $\alpha^{1,0}$ define different B. An example of this is shoen in figure 4.2. B_0 and $B_{0.003}$ have been calculated at the same depth using (4.7) and plotted. Also plotted is $B_{0.003} + 0.003\,B_{0.003}^2$. Since the depth used is also a root of $E^{1,0}$ (for $\alpha^{1,0} = 0$), (4.6) is accurate up to at least the third order in ϵ. In the figure B_0 and $B_{0.003} + 0.003\,B_{0.003}^2$ are indistinguishable.

While different $\alpha^{1,0}$ extract different B, the wave propagation in the model results is of course independent of $\alpha^{1,0}$. Therefore, a good approximate theory should also be approximately independent of $\alpha^{1,0}$ in predicting the propagation. This will be tested later. Here, we just want to point out a crucial point about the theory in advance. The theory says that the total nonlinear propagation speed up to the second order (as in the mKdV equation) is $c_0(1 - rB - \lambda c_0 B^2)$, and both B and λ depend on $\alpha^{1,0}$. B and λ change with $\alpha^{1,0}$ in such a way that the net change in $c_0(1 - rB - \lambda c_0 B^2)$ is very small. On the other hand, the total nonlinear speed up to the first order (as in the KdV equation, obtained by setting $\lambda = 0$ in the mKdV equation) is $c_0(1 - rB)$, which is obviously sensitive to $\alpha^{1,0}$ since only B depends on $\alpha^{1,0}$. Therefore, it is anticipated that the mKdV theory may better describe the

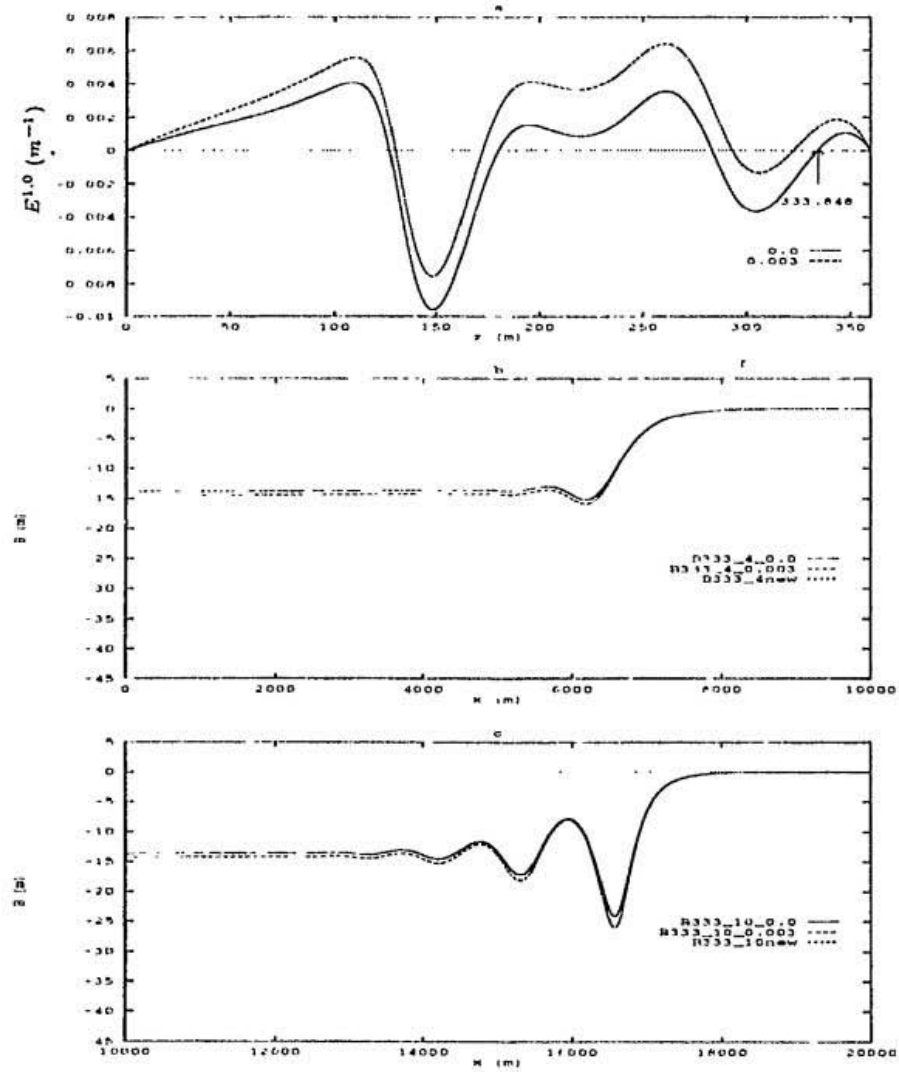

Figure 4.2: Comparison of B's measured at the same depth for different $\alpha^{1,0}$. $\bar{u} = 0.0m/s, c_0 = 0.965m/s$. (a). $E^{1,0}(z)$ with $N_2^2(z)$ for $\alpha^{1,0} = 0$ and $\alpha^{1,0} = 0.003$. (b). B_0, $B_{0.003}$ and $B_{new} = B_{0.003} + 0.003B_{0.003}^2$ at the same depth $z = 333.848m$ and output 4. Note that B_0 and B_{new} waves almost overlay each other. (c). Same as in (b), except for output 10.

evolution of wave B because it is potentially less sensitive to the change of $\alpha^{1,0}$. This will be shown to be the case.

4.1.2 Depth independence of the wave profile

It would be desirable to show that for fixed $\alpha^{i,j}$, the asymptotic expansions (4.5) and (4.6) are valid by showing that the same B is obtained for each z when the infinite series (4.6) is solved. Unfortunately, there is no way to solve this infinite series. The discussion in the previous section suggests that at least we can approximate B by using the first two terms.

The first two terms are a good approximation to the whole expansion only if the associated truncation error is small, i.e.

$$B\phi + B^2 E^{1,0} \gg B_{xx} E^{0,1} + B^3 E^{2,0} + \cdots \tag{4.8}$$

is true. Actually, the terms in ϵ are descending, i.e. $B\phi \gg B^2 E^{1,0} \gg B^3 E^{2,0}$. But $B^2 E^{1,0} \gg B_{xx} E^{0,1}$ is true only if $\epsilon \gg \mu$, as for long waves. When waves are extremely short (e.g. a steep front or undular bore, etc) it is possible for $B_{xx} E^{0,1}$ to be larger than $B^2 E^{1,0}$. Thus the approximation is valid for all z only for waves which are sufficiently long.

Assuming that (4.8) is true for our waves so that the first two terms in (4.2) is

a good approximation to the full expansion, we have

$$B^2 E^{1,0} + B\phi - \eta_d = 0, \tag{4.9}$$

which gives solutions

$$B_{1,2} = \frac{-\phi \pm \sqrt{\phi^2 + 4\,\eta_d\,E^{1,0}}}{2\,E^{1,0}}. \tag{4.10}$$

Of the two roots, only B_1 (with the positive sign) is acceptable. By using $\sqrt{1+x} = 1 + x/2 + x^2/4 + \cdots$, the roots are

$$B_1 \approx \frac{\eta_d}{\phi} - \frac{2\eta^2 E^{1,0}}{\phi^3} + \cdots \tag{4.11}$$

$$B_2 \approx -\frac{\phi}{E^{1,0}} - \frac{\eta_d}{\phi} + \frac{2\eta^2 E^{1,0}}{\phi^3} + \cdots \tag{4.12}$$

Obviously, when $E^{1,0} \to 0$, B_2 goes to infinity, while B_1 recovers the solution $B = \eta_d/\phi$ of (4.9). Thus we select B given by

$$B = \frac{-\phi + \sqrt{\phi^2 + 4\,\eta_d\,E^{1,0}}}{2\,E^{1,0}}. \tag{4.13}$$

Equation (4.13) includes the undetermined $\alpha^{1,0}$. For real B, $\alpha^{1,0}$ must satisfy

$$\alpha^{1,0} \left(\begin{array}{c} \leq \\ \geq \end{array} \right) - \frac{\phi}{4\eta_d} - \frac{\phi^{1,0*}}{\phi} - \frac{r}{c_0} + \frac{(N^2)_z\,\phi}{2c_0 N^2} \quad \text{for} \quad \eta_d \left(\begin{array}{c} \leq \\ \geq \end{array} \right) 0 \tag{4.14}$$

through the entire depth. This is valid only if η_d has the same sign throughout the entire depth, which is guaranteed since we are considering mode one waves (Note that

for higher mode waves, both η_d and ϕ would change sign). In our case, $\eta_d \leq 0$ so we take the upper case.

Condition (4.14) depends on $\eta_d(t; x, z)$ which is variable for different flows. Even for the same flow, because of its time-space variation, one $\alpha^{1,0}$ which works for early outputs may not work for later outputs. Therefore, it is desirable to find a critical $\alpha_c^{1,0}$ which is independent of $\eta_d(t; x, z)$ so that any $\alpha^{1,0} \leq \alpha_c^{1,0}$ ensures real B. $\alpha_c^{1,0}$ is determined by

$$\max E^{1,0}(z; \alpha_c^{1,0}) = 0, \tag{4.15}$$

thus the condition for $\alpha^{1,0}$ is

$$\alpha^{1,0} \leq \alpha_c^{1,0}. \tag{4.16}$$

Obviously, such a $\alpha^{1,0}$ ensures the solvability of real B. Note that (4.15) and (4.14) are only valid for non-zero $N^2(z)$. If $N^2(z)$ goes to 0 below some depth z_c we will require that they hold in a region where $N^2(z) > \delta$ for some small δ since $\frac{(N^2)_z}{N^2}$ becomes infinite in general. Although $\frac{(N^2)_z}{N^2}$ remains finite for the case considered here computational problems arise when $N^2(z)$ is too small.

Condition (4.16) may be too strong for individual flows with small $|\eta_d(t; x, z)|$, i.e., it may not be necessary to require $\alpha^{1,0} \leq \alpha_c^{1,0}$ in order to obtain B. In some of the examples given later, for convenience, $\alpha^{1,0}$ is not restricted to this condition.

It should be also noted that not all $\alpha^{1,0} \leq \alpha_c^{1,0}$ are usable. If $\alpha^{1,0}$ goes to $-\infty$, the asymptotic expansion would be no longer valid since higher order terms would become large. It is impossible to find a lower limit for $\alpha^{1,0}$ because of the inherent arbitrariness of the expansion process. Thus, it is safe to choose a value of $\alpha^{1,0}$ which satisfies condition (4.16) and has small magnitude. Tests with different $\alpha^{1,0}$ will be given later in section 4.3.1.

In order to show that the approximate B obtained using (4.13) is approximately independent of the value of z used in (4.13), we set $\alpha^{1,0}$ to $\alpha_c^{1,0}$ which is -0.00774 for the smooth $N_1^2(z)$, and plot in figure 4.3 B's obtained at different depths (see also figure 4.9, figure 4.12, figure 4.15, figure 4.18 and figure 4.20, etc.) within the stratified upper layer, before and after the undular bore appears. The magnitude of the discrepancy between B's obtained using (4.13) at different depths depends on the associated truncation error. When the truncation error goes to zero, these B's should converge to the exact B profile, and vice versa. It seems that even at the undular bore stage the truncation error is small, i.e. $B^2 E^{1,0} \gg B_{xx} E^{0,1}$. It can be seen that B is roughly independent of z, especially at the wave front. The discrepancy there is due to the truncation error. At the wave tail, the Bs from different depths are different. This is either because the wave tail is over the bank edge (around $x \leq 0$) where the depth is non-uniform and the analysis does not apply, or because waves of

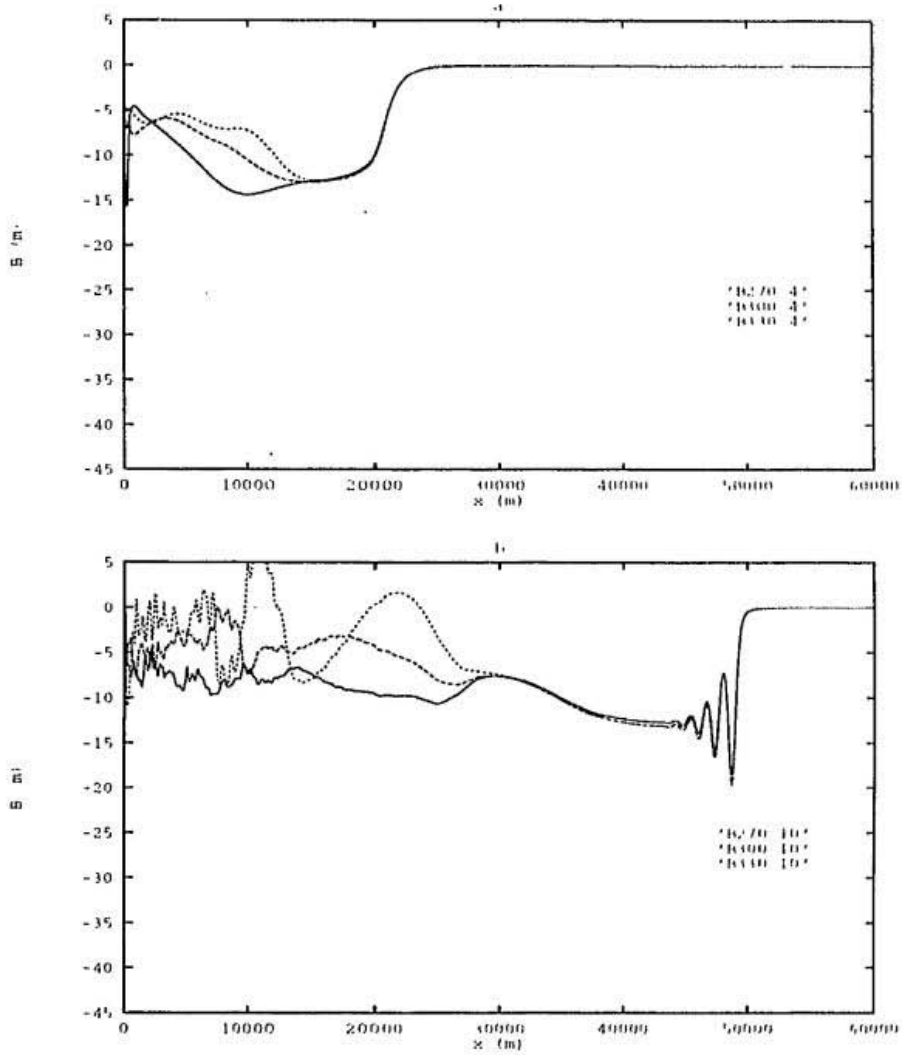

Figure 4.3: Depth independence of B profile with the smooth $N_1^2(z)$, $\alpha_r^{1,0} = -0.00774$. (a). B's at $270m, 300m, 330m$ at output 4. (b). Same as in (a) except at output 10.

other modes are present. Since the other modes propagate more slowly than the first mode, the contamination at the tail has no effect on the evolution of the wave front.

Now we would like to summarize what we did in the above. We first suggested that for a fixed $\alpha^{1,0}$, B calculated at any depth using the first two terms of the expansion may be regarded as an exact wave profile for a particular $\alpha^{i,j}$ set or, as an approximation to the wave profile at other depths. However, because the mKdV equation is only an approximate evolution equation for B, it is not critical to have an exact B. Next, a condition was found for $\alpha^{1,0}$ which ensures the solvability of real Bs from (4.13). Finally, we showed that B is approximately depth independent for a fixed $\alpha^{i,j}$ set.

The wave profile B is measured from the output of IGWsim by a C-code PERT. After $B(t_i, x)$ is obtained at each output time (i = is the output number), we choose a smooth $B(t_k, x)$ at some initial stage as an initial condition $B_{initial}(t, x)$ and solve the time dependent KdV/mKdV equation (4.3) for the theoretical $B_{theory}(t_i, x)$. Then a comparison is made between B and B_{theory}, both of which have evolved from the same initial $B_{initial}$.

The sketch in figure 4.4 is a brief overview showing the procedures used and their relations. C-codes EIG, KDV, PERT and COMP are integrated as a whole thus form an analysis model which is referred to as IGWana (Internal Gravity Wave

Analysis) hereafter. IGWana takes the domain and background parameters from the startup file of IGWsim and calculates the vertical modes up to the second order in ϵ and the associated nonlinear/dispersive coefficients. B profiles are measured at selected depths from IGWsim density field outputs and an initial wave is chosen. Then, theoretical KdV/mKdV waves evolving from the initial wave are computed. Finally, detailed comparison is made by COMP.

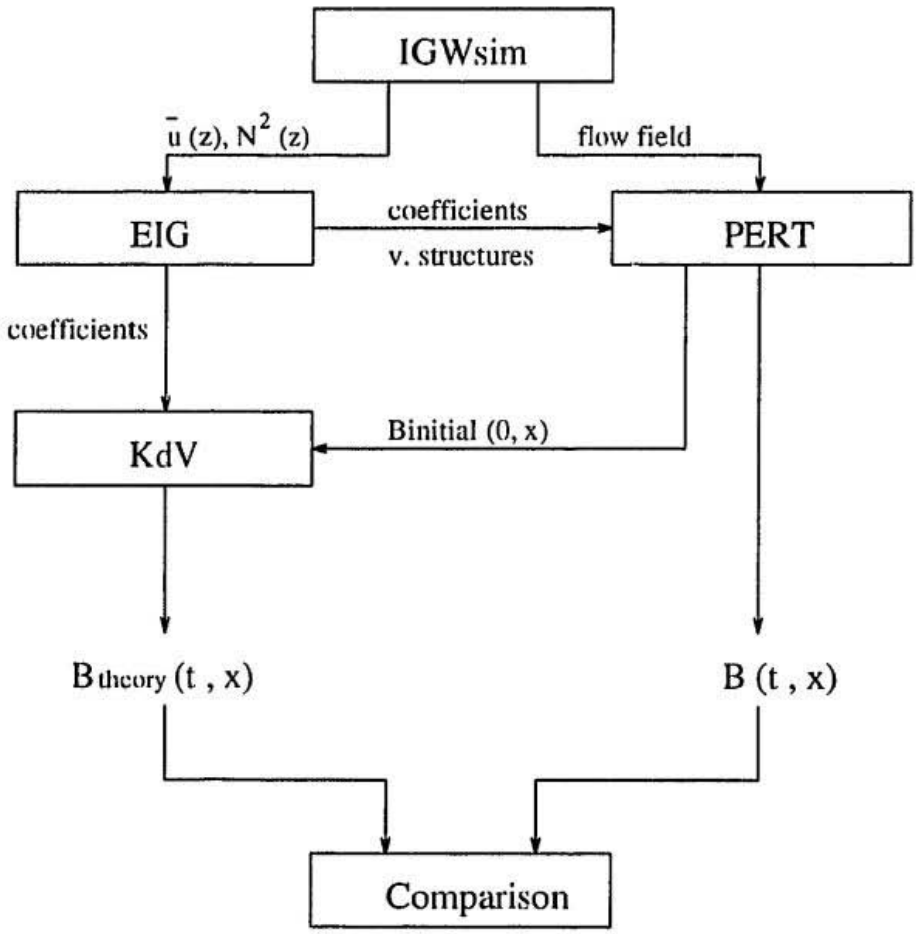

Figure 4.4: The sketch of IGWana model working flow.

4.2 Resolution test

We first run the model for different space/time resolutions to see how sensitive the model results are to the resolution. An effective resolution will be selected based on these runs.

The resolution of the model can be written as $(\Delta x, \Delta z, dt)$. In our runs, $\Delta x = L/I$ is uniform and

$$\Delta z = (H - h(x)) \frac{A}{1 + a\frac{j}{J}\Delta\eta} \Delta\eta \tag{4.17}$$

is variable (recall $\Delta\eta = 1.0$). j is the index of vertical grid. This vertical coordinate transformation gives a higher resolution in the upper stratified layer. Recall that the model is based upon the projection method described in chapter 2. The projection matrix is a $[I(J-1)]\times[I(J-1)]$ matrix. Projecting a given flow field to a divergent-free vector field involves $O(IJ^2)$ operations, and this is the main part of the calculation at each time step. Memory requirements are $O(IJ^2)$ for the LU decomposition of the block tridiagonal projection matrix. When I and J are large it could take too long to run the model for fixed dt and T. Note that doubling J will increase the calculating operation by a factor of four if dt is unchanged and quadruple memory requirements for the projection matrix. Thus the computational expense is very sensitive to J. Theoretically, the higher the resolution (i.e., the smaller $\Delta x, \Delta z$ and dt), the better

the numerical results. We would like to choose a resolution which is high enough for our problem, and at the same time, does not take too long to finish a $T = 16000$s run. Some results for different resolutions are given below in figures 4.5-4.7. The density stratification used for these test runs is the stepwise $N_1^2(z)$ given by (2.38), the scaled amplitude of the generated waves is about $\epsilon = 0.04$ (corresponding to that of the moderate forcing case) and the terminal background flow is $\bar{u} = 0.194$ m/s.

It is found that the model is fairly insensitive to Δz resolution when $J \geq 40$, except a small phase shifting (figure 4.5). This is good news since we do not have to take a large J which would significantly increase the amount of calculation. The model is more sensitive to Δx resolution (figure 4.6), and with a low resolution the model certainly can not capture most of the wave features. However, when $\Delta x \leq 40m$ (or $I \geq 2000$), this sensitivity decreases a great deal. It is also noted that the initial waves at output 4 are slightly different for both Δz and Δx tests. Some of the difference at output 10 could be a result of this initial difference, although figure 4.5 (a) and figure 4.6 (a) suggest that this effect is small. As for dt, all runs had the same time step $dt = 2.5$s until output 4 so that the initial state for the tests is exactly the same (figure 4.7). The time step for the run with $dt = 8$s actually varies around 8s because 8s is near the time step restriction (2.35). The actual time steps for other runs are as indicated by the attached labels. As can be seen, although the model is

subject to the variation of dt, the results convergence quickly in the limit $dt \to 0$.

Based on the above tests, a resolution corresponding to ($I = 2048, J = 40, dt = 2.5$) has been selected for all the following runs. The above test runs suggest that at this resolution the amplitudes of the waves in the undular bore are quite accurate. This implies that any differences in amplitude seen between the model results and the KdV/mKdV solutions later on are due to the approximations made in the weakly nonlinear theories and not to numerical dissipation. With this resolution, the model results are near what would be obtained when $I, J \to \infty$ and $dt \to 0$.

Resolution tests were also done for larger waves with $\epsilon \sim 0.07$ (corresponding to the strong forcing case). Similar results were obtained but are not shown here, which indicate that the above conclusion is still true for waves with $\epsilon \sim 0.07$.

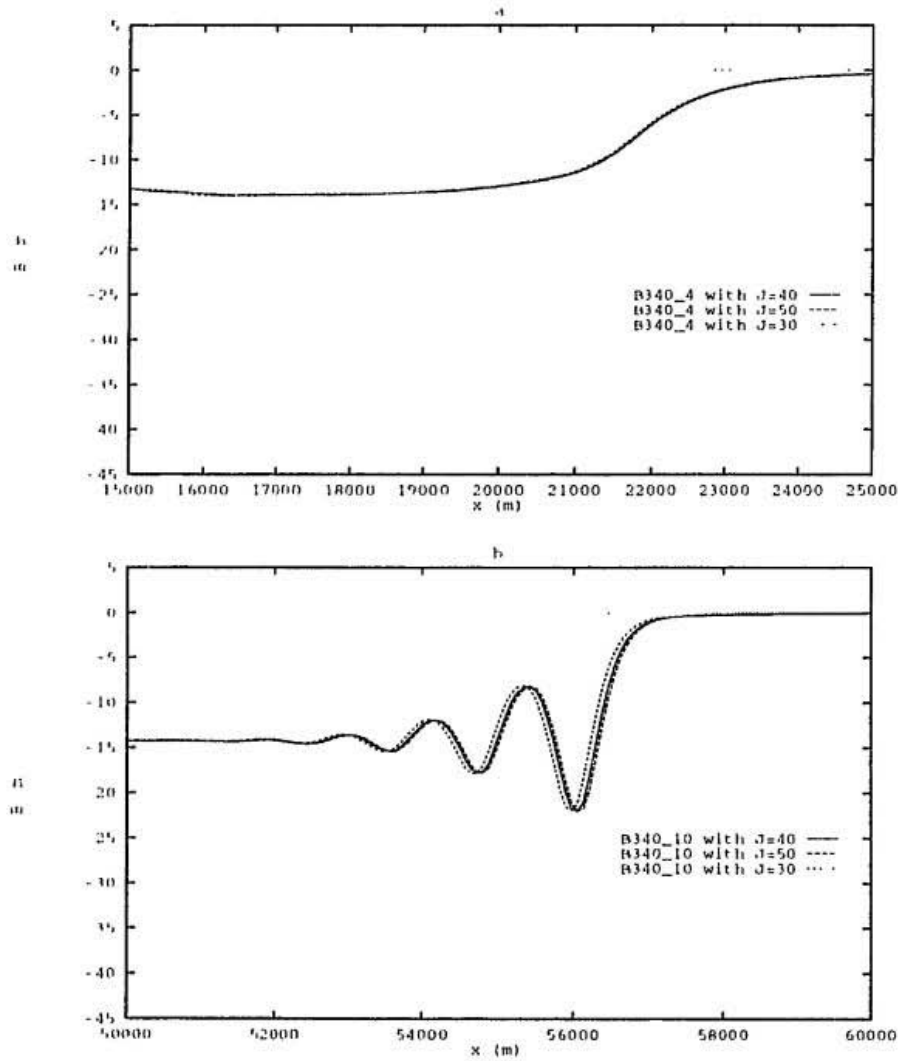

Figure 4.5: Comparison between model results for different J while I is fixed to 1024 and dt is fixed to 2.5. The stratification is the stepwise $N_1^2(z)$, and $\alpha^{1,0} = -0.005$. $u = 0.833m/s, c_0 = 2.508m/s$. The compared waves are measured at $z = 340m$. (a). B's at output 4. (b). B's at output 10.

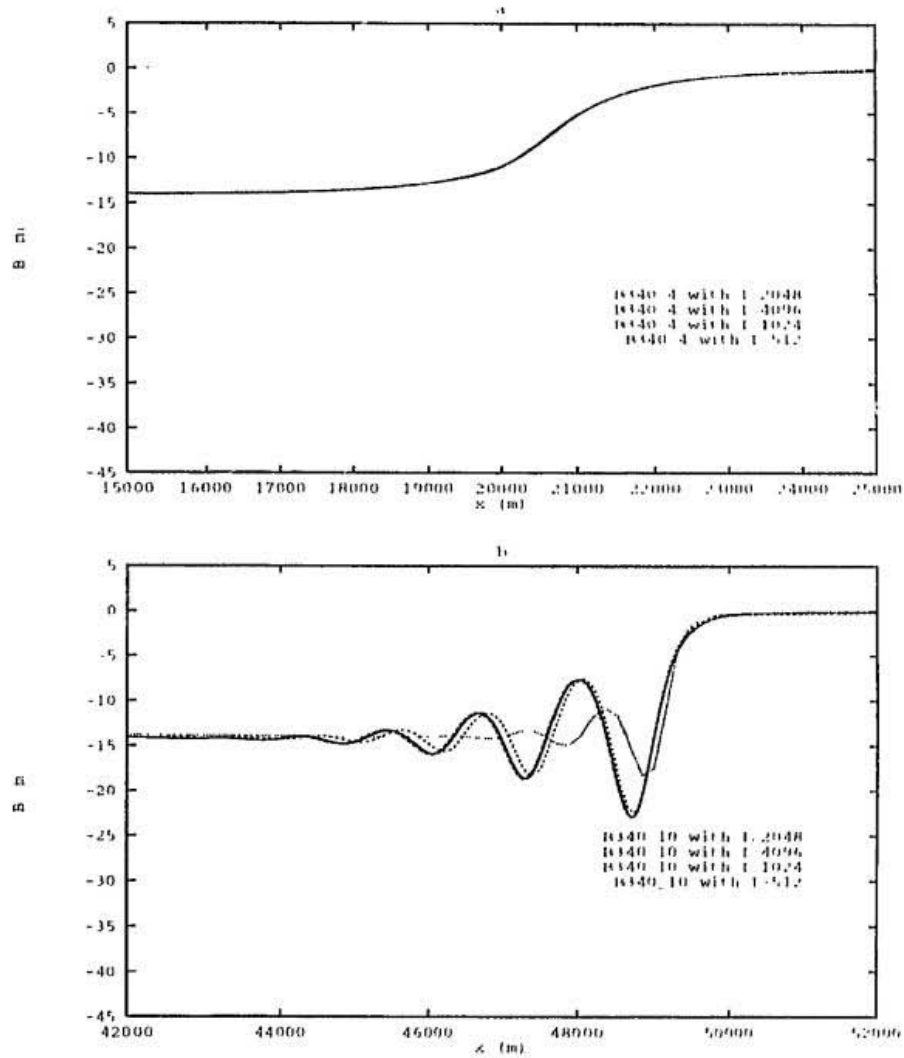

Figure 4.6: Comparison between model results for different I while J is fixed to 40 and dt is fixed to 2.5. The stratification is the stepwise $N_1^2(z)$, and $\alpha^{1,0} = -0.005$. $\bar{u} = 0.833m/s, c_0 = 2.508m/s$. The compared waves are measured at $z = 340m$. (a). B's at output 4. (b). B's at output 10.

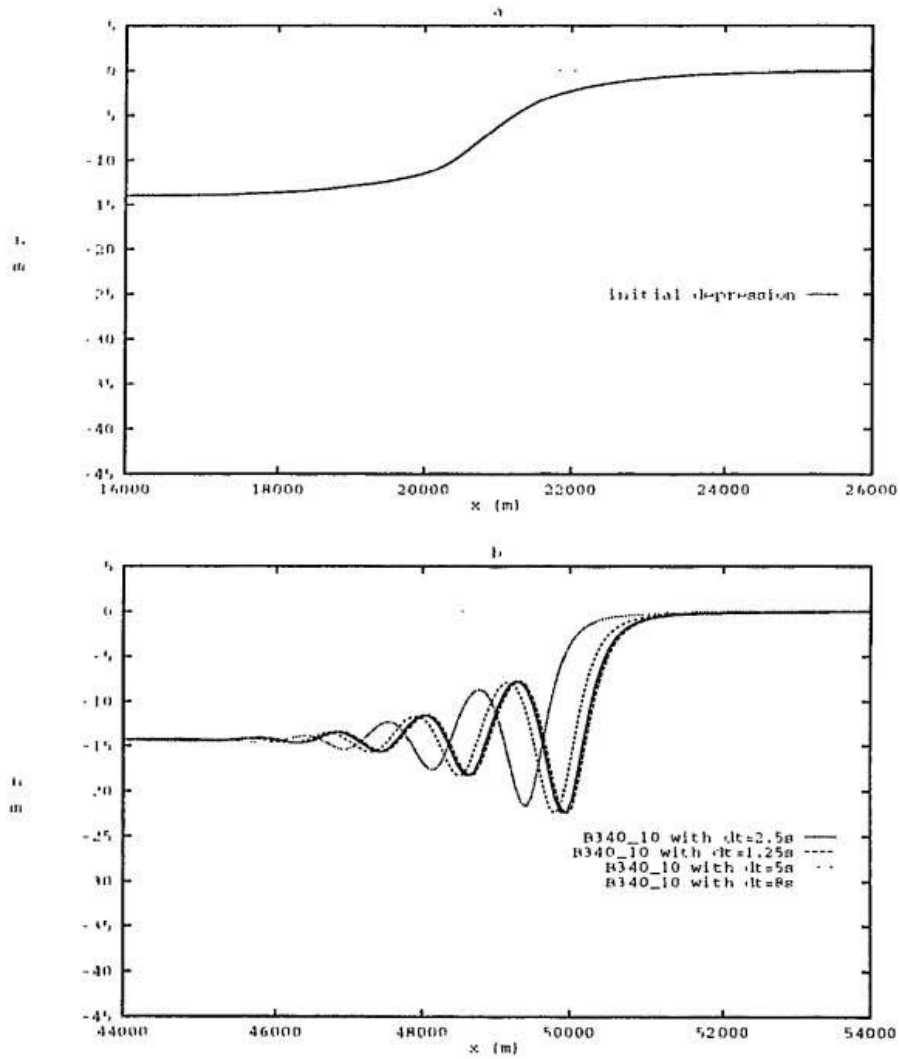

Figure 4.7: Comparison between model results for different dt while I is fixed to 1024 and J is fixed to 40. The stratification is the stepwise $N_1^2(z)$, and $\alpha^{1,0} = -0.005$. $\bar{u} = 0.833m/s, c_0 = 2.508m/s$. The compared waves are measured at $z = 340m$. Each model run uses the same time step $dt = 2.5s$ until output 4. (a). The initial depression at output 4. (b). B's at output 10.

4.3 Results and discussion

Now we are ready to compare the weakly nonlinear theory with the model results. This will be done for three categories of tests. The first two are for different stratifications and wave amplitudes. For the third, two runs were done to test rotational effects and to determine the validity of the theory in a rotating system. In the following $B(t,x)$ represents the density perturbation wave measured from IGWsim while $B_{kdv}(t,x)$ and $B_{mkdv}(t,x)$ denote the theoretical wave given by the KdV and mKdV equations. In order to see how different the nonlinear theory is from the linear theory, linear waves evolving from the same initial conditions are also included in the comparison and are represented by $B_{ln}(t,x)$.

The two stratifications $N_1^2(z)$ and $N_2^2(z)$ given in chapter 2 have been used for detailed comparisons of the model and theoretical results. With $N_1^2(z)$, two values of q are considered (see figure 2.4). For each $N^2(z)$, the model is initialized with different forcings, i.e. weak forcing, moderate forcing and strong forcing, for the purpose of testing the dependence of validity range of the theory on the largeness of the waves. The amplitudes of waves for the three forcings are approximately 7 m, 14 m and 25 m, respectively. The scaled amplitude for the forcings are therefore $\epsilon \approx 0.02, 0.04$ and 0.07. Finally, the model is run with rotation included and the result is compared with

$N^2(z)$, f	$\alpha_*^{1,0}$ $m^{-2}s$	c_0 ms^{-1}	τ m^{-1}	s m^3s^{-1}	$\alpha^{1,0}$ $m^{-2}s$	λ $m^{-3}s$	*terminal* $\tilde{u}$ (ms^{-1})		
							wf	*mf*	*sf*
$N_2^2(z)$, f=0	−0.00867	0.965	0.00807	−4570	−0.00867	-1.657×10^{-4}	0	0	0
					−0.02867	-4.884×10^{-4}	*NR*	0	*NR*
					−2.00867	-3.243×10^{-2}	*NR*	0	*NR*
smooth $N_1^2(z)$, f=0	−0.00774	2.5	0.00833	−10003	−0.00774	-2.982×10^{-5}	0.194	0.194	0.078
stepwise $N_1^2(z)$, f=0	−0.00796	2.507	0.00837	−9798	−0.00796	-2.907×10^{-5}	*NR*	0.194	*NR*
$N_2^2(z)$, $f=10^{-4}$	−0.00867	0.965	0.00807	−4570	−0.00867	-1.657×10^{-4}	*NR*	*NR*	0

Table 4.1: The list of runs, the associated parameters and coefficients. Notations wf, mf, sf stand for weak forcing, moderate forcing and strong forcing, respectively. NR means no run for that case. For $N_2^2(z)$, the initial depression is specified for each forcing, thus no need to use a background flow.

the non-rotating case. Rotation makes long waves dispersive, so it is expected that rotation will affect the evolution of long waves. The importance of rotation should be greatly reduced at the wave front after it gets sufficiently steep and develops an undular bore, since then short length scales are involved. It is interesting to know if our non-rotating theory is applicable to a rotating flow at such a stage. Therefore, the theory is also compared with the rotating result.

Table 4.1 is the list of all runs and the associated parameters and coefficients. The following are the results of comparisons for each group of runs.

4.3.1 Runs with $N_2^2(z)$

For this stratification, as mentioned in section 2.3, strong overturning at the bank edge made it difficult to generate a satisfactory initial depression which would develop into an undular bore within the 16000s evolution time. Therefore, the model is initialized with a smooth mode-one linear wave using the first order perturbation. In this case no background flow is needed and $\bar{u}$ is set to zero (These runs were in fact the last done, otherwise all model runs would have been done this way).

In this group of runs, extra experiments are done with the moderate forcing case for different values of $\alpha^{1,0}$. The purposes of these runs are, first, to verify that the mKdV result is less sensitive to $\alpha^{1,0}$ than the KdV result and hence better describes the evolution of waves. Second, we want to see what will happen when $|\alpha^{1,0}|$ is large. Therefore, $\alpha^{1,0}$ is set to $\alpha_c^{1,0}$, $\alpha_c^{1,0} - 0.02$ and $\alpha_c^{1,0} - 2.0$, respectively, and comparisons are made at the three depths. Figure 4.8 shows $E^{1,0}(z)$ for the three $\alpha^{1,0}$. Figures 4.9-4.11, 4.12-4.14 and 4.15-4.17 show the approximate depth independence of B profiles and the comparisons of the model results with the theoretical results at the depths of 330 m, 300 m and 270 m for the three different $\alpha^{1,0}$ values.

It is seen in figure 4.9 and 4.12 that B profiles measured at depths above 180 m are quite depth independent, the small discrepency is only due to the truncation

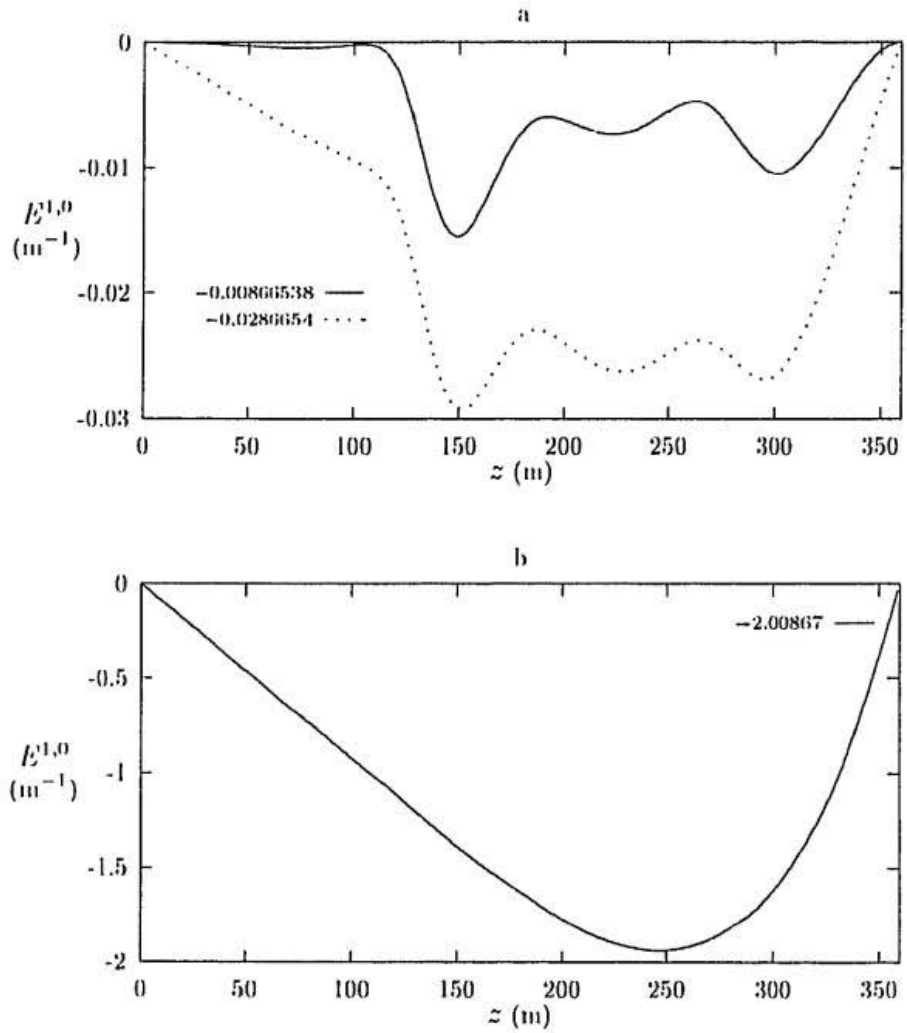

Figure 4.8: $E^{1,0}(z)$ with $N_2^2(z)$ for different $\alpha^{1,0}$. (a). $\alpha^{1,0} = -0.00866538$ and -0.0286654. (b). $\alpha^{1,0} = -2.00867$.

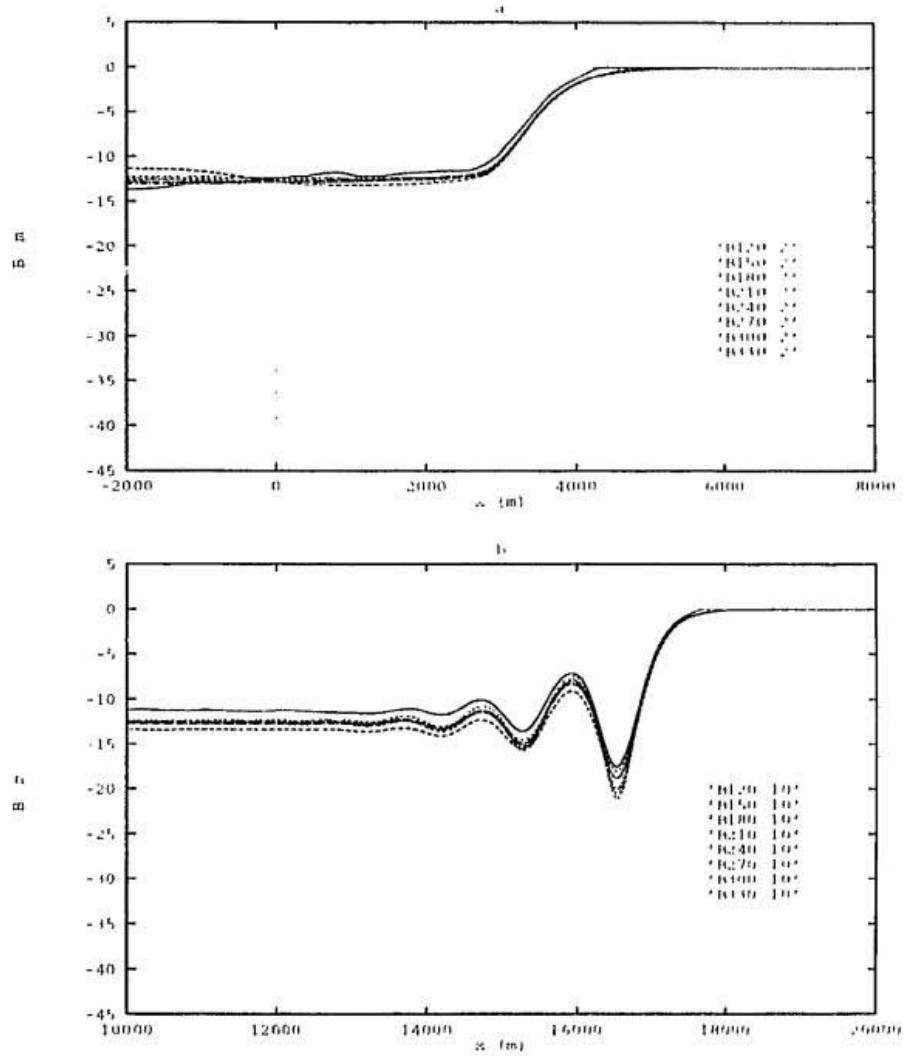

Figure 4.9: B's measured at different depths for the run with $N_2^2(z)$ and moderate forcing. $\alpha^{1,0} = -0.00867, \bar{u} = 0.0m/s$, $c_0 = 0.965m/s$ and $\lambda = -1.657 \times 10^{-5}$. (a). B's at $z = 120m$ to $z = 330m$ with an interval of $30m$ and at output 2. (b). Same as in (a) except at output 10.

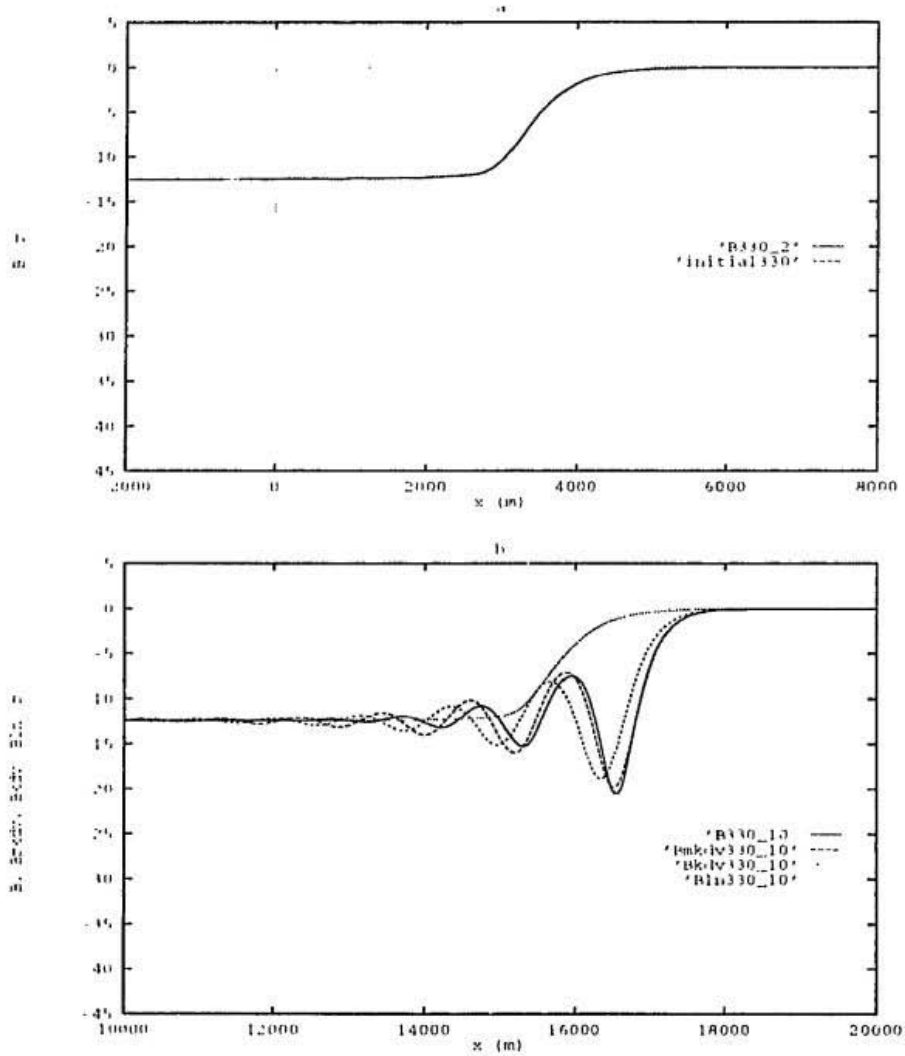

Figure 4.10: Comparison between the model and the analysis for the run with $N_2^2(z)$ and moderate forcing. $\alpha^{1,0}, \bar{u}, c_0$ and λ are the same as for Figure 4.9. (a). Original and reconstructed initial wave at $z = 330m$. (b). Comparison of B_{ln}, B_{kdv} and B_{mkdv} with B at $z = 330m$ and at output 10.

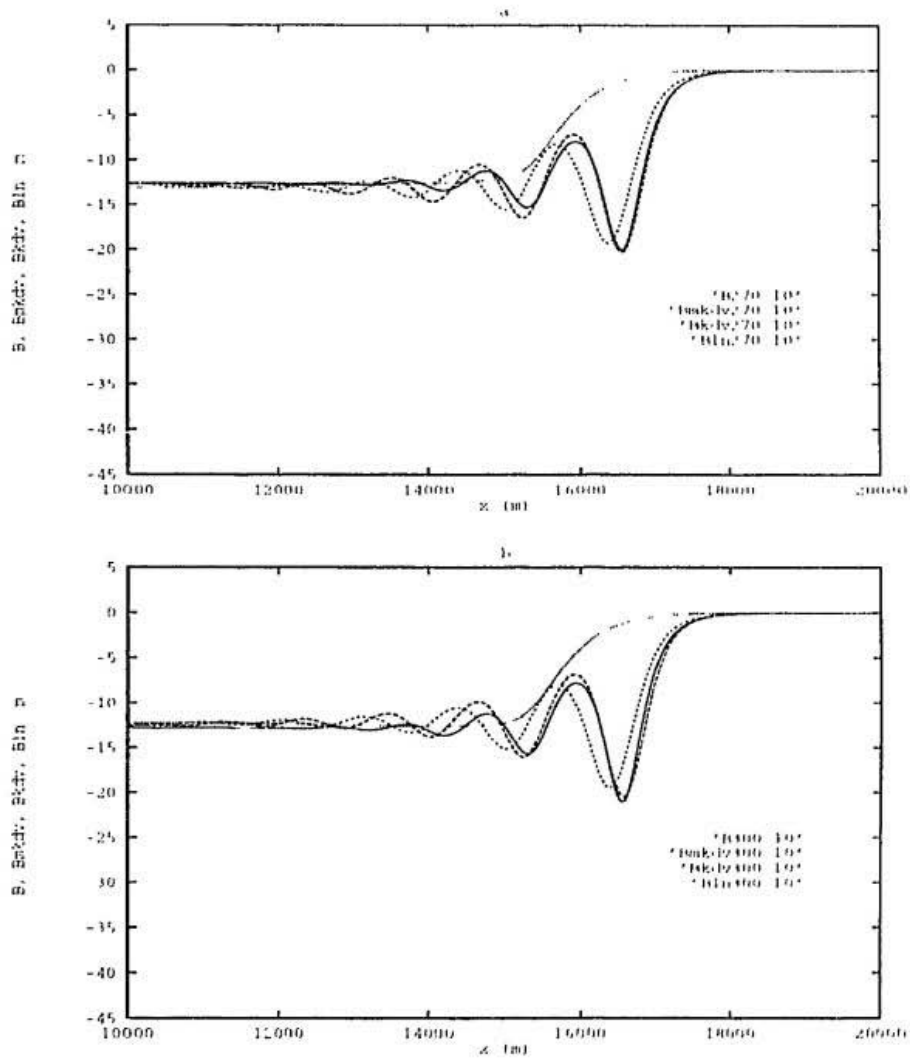

Figure 4.11: As in 4.10 (a). but for (a). $z = 270\,\mathrm{m}$. (b). $z = 300\,\mathrm{m}$.

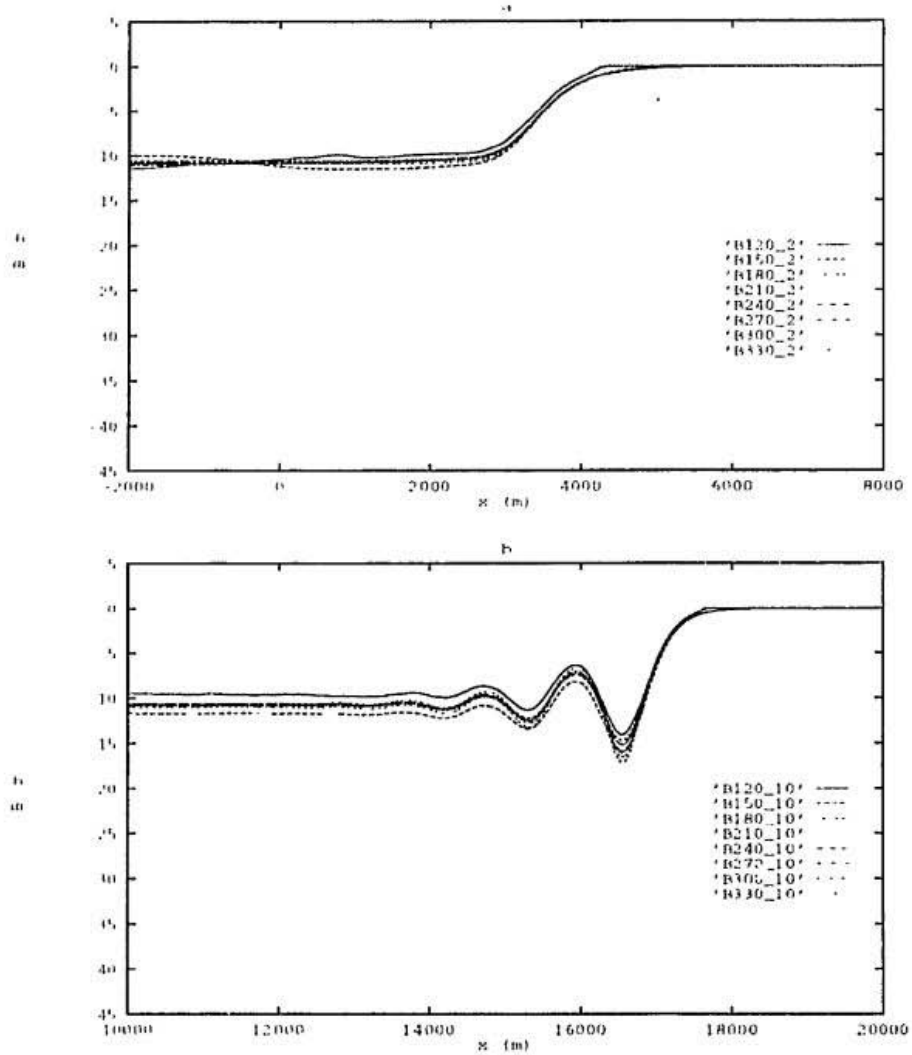

Figure 1.12: B's measured at different depths for the run with $N_2^2(z)$ and moderate forcing. $\alpha^{1,0} = -0.02867, u = 0.0m/s$, $c_0 = 0.965m/s$ and $\lambda = -4.884 \times 10^{-5}$. (a). B's at $z = 120m$ to $z = 330m$ with an interval of $30m$ and at output 2. (b). Same as in (a) except at output 10.

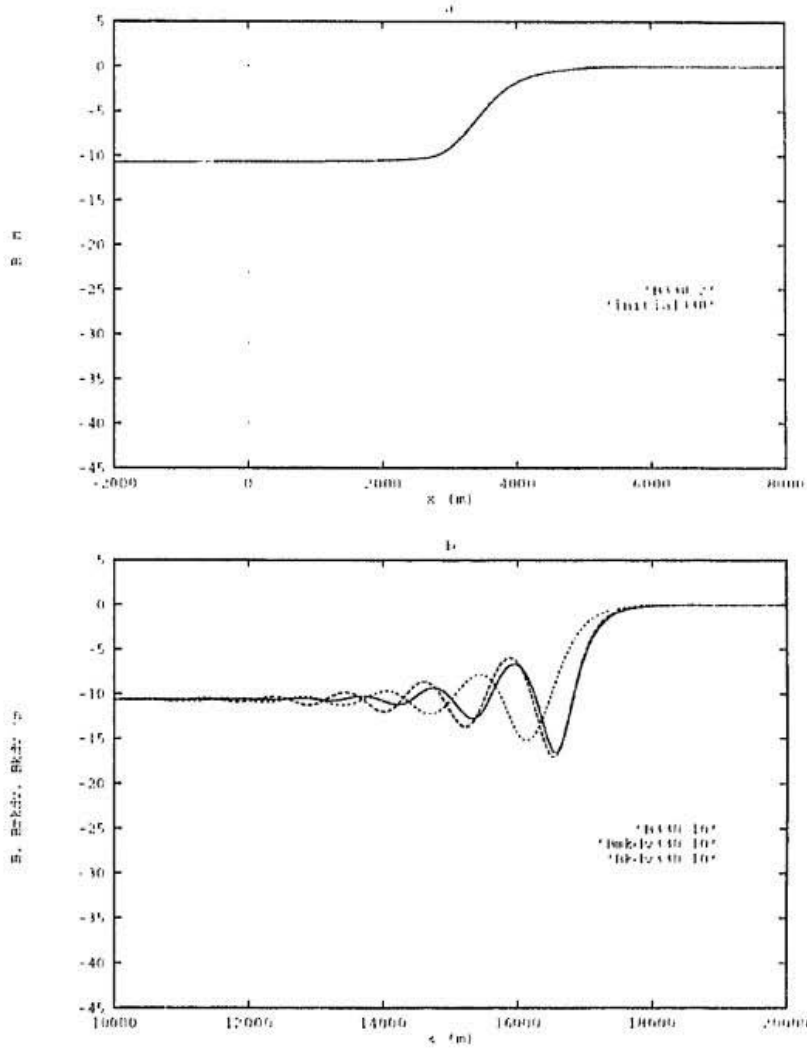

Figure 4.13: Comparison between the model and the analysis for the run with $N_z^2(z)$ and moderate forcing. $\alpha^{1,0}, \bar{u}, c_0$ and λ are the same as for Figure 4.12. (a). Original and reconstructed initial wave at $z = 330m$. (b). Comparison of B_{kdv} and B_{mkdv} with B at $z = 330m$ and at output 10.

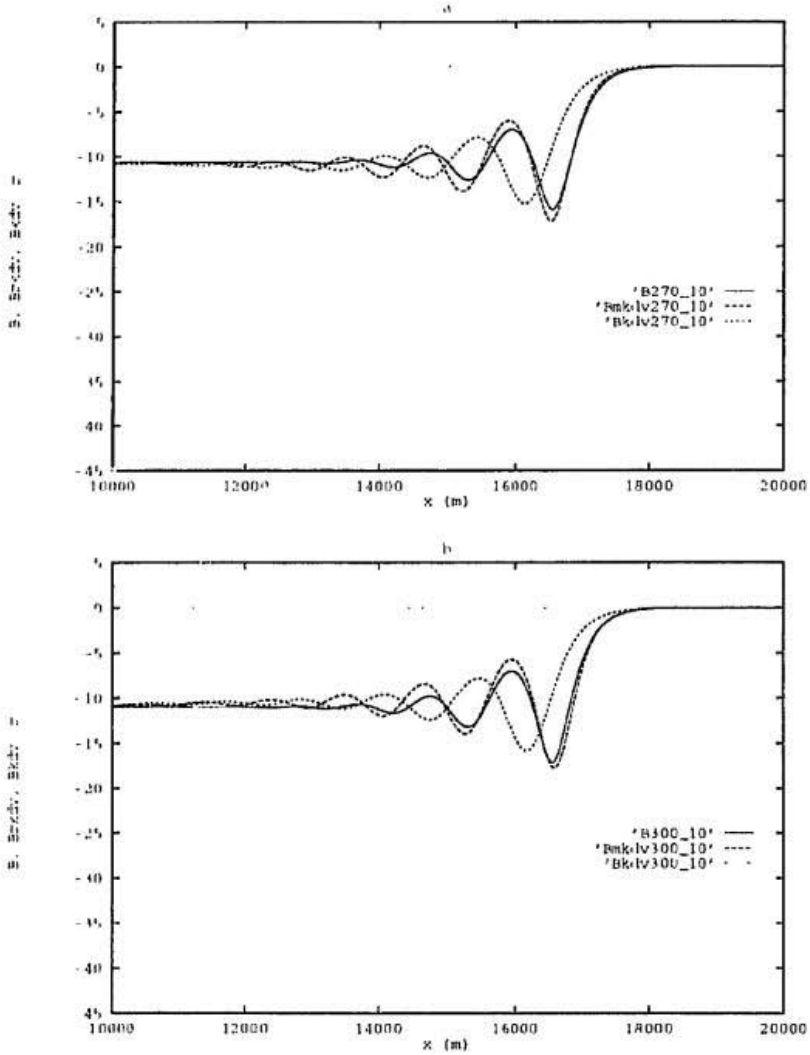

Figure 4.14: As in 4.13 (a). but for (a). $z = 270\,\mathrm{m}$. (b). $z = 300\,\mathrm{m}$.

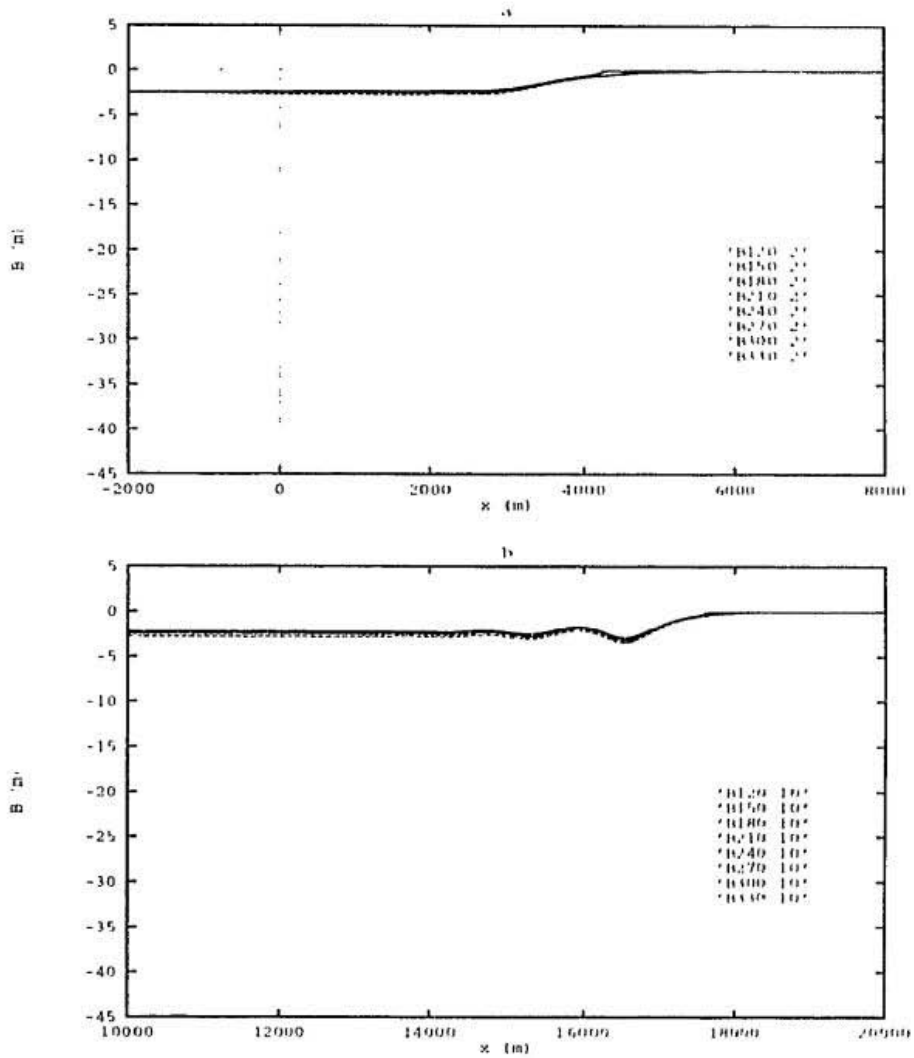

Figure 4.15: B's measured at different depths for the run with $N_2^2(z)$ and moderate forcing. (a). B's at $z = 120m$ to $z = 330m$ with an interval of $30m$ and at output 2. (b). Same as in (a) except at output 10.

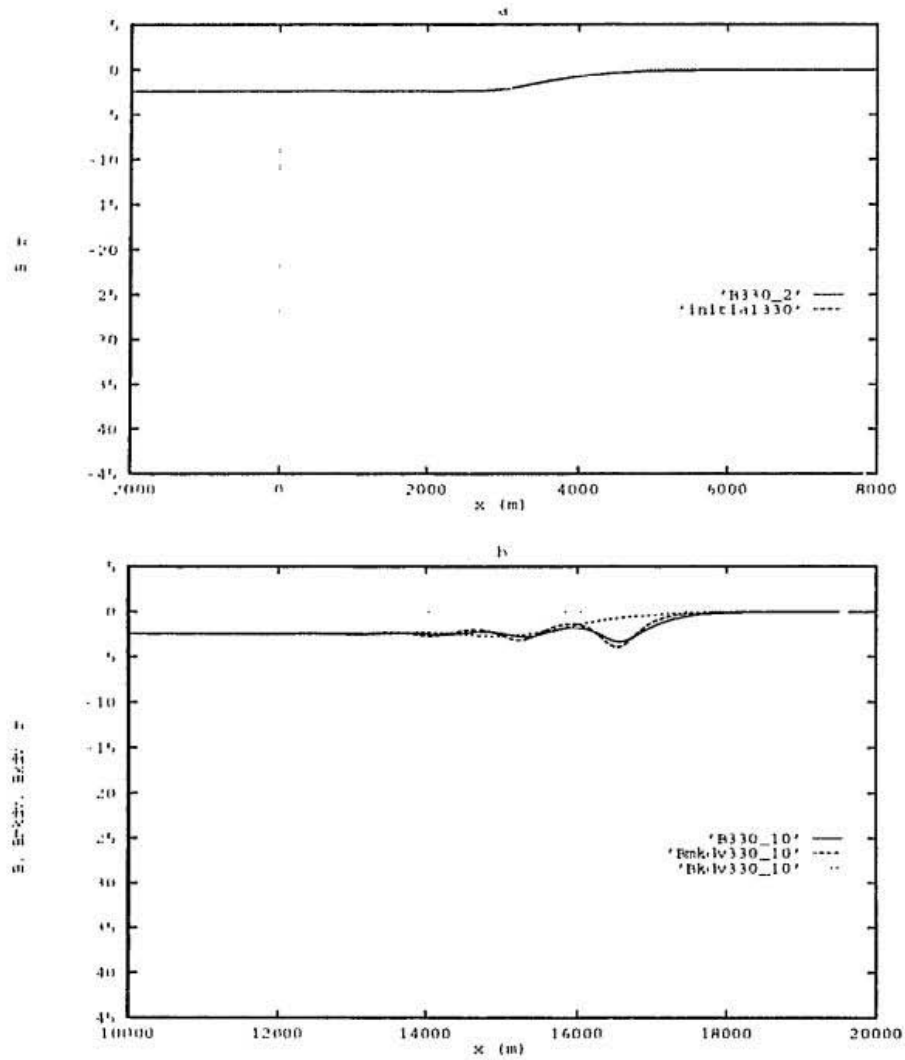

Figure 4.16: Comparison between the model and the analysis for the run with $N_2^2(z)$ and moderate forcing. $\alpha^{1,0}, \tilde{u}, c_0$ and λ are the same as for Figure 4.15. (a). Original and reconstructed initial wave at $z = 330m$. (b). Comparison of B_{kdv} and B_{mkdv} with B at $z = 330m$ and at output 10.

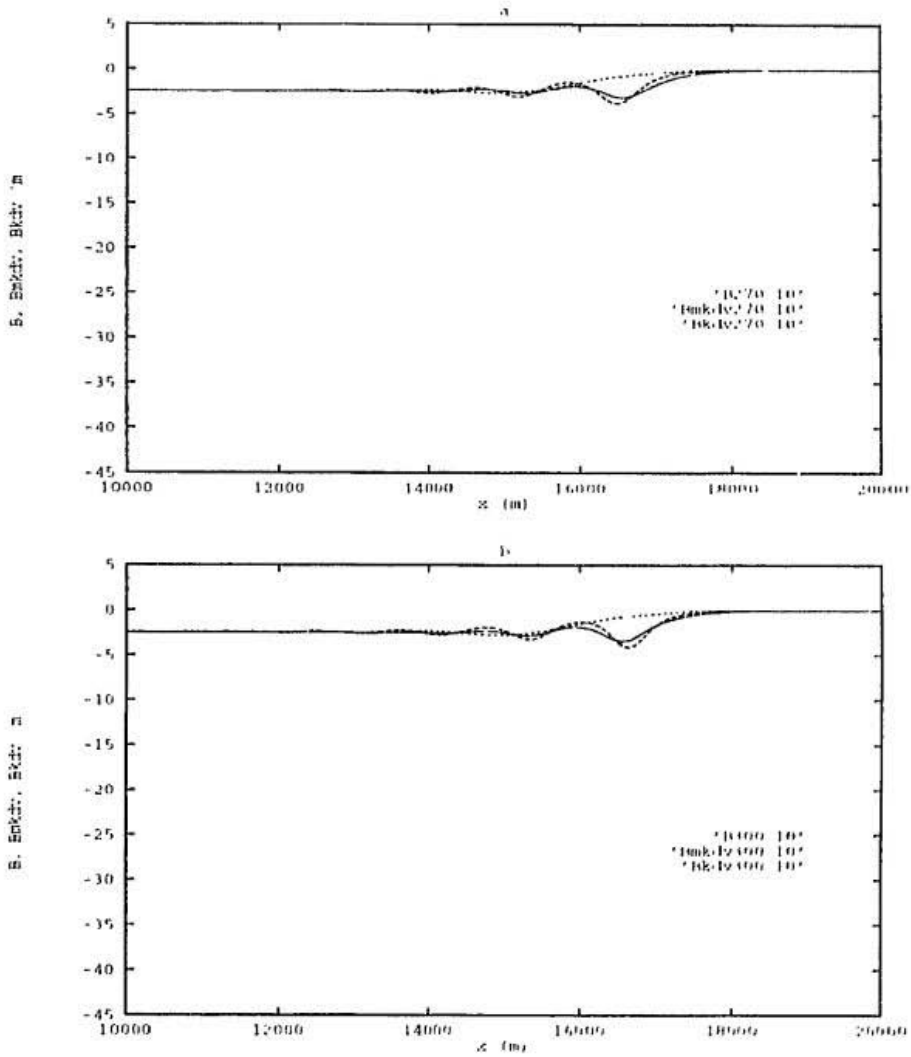

Figure 4.17: As in 4.16 (a), but for (a). $z = 270\,\mathrm{m}$. (b). $z = 300\,\mathrm{m}$.

error. But at lower depths (120 m and 150 m) B's are different. This is probably because of computational error, since at lower depths $N^2(z)$ is extremely small (see figure 2.4). Any small computational error like those involved in interpolation, etc., which is quite likely to occur and could be comparable to $N^2(z)$ itself, could cause unrealistic perturbations. Thus B measured at a depth in the lower layer could be quite different from what it should be. Therefore, it is suggested that Bs should be obtained only at depths within the significantly stratified upper layer Thus, only Bs at 270 m, 300 m and 330 m are used for comparisons.

The amplitude of the B profile changes with $\alpha^{1,0}$ as anticipated. When $\alpha^{1,0}$ changes from -0.00867 to -2.00867, B changes from 14 to 2.5, decreasing by about a factor of 5 (figure 4.9, figure 4.12 and figure 4.15). It is found in these runs that, compared with the KdV results, the mKdV results are better in that they are more stable to the changing $\alpha^{1,0}$, and match the model better in an overall sense, while the KdV results vary with $\alpha^{1,0}$, showing uncertainty to the extraction of B.

For $\alpha^{1,0} = -0.00867$ and -0.02867, as can be seen, the main features of the model results are reproduced by the mKdV theory. For instance, the steepness of the wave front, the number of significant ripples evolving at the rear of the front, the phase and the amplitude of the first few ripples and the nonlinear propagation speed, etc., all agree well with the model, except that the theoretical wave has a longer wave length resulting in a phase shift in the tail of the bore. It is also noted that the relative difference in amplitude is large for smaller ripples. As noted in section 4.2 this is believed to be due to the approximations made in deriving the KdV and mKdV equations and not due to numerical dissipation. The KdV theory, though not as good as the mKdV theory in that it is much more sensitive to $\alpha^{1,0}$, is reasonably good in producing results in qualitative agreement with the model for $\alpha^{1,0} = -0.00867$ and -0.02867. For $\alpha^{1,0} = -2.00867$ it is seen from figure 4.16 and figure 4.17 that the KdV theory completely fails. Although the mKdV theory seems still to hold, the relative difference of the amplitude, the phase and the steepness of the front from the model increases as $\alpha^{1,0}$ decreases. This indicates the beginning of the failure of the asymptotic theory due to the fact that with a large $|\alpha^{1,0}|$ the two terms are no longer a good approximation to the system. It is then concluded that the mKdV theory is good for $\alpha^{1,0}$ close to $\alpha_c^{1,0}$. Apart from this criterion it does not matter which $\alpha^{1,0}$ is chosen.

For each $\alpha^{1,0}$, B measured at 270 m, 300 m and 330 m are compared with the theory. Except for some minor differences, the agreement is equally good for each depth. This is what we expect, since the mKdV theory equally approximates the evolution of a wave obtained at any depth, as discussed in section 4.1.1. Therefore, there seems no need to do the comparison at several depths, one depth is enough.

According to the above conclusion regarding the selections of $\alpha^{1,0}$ and depth, in the following comparison, we will stick to one $\alpha^{1,0}$ value and one depth only, i.e. $\alpha^{1,0} = \alpha_c^{1,0}$ and $z = 330m$. Bs measured at $270m$ and $300m$ are only used together to show the depth independence of B.

Figures 4.18 and 4.19 show the comparison for the weak forcing case, while figure 4.20 and figure 4.21 are for the strong forcing case. Obviously, both KdV and mKdV results are in much better agreement with the model for the weak forcing case than for the moderate forcing case, though the mKdV result is even better. This is not surprising, since the asymptotic expansion used is more accurate for small waves. For waves with small amplitude the second order nonlinearity is no longer very important, thus the KdV theory is accurate enough to describe such waves.

For the strong forcing, the mKdV matches the model result reasonably well only at the front and the first ripple. At the tail the mKdV waves go out of phase and have considerably larger amplitude. The KdV solution significantly lags the

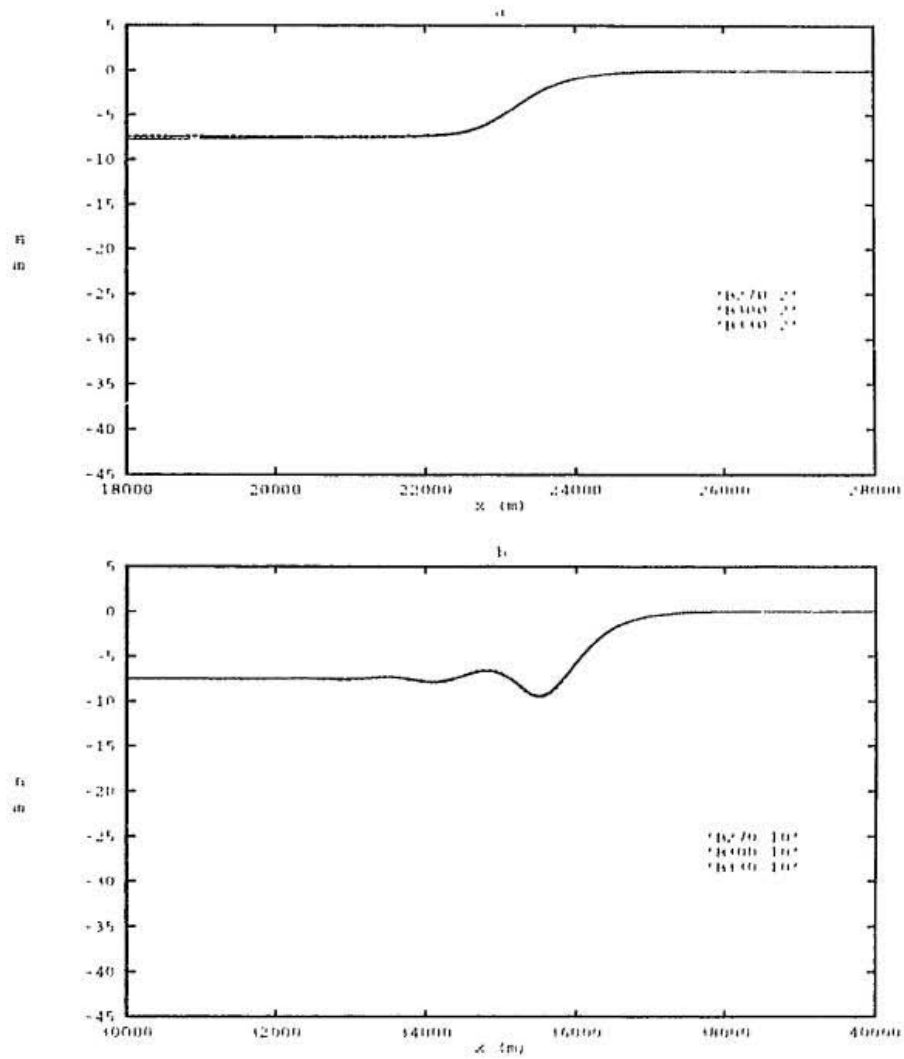

Figure 4.18: B's measured at different depths for the run with $N_2^2(z)$ and weak forcing. $\alpha^{1,0} = -0.00867, \bar{u} = 0.0m/s$, $c_0 = 0.965m/s$ and $\lambda = -1.657 \times 10^{-4}$. (a). B's at $z = 270m, 300m, 330m$ and at output 2. (b). Same as in (a) except at output 10.

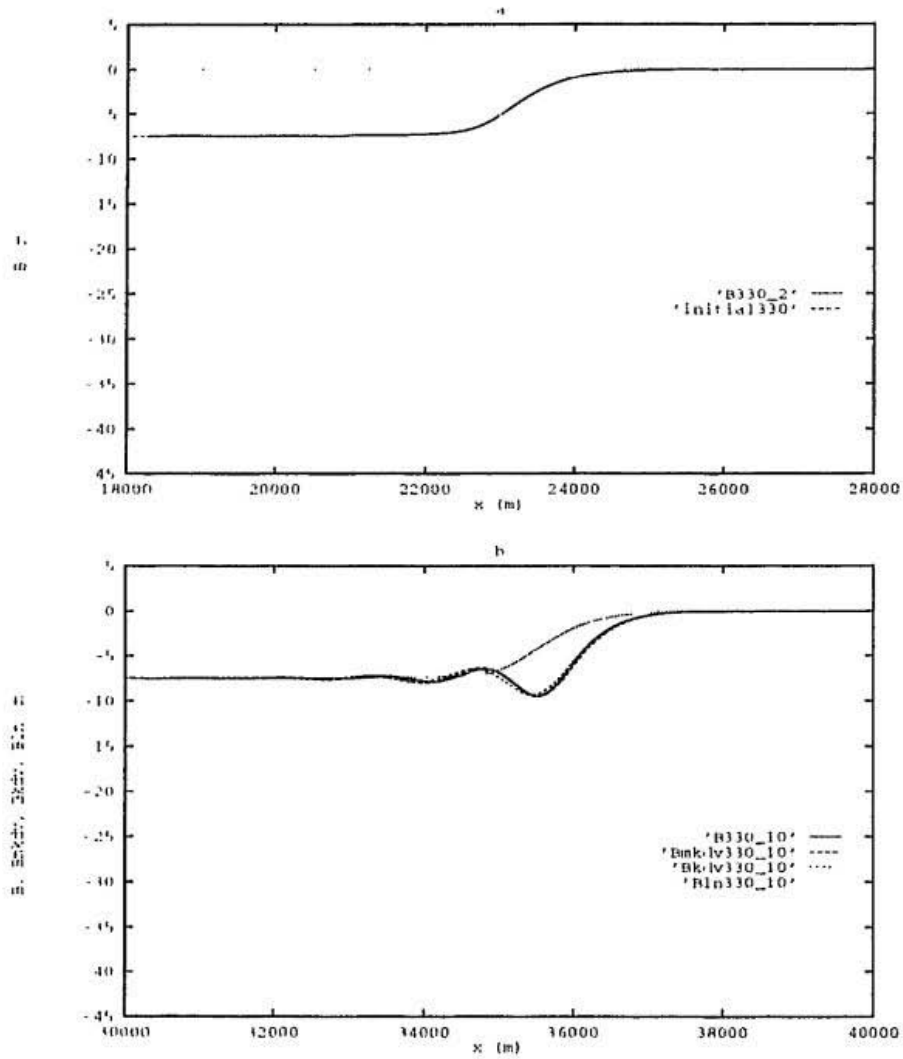

Figure 4.19: Comparison between the model and the analysis for the run with $N_2^2(z)$ and weak forcing. $\alpha^{1,0}, \bar{u}, c_0$ and λ are the same as for Figure 4.18. (a). Original and reconstructed initial wave at $z = 330m$. (b). Comparison of B_{ln}, B_{kdv} and B_{mkdv} with B at $z = 330m$ and at output 10.

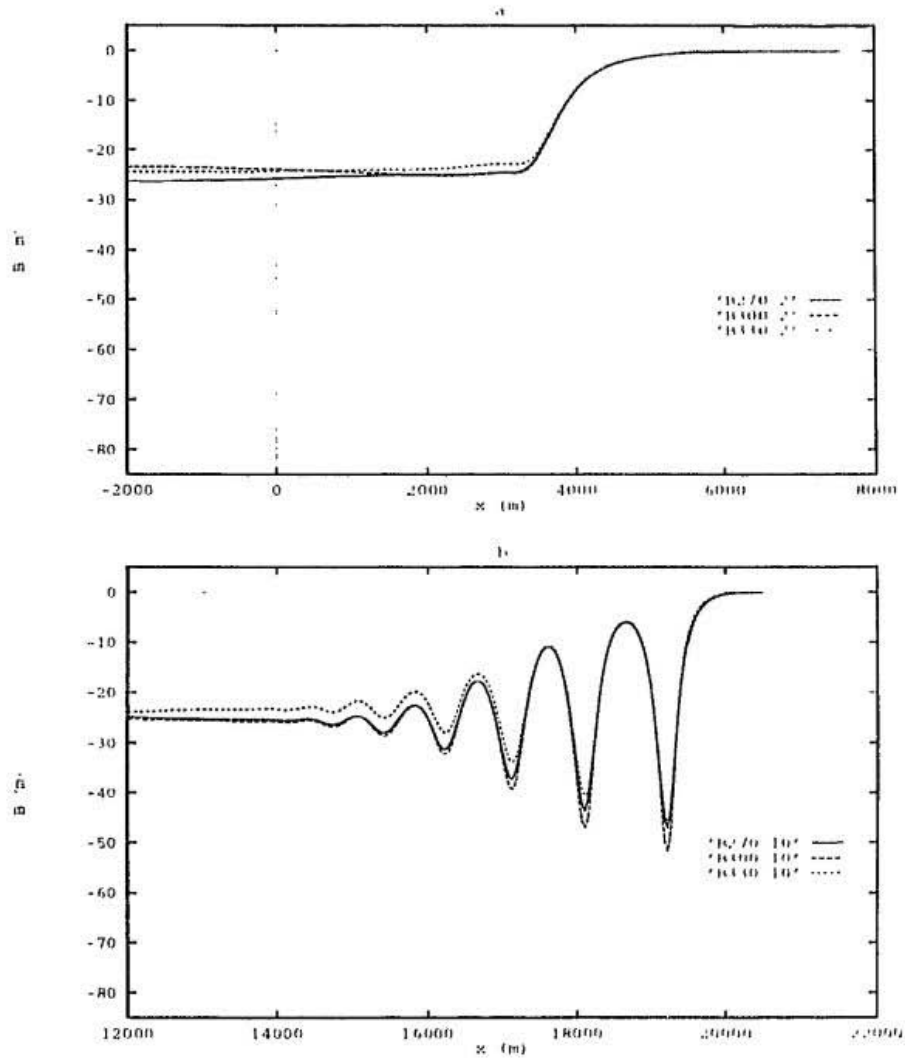

Figure 4.20: B's measured at different depths for the run with $N_2^2(z)$ and strong forcing. $\alpha^{1,0} = -0.00867, \bar{u} = 0.0m/s$, $c_0 = 0.965m/s$ and $\lambda = -1.657 \times 10^{-4}$. (a). B's at $z = 270m, 300m, 330m$ and at output 2. (b). Same as in (a) except at output 10.

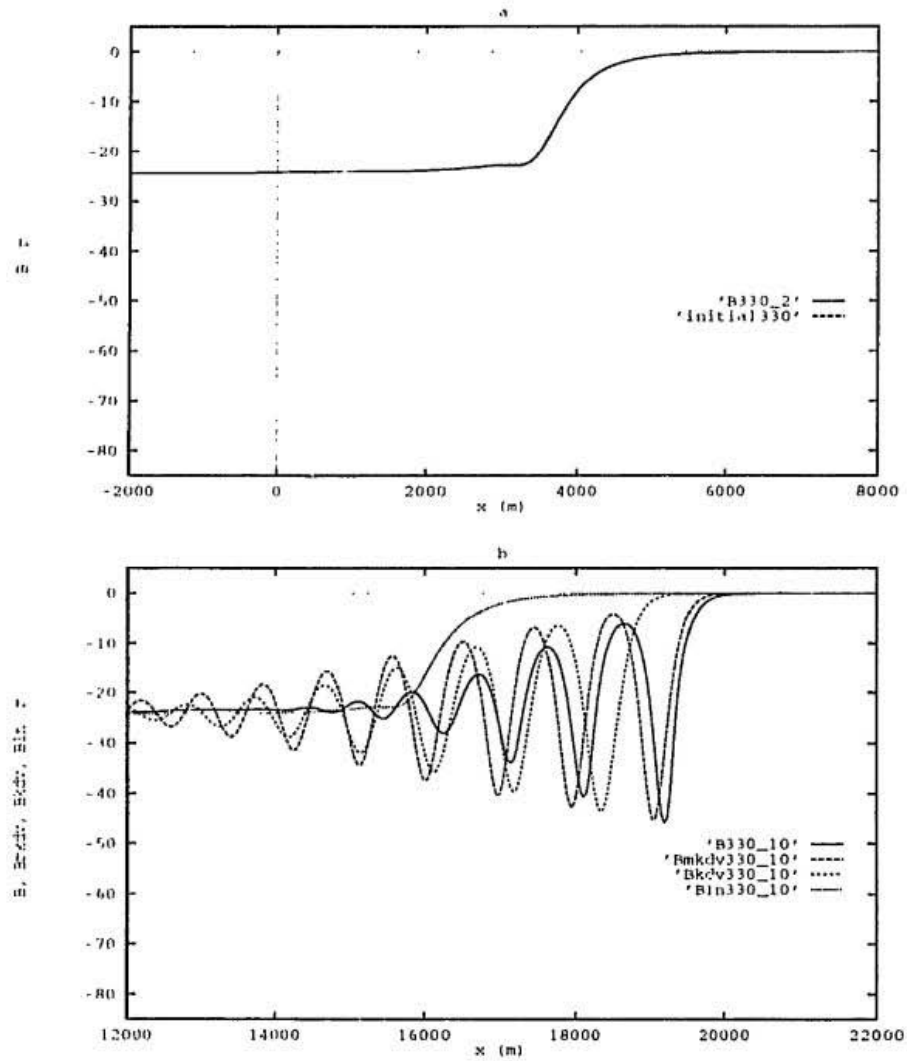

Figure 4.21: Comparison between the model and the analysis for the run with $N_2^2(z)$ and strong forcing. $\alpha^{1,0}, \bar{u}, c_0$ and λ are the same as for Figure 4.20. (a). Original and reconstructed initial wave at $z = 330m$. (b). Comparison of B_{ln}, B_{kdv} and B_{mkdv} with B at $z = 330m$ and at output 10.

model result. The trailing waves are again much larger than those in the model. As mentioned before, the differences in amplitudes of the trailing waves are not because of numerical error (a resolution test was done for waves of this amplitude) but because of the approximations made in the theory. This failure of the KdV and mKdV equations are due to the invalidity of the asymptotic theory since with large amplitude neglecting higher order terms is not appropriate. The theory would be improved by adding additional terms to it. The failure could also be due to the generation of a mode-two wave due to nonlinear interactions. This phenomenon does not appear to be significant in this case because the small variations of B with depth do not correspond with the linear mode-two vertical mode function.

Wave propagation speeds and wavelengths are presented in figure 4.22-4.24. The compared quantities are plotted vs. the output number, therefore the propagation speeds can be regarded as averaged over an output interval of 1600s. Figure 4.22 (a) shows the wavelengths of the first two ripples in the model result, while figure 4.22 (b) is the speed of the model wave front. The wavelength is measured as the distance between two successive troughs, and the speed of the front is measured as the average speed at which the first trough has traveled during an output interval. Then the difference in wavelength between the theory and the model (KdV/mKdV wavelength minus model wavelength) is plotted in figure 4.23 for the moderate and strong forc-

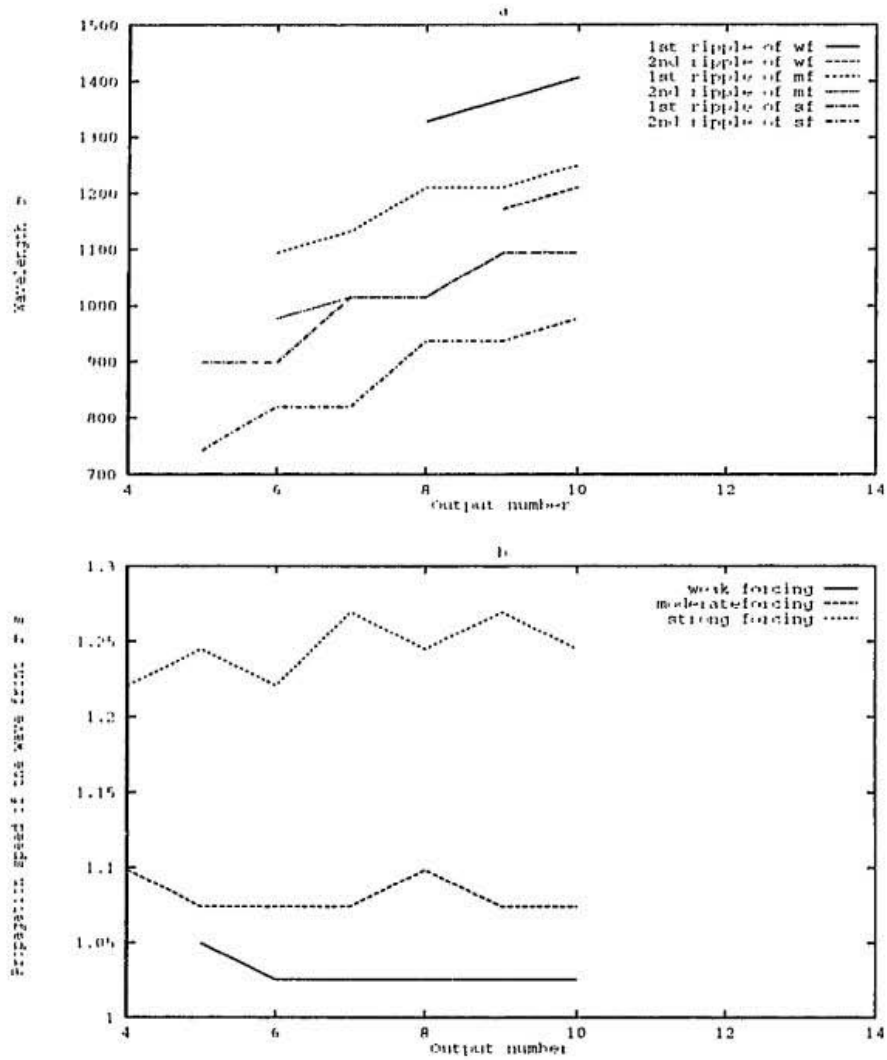

Figure 4.22: Model result for the run with $N_2^2(z)$. (a). Model wavelength of the first two ripples for each forcing. (b). Model propagation speed of the wave front for each forcing. Note that linear propagation speed is $c_0 = 0.965\,\mathrm{m/s}$.

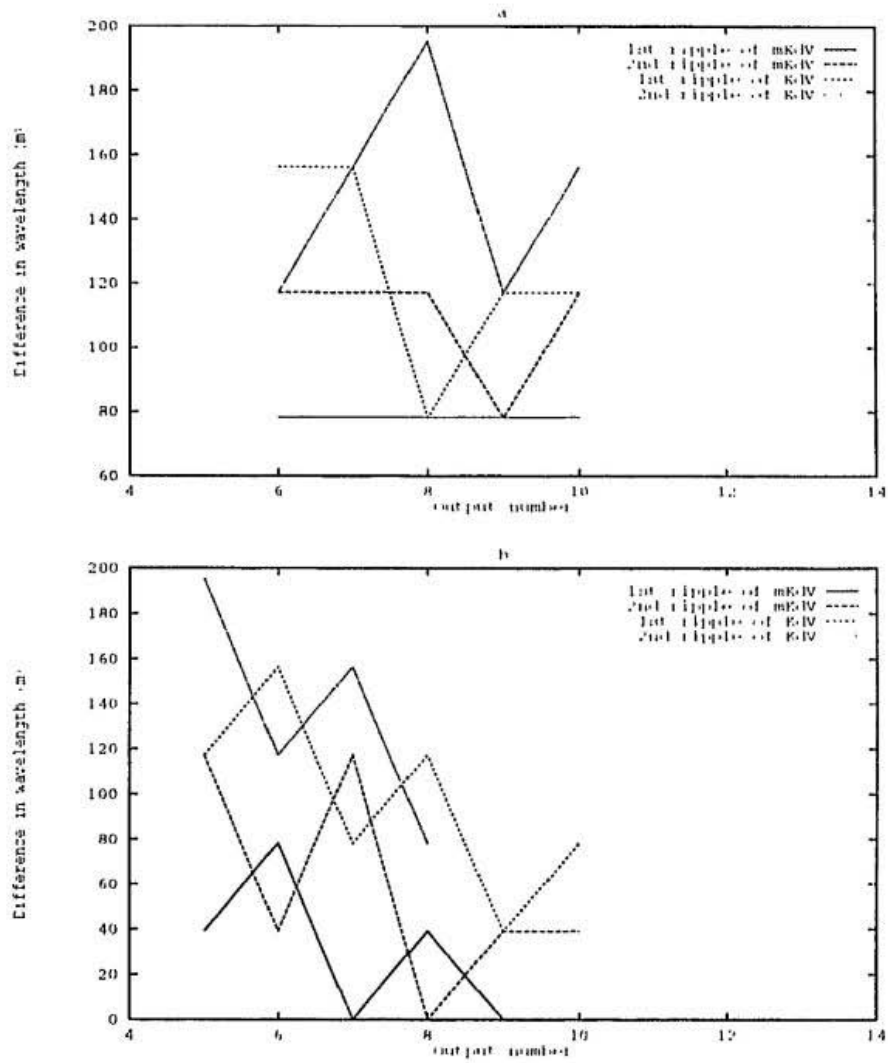

Figure 4.23: The wavelength difference (KdV/mKdV wavelength - model wavelength) for the run with $N_2^2(z)$. (a). Wavelength difference in the moderate forcing case. (b). Wavelength difference in the strong forcing case.

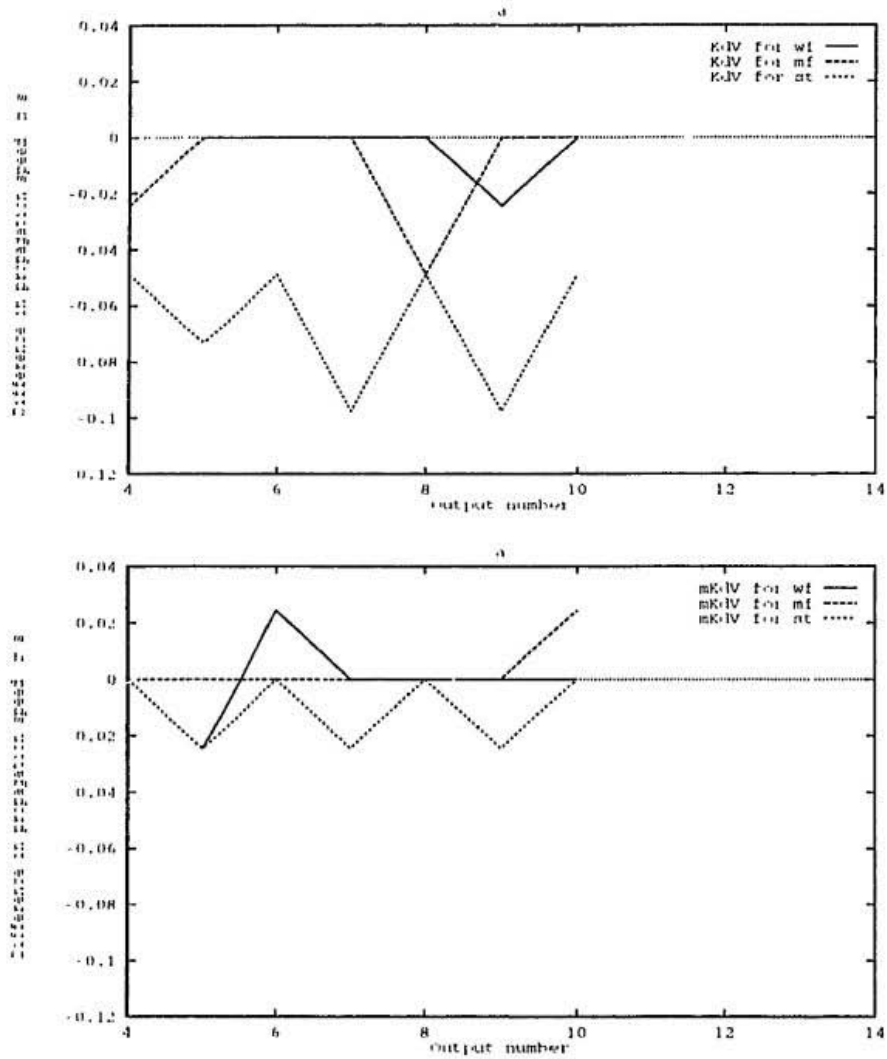

Figure 4.24: The propagation speed difference (KdV/mKdV speed - model speed) for the runs with $N_2^2(z)$. (a). For the KdV solutions. (b). For the mKdV solutions.

ings. The difference in speed (KdV/mKdV speed minus model speed) is shown in figure 4.24. Note that the x resolution is $\Delta x \approx 40\,\mathrm{m}$. Therefore, the measuring error involved is $40m$ for wavelength and $0.025\,\mathrm{m/s}$ for propagation speed.

The model wavelengths vary between $750\,\mathrm{m}$ and $1400\,\mathrm{m}$. They decrease as the front amplitude increases and increase with time. The amplitudes of the ripples increase with both the front amplitude and time. The decreasing wavelength with the front amplitude is a direct result of strong nonlinearity. The larger the front, the larger the steepening, and the shorter the dispersed waves. At the same time, a larger front contains more energy thus dispersing larger ripples. The growing amplitudes of the ripples with time indicates that these ripples are not solitons at this stage of their evolution.

The theory predicts the same wavelength variation trend, but the wavelength is systematically longer than that of the model wave. In particular, the mKdV waves are about $1-3\,\Delta x$ longer while the KdV waves are $2-5\,\Delta x$ longer. The mKdV waves are in better agreement with the model waves.

The propagation speed of the model front is rather constant for each forcing case (only a slight increase with time in the strong forcing case), but of course increases with frontal amplitude. The nonlinear propagation speed is about $2.5-3\%, 7-10\%$ and $22-25\%$ larger than the linear speed in the weak, moderate and strong forcing

cases, respectively. The theoretical propagation speeds are in very good agreement with the model (within the measuring error), except for the KdV wave in the strong forcing case.

It is now clear that for waves with up to moderate amplitude, the difference in wavelength, rather than propagation speed, between the mKdV and the model is responsible for the phase shift at the bore tail. Also, the theory is not quite appropriate for waves with a scaled amplitude larger than $\epsilon = 0.07$.

4.3.2 Runs with smooth $N_1^2(z)$

For the smooth $N_1^2(z)$ ($q = 0.07$), $\alpha_c^{1,0} = -0.00774$. The associated $E^{1,0}(z)$ is shown in figure 4.25. The significantly stratified layer starts at $z_c = 260\,\mathrm{m}$.

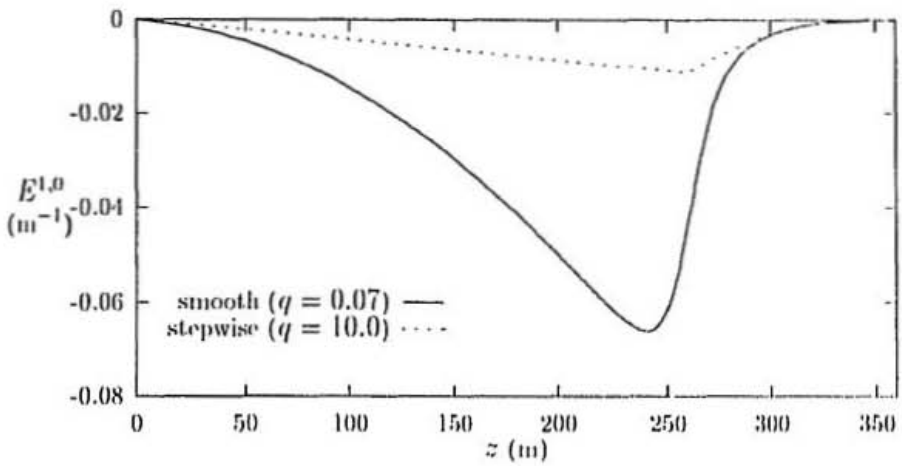

Figure 4.25: $E^{1,0}(z)$ with $\alpha^{1,0} = \alpha_c^{1,0}$ for (a). the smooth $N_1^2(z)$ (slope $q = 0.07$). (b). the stepwise $N_1^2(z)$ (slope $q = 10.0$).

In this group of comparisons we take $\alpha^{1,0} = \alpha_c^{1,0}$. The measuring depths are the same, i.e. 270 m, 300 m and 330 m within the stratified layer, but the comparisons are only made at $330m$. The sufficiency of choosing only one $\alpha^{1,0}$ and one depth has been justified in the previous section. The forcings are the same as before. The results are presented in figures 4.26-4.31. Figures 4.32-4.34 give detailed comparisons of the

wavelength and speed.

It is found that most of the observations and comments made for the runs with $N_2^2(z)$ hold for these runs, too. For instance, for the moderate forcing, the steepness of the front, the number of significant ripples, the phase and amplitudes of these ripples and propagation speed, etc., are predicted quite well by the theory. The mKdV result is again better than the KdV result. The better agreement between the KdV and the model in figure 4.29 is coincidental. The KdV solution is very sensitive to $\alpha^{1,0}$ while the sensitivity of the mKdV is much less. The value of $\alpha^{1,0}$ used here happens to make the KdV solution very accurate.

The disagreement is again in the phase shift and larger amplitude of the small waves at the bore tail. For the weak forcing both the mKdV and KdV waves match the model very well. The mKdV and KdV waves are almost identical, indicating the unimportance of the second-order nonlinearity. For the strong forcing, even mKdV theory begins to fail. It is noted in the strong forcing case that the KdV/mKdV bore tails tilt up. This is because the initial depression was quite narrow so that the tail of the undular bore overlaps with the rising isopycnals at the back of the depression.

Investigating the detailed comparison figures 4.32-4.34 we find the same variation of the model wavelength, i.e. decreasing with forcing and increasing with time, within a range of 1050 – 1370 m. One difference is that since the second-order non-

linearity λ is very small for $N_1^2(z)$, the mKdV and KdV waves are both $1-3\Delta x$ shorter than the model wave. As for the propagation speed, the same observation has been found, e.g. rather constant speeds of the model wave front for each forcing, the speed increasing with the forcing. The speed differences between the theory and the model (except the KdV wave for the strong forcing) are within the measuring error. It is inferred that the observed phase shift at smaller ripples also is a result of the discrepency in wavelength. The ratio of nonlinear speed to linear speed is larger. For instance, the ratio is about 20% for the moderate forcing, and $30-32\%$ for the strong forcing. This indicates that the nonlinear effect for the smooth $N_1^2(z)$ is stronger than for $N_2^2(z)$, since the waves in both cases are of the same size.

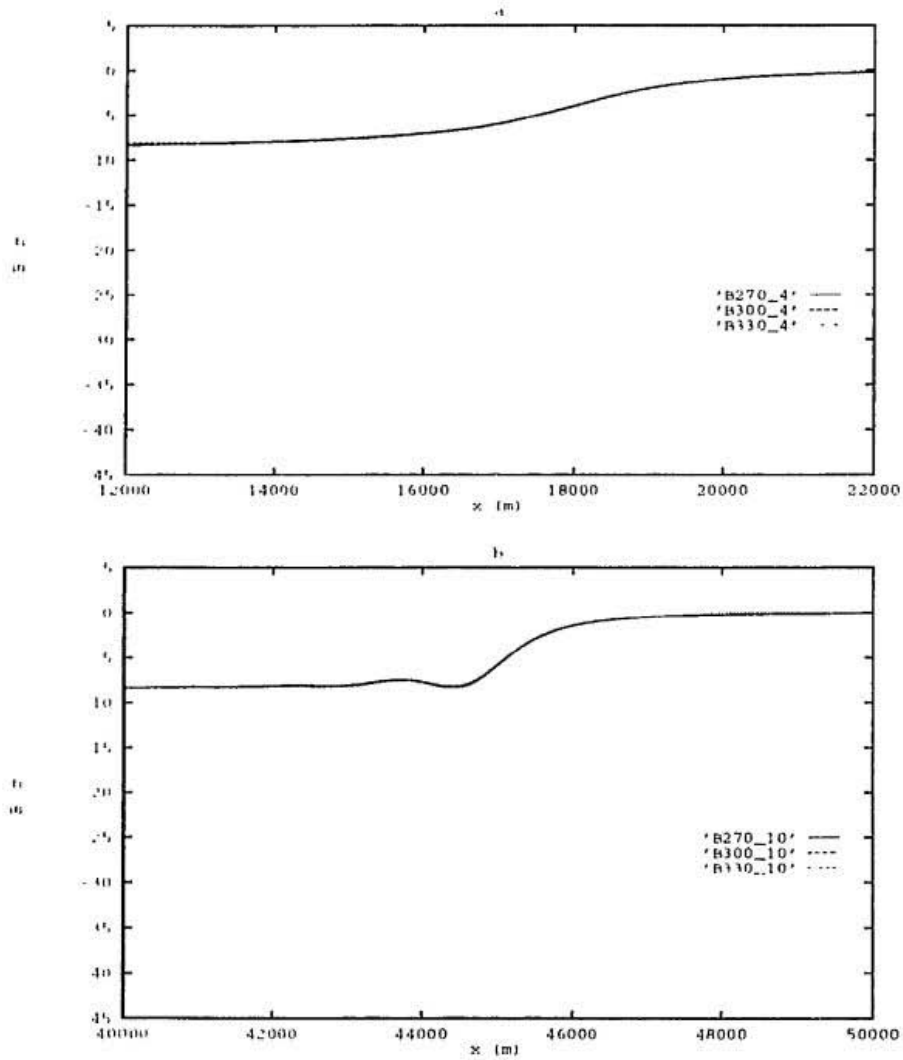

Figure 4.26: B's measured at different depths for the run with smooth $N_1^2(z)$ and weak forcing. $\alpha^{1,0} = -0.00774, \bar{u} = 0.194m/s$, $c_0 = 2.49995m/s$ and $\lambda = -2.982 \times 10^{-5}$. (a). B's at $z = 270m, 300m, 330m$ and at output 4. (b). Same as in (a) except at output 10.

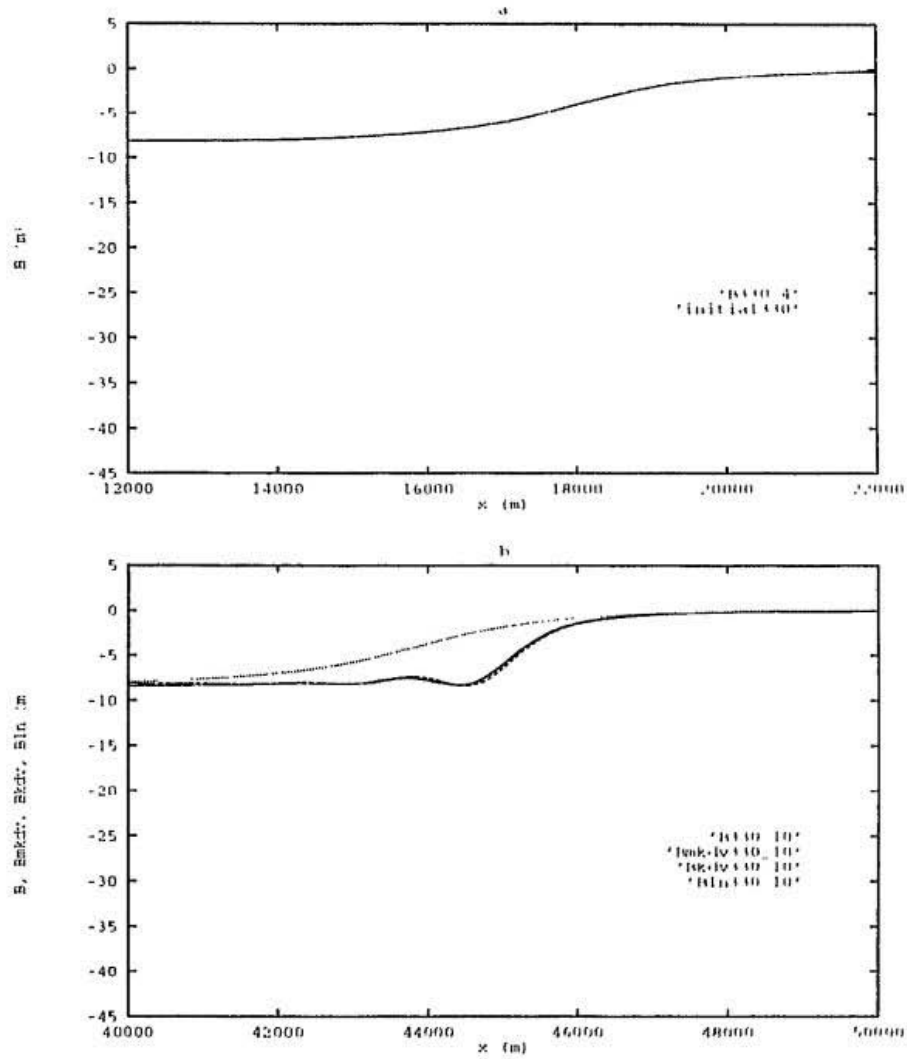

Figure 4.27: Comparison between the model and the analysis for the run with smooth $N_1^2(z)$ and weak forcing. $\alpha^{1,0}, \bar{u}, c_0$ and λ are the same as for Figure 4.26. (a). Original and reconstructed initial wave at $z = 330m$. (b). Comparison of B_{kn}, B_{kdv} and B_{nkdv} with B at $z = 330m$ and at output 10.

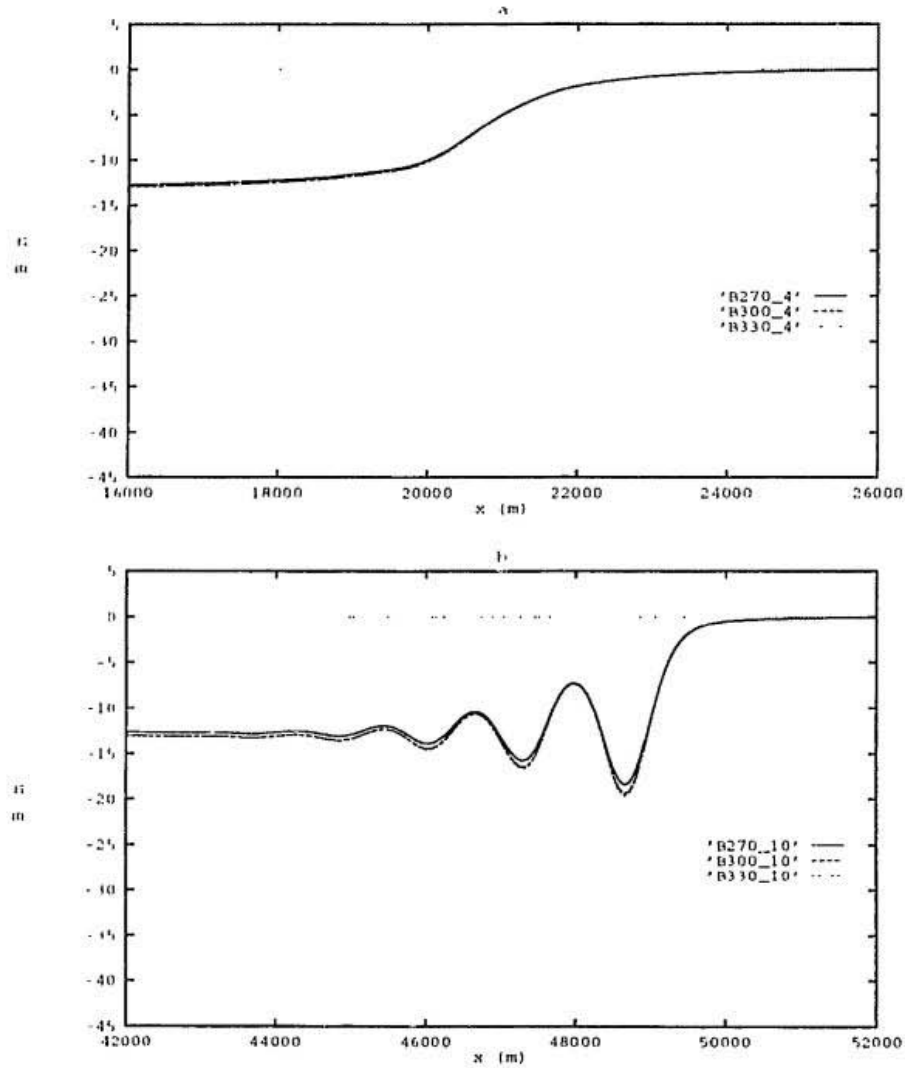

Figure 4.28: B's measured at different depths for the run with smooth $N_1^2(z)$ and moderate forcing. $\alpha^{1,0} = -0.00774, \bar{u} = 0.194m/s$, $c_0 = 2.49995m/s$ and $\lambda = -2.982 \times 10^{-5}$. (a). B's at $z = 270m, 300m, 330m$ and at output 4. (b). Same as in (a) except at output 10.

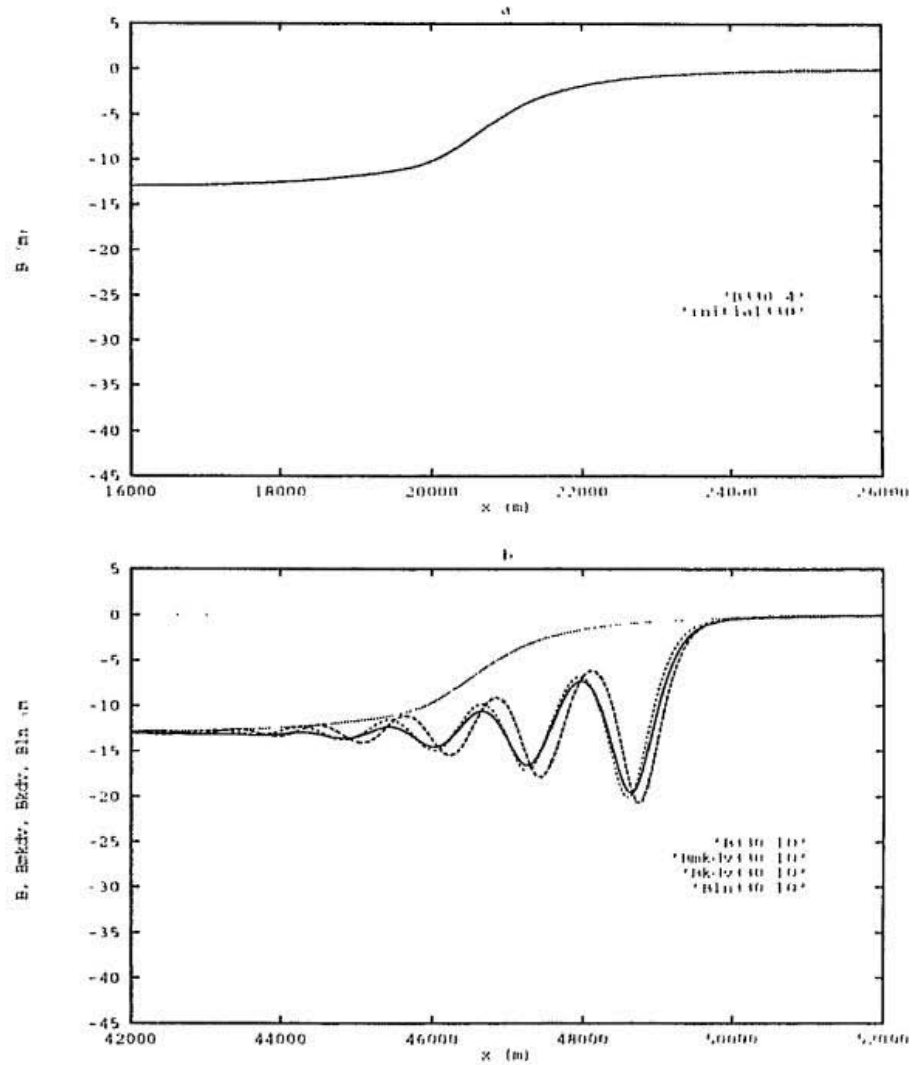

Figure 4.29: Comparison between the model and the analysis for the run with smooth $N_1^2(z)$ and moderate forcing. $\alpha^{1,0}, \bar{u}, c_0$ and λ are the same as for Figure 4.28. (a). Original and reconstructed initial wave at $z = 330m$. (b). Comparison of B_{lin}, B_{kdv} and B_{mkdv} with B at $z = 330m$ and at output 10.

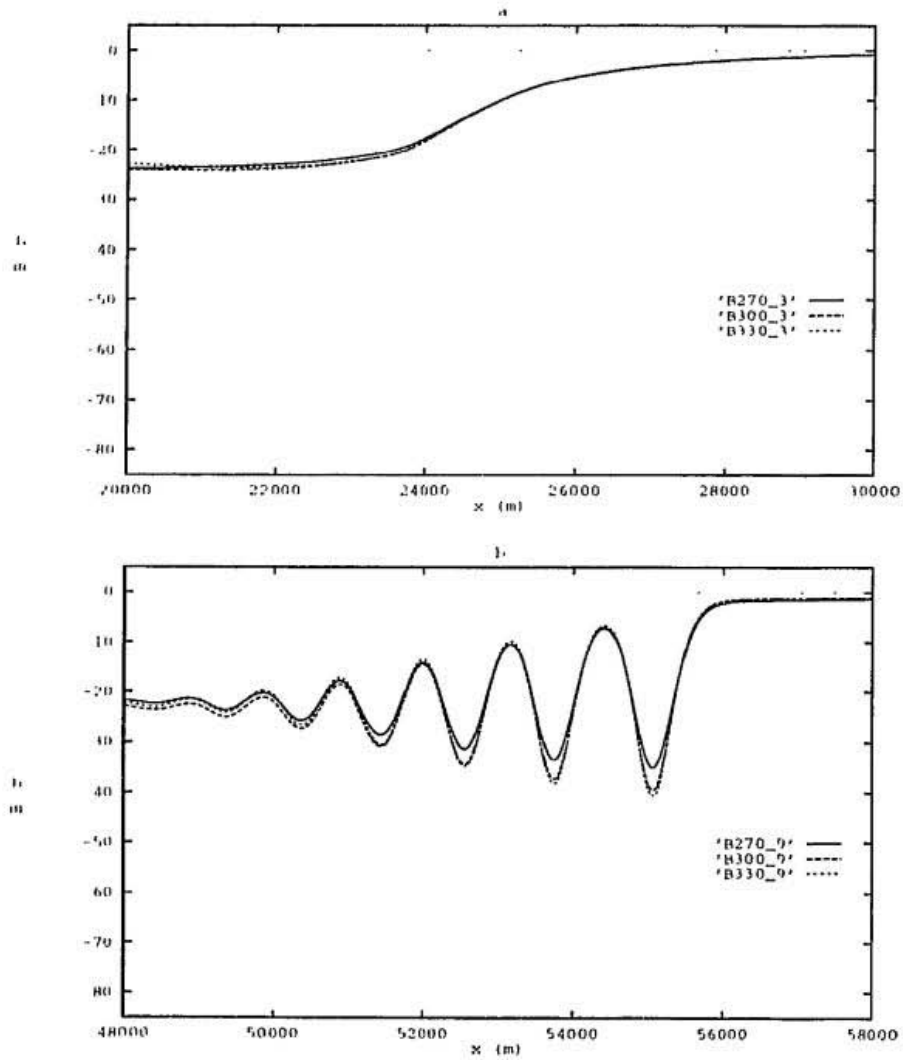

Figure 4.30: B's measured at different depths for the run with smooth $N_1^2(z)$ and strong forcing. $\alpha^{1,0} = -0.00774, \bar{u} = 0.078m/s$, $c_0 = 2.49995m/s$ and $\lambda = -2.982 \times 10^{-5}$. (a). B's at $z = 270m, 300m, 330m$ and at output 4. (b). Same as in (a) except at output 10.

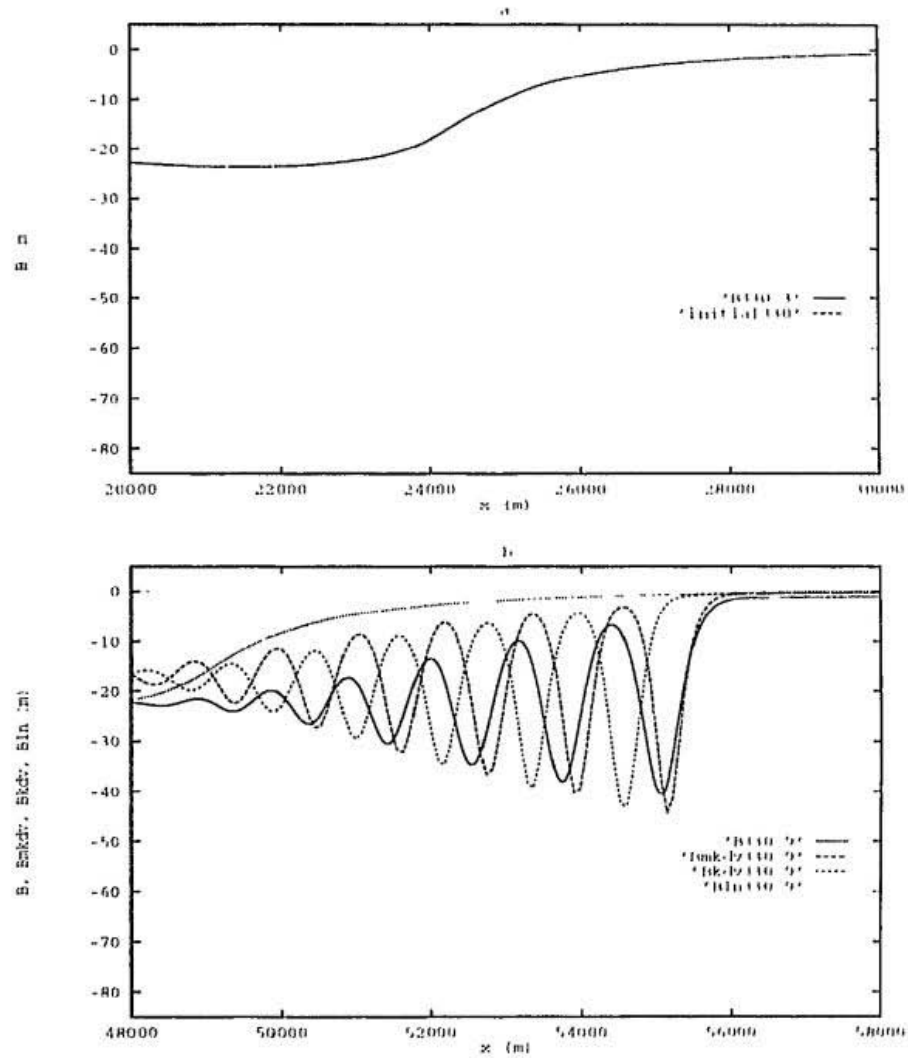

Figure 4.31: Comparison between the model and the analysis for the run with smooth $N_1^2(z)$ and strong forcing. $\alpha^{1,0}, \bar{u}, c_0$ and λ are the same as for Figure 4.30. (a). Original and reconstructed initial wave at $z = 330m$. (b). Comparison of B_{lin}, B_{kdv} and B_{mkdv} with B at $z = 330m$ and at output 10.

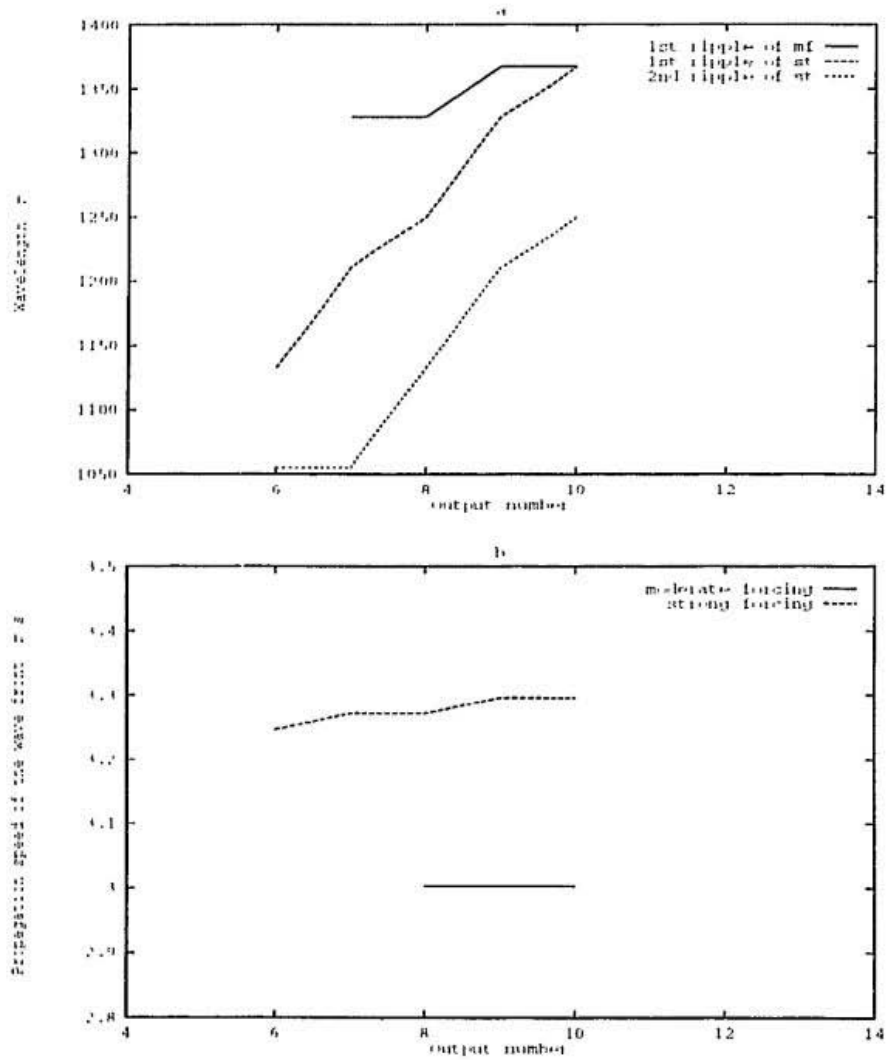

Figure 4.32: Model result for the run with smooth $N_1^2(z)$. (a). Model wavelengths of the first two ripples for each forcing. (b). Model propagation speed of the wave front for each forcing. Note that linear propagation speed is $c_0 = 2.5\,\mathrm{m/s}$.

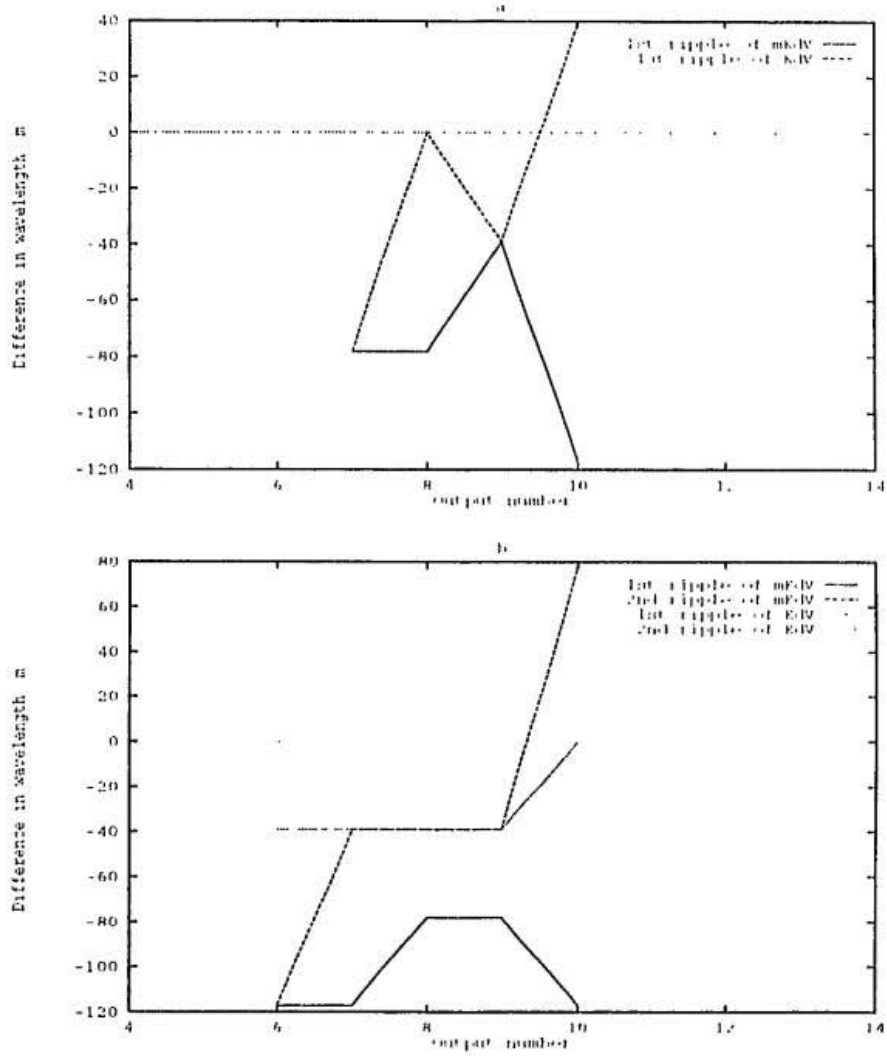

Figure 4.33: The wavelength difference (KdV/mKdV wavelength - model wavelength) for the runs with smooth $N_1^2(z)$. (a). Wavelength difference in the moderate forcing case. (b). Wavelength difference in the strong forcing case.

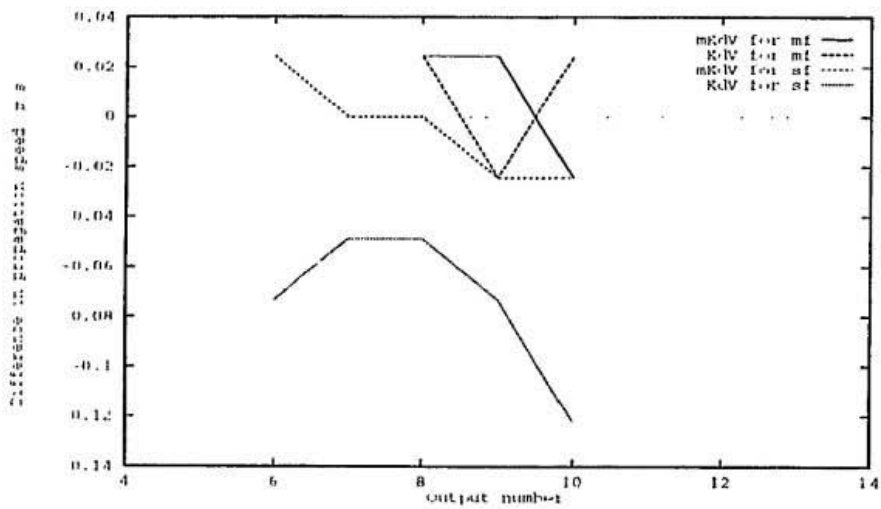

Figure 4.34: The propagation speed difference (KdV/mKdV speed - model speed) for the run withs smooth $N_1^2(z)$.

4.3.3 With a stepwise $N_1^2(z)$

$E^{1,0}(z)$ for this stepwise $N_1^2(z)$ is shown together with that of the smooth $N_1^2(z)$ in figure 4.25. With a large q, $N_1^2(z)$ approximates a discontinuous stepwise function. Therefore, expansion (4.2) is only valid above z_c where $N_1^2(z)$ is non-zero. For convenience, the $\frac{(N^2)_z}{2N^2 c_0}\phi^2$ term (being zero away from z_c where $N_1^2(z)$ is constant) is removed from $E^{1,0}(z)$.

One of the purposes of considering this stratification is to see if the flow experiences some abrupt change when $N_1^2(z)$ becomes discontinuous, i.e., when $q \to \infty$. The model results show that there is no sudden change in the flow pattern for the stepwise $N_1^2(z)$. The model was also run with a discontinuous stepwise $N_1^2(z)$. There is no distinguishable difference in the flow pattern in comparison with the present $N_1^2(z)$. The flow is rather insensitive to the slope parameter, at least for the range of $q \geq 0.07$, as can be seen in figure 4.37.

Since the results are quite similar to those of the smooth $N_1^2(z)$ case we present only the result for the moderate forcing in figures 4.35- 4.36.

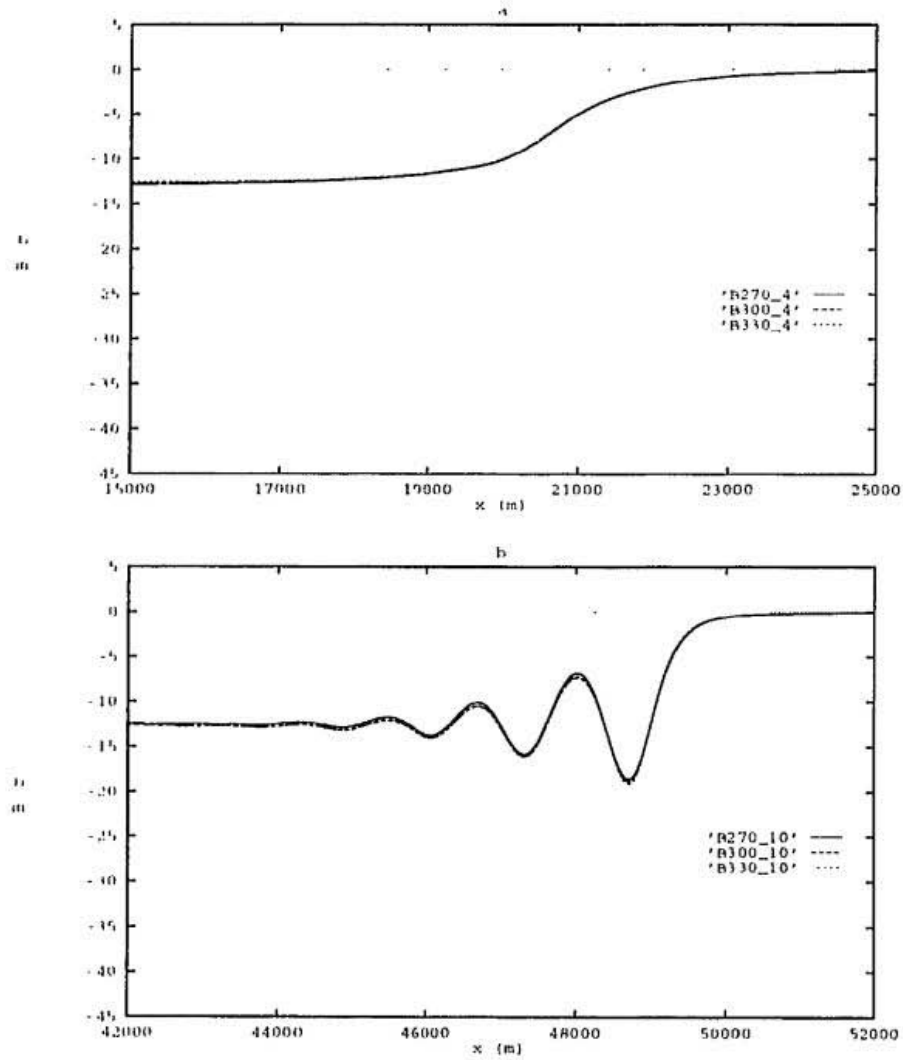

Figure 4.35: B's measured at different depths for the run with stepwise $N_1^2(z)$ and moderate forcing. $c^{1,0} = -0.00796, \bar{u} = 0.194m/s$, $c_0 = 2.50789m/s$ and $\lambda = -2.907 \times 10^{-5}$. (a). B's at $z = 270m, 300m, 330m$ and at output 4. (b). Same as in (a) except at output 10.

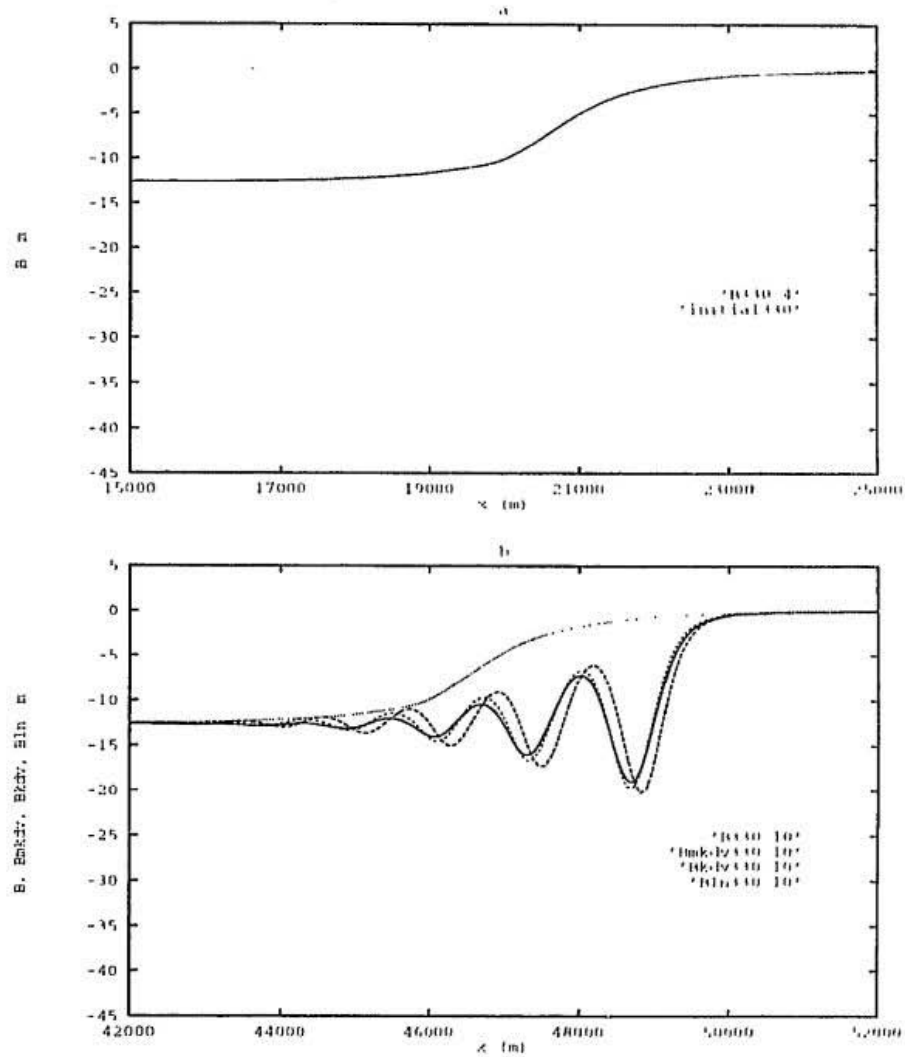

Figure 4.36: Comparison between the model and the analysis for the run with stepwise $N_1^2(z)$ and moderate forcing. $\alpha^{1,0}, u, c_0$ and λ are the same as for Figure 4.35. (a). Original and reconstructed initial wave at $z = 330m$. (b). Comparison of B_{ln}, B_{kdv} and B_{mkdv} with B at $z = 330m$ and at output 10.

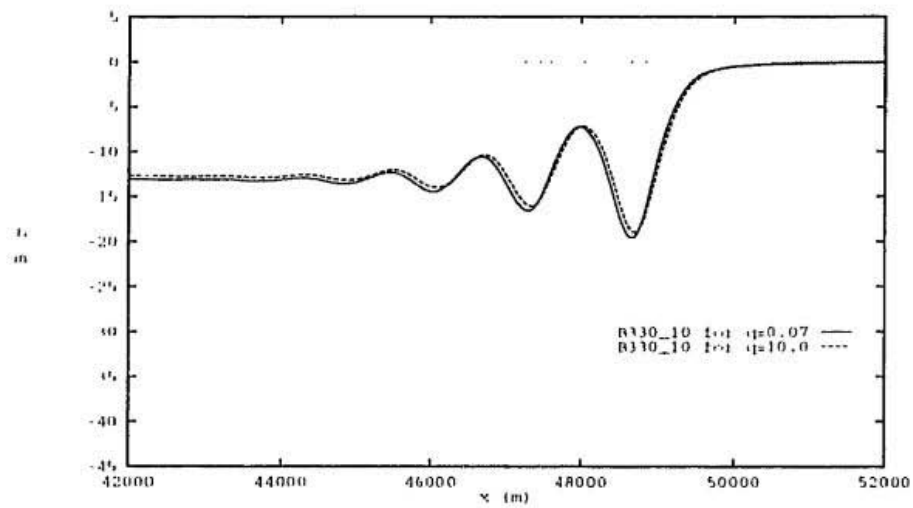

Figure 4.37: Comparison between two model runs, one with the smooth $N_1^2(z)$ and the other with the stepwise $N_1^2(z)$.

4.3.4 Effects of rotation

It is of interest to examine the validity of applying weakly nonlinear theories, which do not take rotation into account, to oceanic situations where rotational effects are present. Rotation affects the evolution of waves longer than or comparable to the internal Rossby radius, but does not affect short waves. Houghton [1969] investigated rotational effects on the formation of hydraulic jumps using an approximation to a $1\frac{1}{2}$ layer model. His result suggests that hydraulic jumps would be less intense and take longer to form, owing to rotation.

In order to study rotational effects we initialized the model with a depression having a frontal length scale of 15 km. The Coriolis parameter is taken as $f = 10^{-4}\,s^{-1}$, and the non-rotating linear propagation speed of mode-one wave is $c_0 = 0.965\,m/s$ as before. Thus, the length of the front is larger than the Rossby radius $R = c_0/f = 9.65\,km$ and rotational effects will be important. To ensure an undular bore appearing within the 16000s evolution time, we have specified a large initial amplitude, corresponding to the strong forcing case, for a stronger nonlinear steepening.

The comparison of the model results for rotating and non-rotating cases is shown in figure 4.38. It is seen that the amplitude of the front in the rotating case

decreases during propagation, and the wave tail tilts up. At later outputs, the front is not as steep as in the non-rotating case, and the undular bore is less intense. This can be explained using a linear theory. Under rotation, the dispersion relation becomes

$$\omega^2 = c_0^2 k^2 + f^2, \tag{4.18}$$

where ω is the frequency, k is the wave number. Thus, the linear group velocity is given by

$$c_g = c_0(1 + \frac{1}{R^2 k^2})^{-\frac{1}{2}}. \tag{4.19}$$

Therefore, long waves are dispersive and very short wave components are non-dispersive and are unaffected by rotation. Since long components are left behind, the amplitude of the front diminishes, hence the nonlinear steepening is greatly reduced. Thus, the initial effect of rotation is to reduce the amplitude of the front, resulting in a delayed appearance of the undular bore. The undular bore is also smaller in amplitude. Once the front gets sufficiently steep its evolution is no longer significantly modified by rotational effects. The rising tail is due to the trailing iong waves (see figure 4.38).

Our theory is derived for non-rotating systems. However, after long wave components have been dispersed and the wave front has become sufficiently short, it is possible that the theory may be valid at the wave front where the rotation effect is no longer significant. Figure 4.39 shows the result of applying the theory to the wave

front under the rotation. The agreement between the mKdV theory and the model is fairly good for the front and the first ripple, but not for others. The disagreement comes partly from the fact that the model front is still dispersing out longer components and its amplitude is diminishing. This indicates the persistence, although not large, of the rotation effect. Better agreement may be expected if the comparison starts at some later output. Another reason for the disagreement may be that the theory itself begins to fail due to the large amplitude of this strong forcing case. Figure 4.40 shows a case with moderate forcing, the comparison is better.

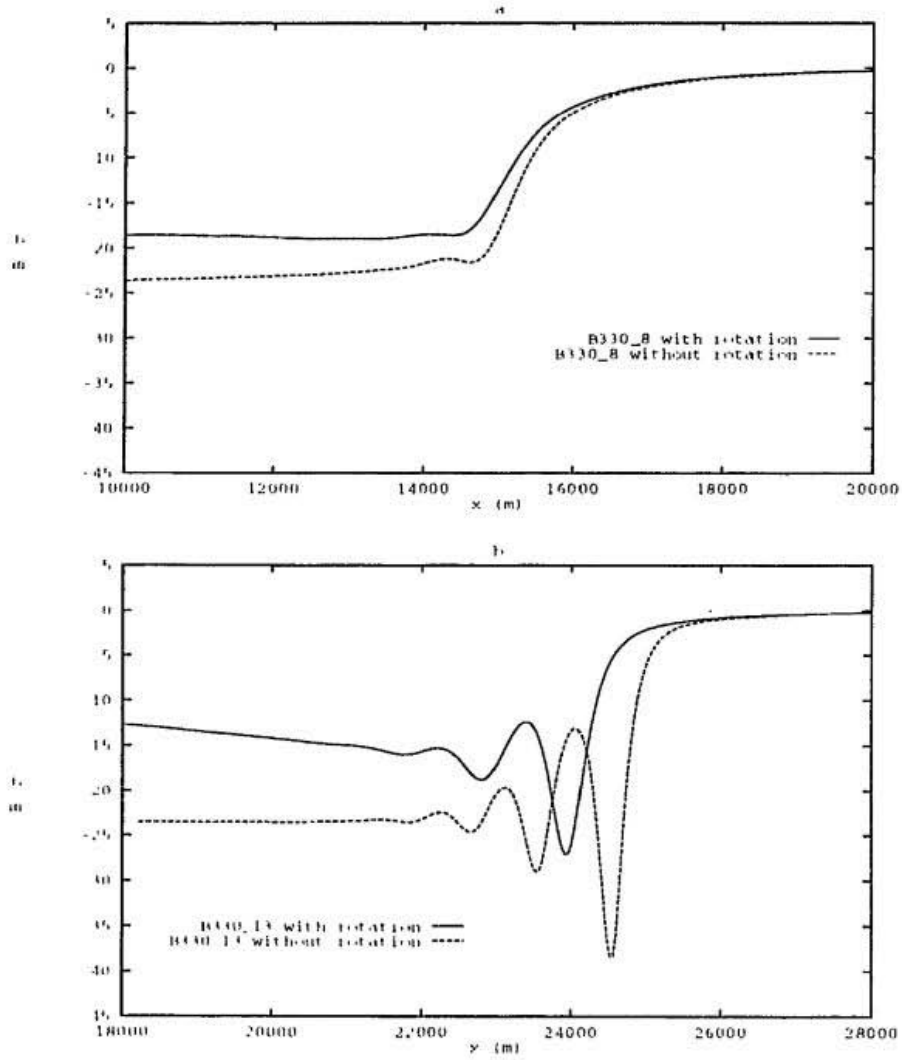

Figure 4.38: Comparison between the model results with and without rotation, for $N_2^2(z)$ and strong forcing case. (a). At output 8. (b). At output 13.

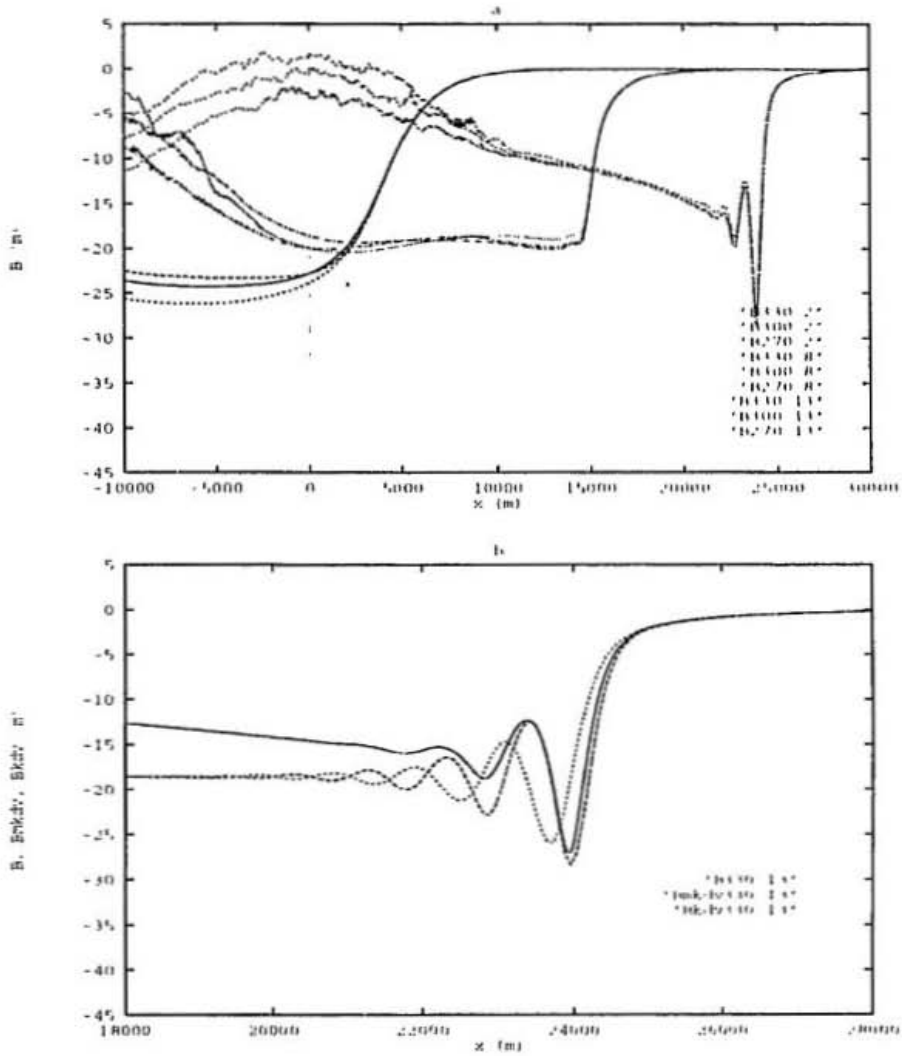

Figure 4.39: Application of the theory to the rotating model result for $N_2^2(z)$ and strong forcing. (a). B's measured at $270m$, $300m$ and $330m$, and at different evolution times. (b). Comparison of B_{kdv} and B_{mkdv} with rotating B at $z = 330m$ and at output 13. The wave at output 8 is picked up as the initial for the theory.

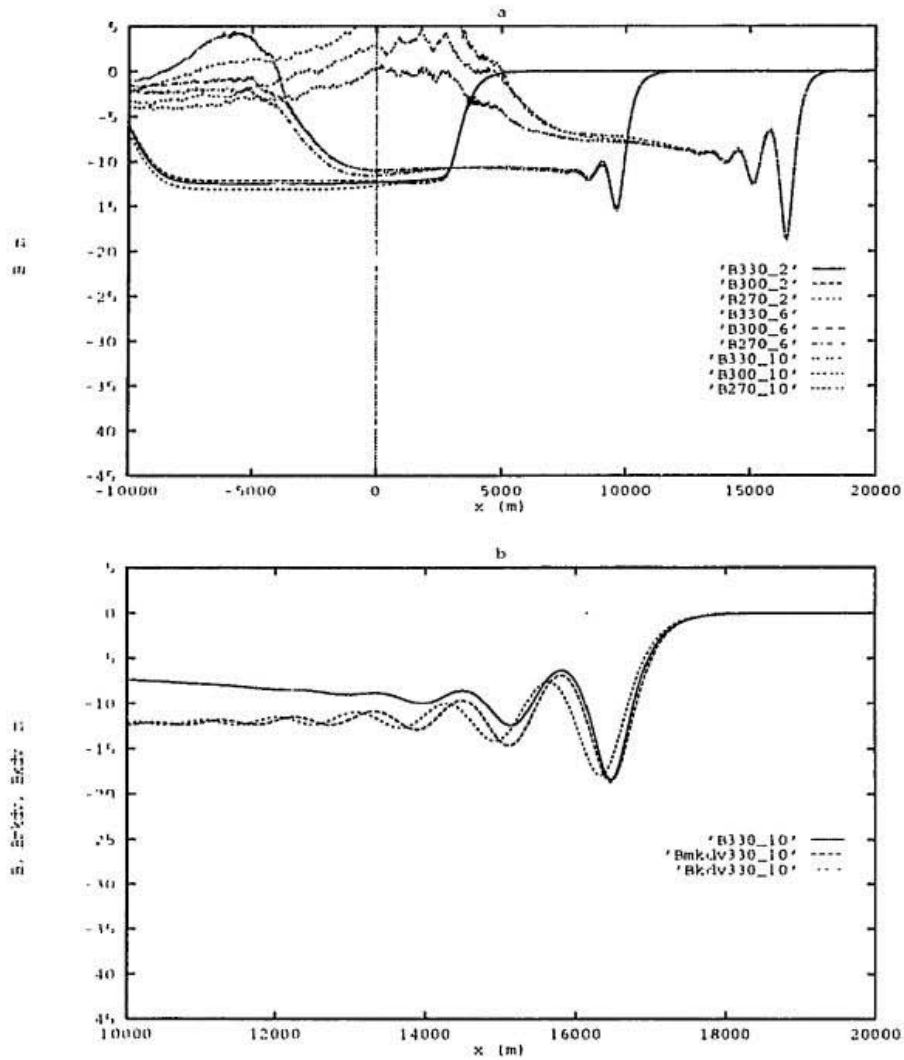

Figure 4.40: As in Figure 4.39 but for moderate forcing.

4.4 Discussion

Along with the comparisons, we have already made some comments and discussed some of the results. In this section, a more general discussion will be given.

The observed evolution of the front into an undular bore in both the model results and in the weakly nonlinear theories is a consequence of nonlinear steepening followed by the dispersion of short waves. When the front is sufficiently steep, short waves are generated which, having a smaller propagation speed than that of the wave front, are left behind. Any given wave grows in wavelength and amplitude with time and propagates at almost a constant speed. Since larger waves have larger propagation speeds, the waves travel in a group with amplitude ranked in order. Meanwhile, smaller waves successively appear at the bore tail because of dispersion, resulting in the continual lengthening of the undular bore. This process can be viewed as waves embedded in a wave packet whose envelope is continually lengthening.

In our weakly nonlinear cases, the linearized KdV and mKdV equations give the same dispersion relation with

$$C = c_0 + s\,k^2, \tag{4.20}$$

$$C_g = c_0 + 3\,s\,k^2, \tag{4.21}$$

where C, C_g are linear dispersive phase and group velocities, respectively, and c_0 and s

are as in the mKdV equation. Since $s < 0$ for the cases studied here, the group velocity C_g is less than the phase velocity C. (4.20) and (4.21) apply to the undular bore tail where small oscillations are nearly linear. The front of the wave envelope moves with the bore front, while the trailing envelope edge moves at speed C_g which is slower than the phase speed C of the waves. Thus, in a reference frame moving with the front, one would see energy leaking at the bore tail, i.e., smaller waves successively appear and propagate in the negative direction (Fornberg & Whitham [1978] discussed the phenomena using a modulation approach.). By steepening the wave front nonlinearity transfers energy from long wave components to short wave components. This energy transfer results in the continuous growth of the dispersed waves. The growing waves are then subject to the nonlinearity which results in the larger waves travelling faster, hence the largest leads the packet and the distance between two successive waves (the wavelength) increases with time.

These waves are not solitons at their present stage of evolution. The question is whether they will develop into solitons. In order to answer this, the mKdV equation was solved for a long evolution time of 100000s starting from a very localized initial depression. The result is shown in figure ??. When the first crest, which is continuously growing, reaches the undisturbed height, the first depression appears to separate from the rest of the waves, forming a soliton. Eventually, the depression

will evolve into a finite number of solitons followed by a wave train. This is known to happen for a finite depression of sufficiently small volume (Gardner *et al.* [1967]). It is clear now that the reason for solitons not appearing in our results is that the time needed for solitons to evolve from our initial conditions is very large. We can not afford such long runs with the primitive equation model.

The derived mKdV theory describes the observed evolution quite well, at least for waves with a scaled amplitude up to $\epsilon = 0.04$. There is good quantitative agreement between the mKdV theory and the model. The mKdV equation is much better than the KdV equation which is only good for waves up to $\epsilon = 0.02$ and is sensitive to $\alpha^{1.0}$. The agreement between the KdV and the model for waves with $\epsilon = 0.02$ indicates that the second order nonlinearity is not crucial for small waves.

When $\epsilon = 0.07$, the KdV equation completely fails, while the mKdV is still good for predicting the wave front and the first ripple. This is due to the fact that for large waves, higher order terms in the asymptotic expansion become more important. Adding extra terms to our theory should improve the comparison.

The disagreement between the mKdV and the model is most apparent at the trailing edge of the undular bore where the mKdV waves go out of phase with the model waves and have larger amplitudes. This is most evident when $\epsilon = 0.07$. The detailed comparison suggests that this is not due to the difference in propagation speed

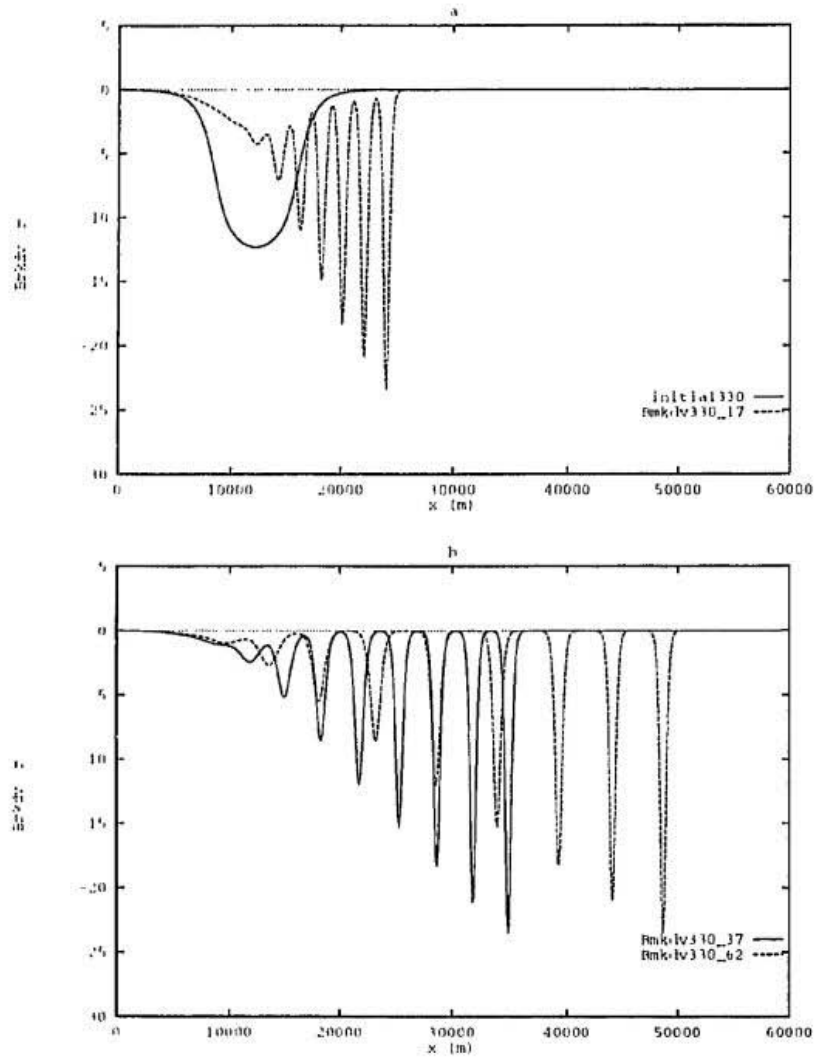

Figure 4.41: Solitons evolving from a localized depression. (a). mKdV waves at the initial stage and at 27200s. (b). mKdV waves at 59200s and 99200s. Obviously, the initial wave shown in (a) has now developed into solitons.

which is less than the measuring error. It seems that the difference in wavelength is most responsible for the discrepency. The wavelength difference from the model may be a result of inappropriate nonlinear-dispersive balancing, leading to differences in the group velocities of the theoretical and model waves. This can cause a theoretical wave to start dispersing longer/shorter waves at an earlier/later time than the model. As for the larger amplitudes at the bore tail, this could also be due to the nonlinear-dispersive balancing.

Koop & Butler [1981] experimentally tested the existing theories of finite amplitude internal solitary waves in terms of wave shape and amplitude-wavelength scale relationship in a two fluid system. Their results show that the KdV equation predicts the right shape and amplitude-wavelength scale relationship up to $\epsilon = 0.033$, while the mKdV extends the range to $\epsilon = 0.13$ (Their amplitude ϵ is actually scaled by the stratified depth h, which is now transformed to that scaled by the total depth H.). Segur & Hammack [1982] also investigated the KdV theory through experiments in a two fluid system, with focus on the solitary solution of the theory. Their finding is again that the KdV predicts the right shape and amplitude-wavelength scale relationship up to $\epsilon = 0.02$.

These investigations were conducted only for the steady solitary waves and in terms of the shape and amplitude-wavelength relation, while our comparisons are

for time dependent solutions of the mKdV theory. The question is whether the confirmed validity range of the theory for the steady solution is also applicable to the time evolution.

Our wave $B(t,x)$, with a typical initial front length of over 10 km and wavelength in the undular bore about 1 km, confined in a vertical extent of 360 m, certainly falls within the categary of the shallow water configuration, within which the mKdV/KdV theory is derived. The amplitudes considered are $\epsilon \approx 0.02, 0.04$ and 0.07. The confirmed KdV/mKdV validity range is 0.02/0.04, but the actual range is expected to extend to somewhere between $(0.02, 0.04)/\ (0.04, 0.07)$. Obviously, our KdV validity range is almost the same as those confirmed by the above authors, while the mKdV validity range appears to be smaller than that given by Koop & Butler [1981].

When rotation is taken into account, the earlier evolution of the wave front is significantly affected because long wave dispersion reduces the amplitude of the front. The front is smoother and dispersion begins later than in nonrotating cases. Rotational effects will become unimportant at the later evolution stage of the front after it becomes sufficiently steep. Therefore, our non-rotating theory can be applied to the front during its later evolution, and the result is in good agreement with the model.

Chapter 5

Summary and Conclusion

The purpose of this work is to compare the evolution of an initial isopycnal depression obtained from a fully nonlinear numerical model with the prediction of weakly nonlinear theory. The physical situation in mind is vertically trapped IGW packets occurring in the ocean. Idealized ocean conditions are considered, i.e., a constant depth, an inviscid, incompressible Boussinesq fluid, vertically uniform mean flows and simple stratifications. These enable us to concentrate on our goal.

In such an environment, the evolution of IGWs from the state of rest is simulated by Lamb's fully nonlinear numerical model. Undular bores are obtained, which are similar to those observed in the ocean by many authors. For the same governing equations, by the method of asymptotic expansion, a mKdV theory is derived

following Lee & Beardsley [1974].

In the weakly nonlinear theory, the temporal and horizontal variation of the wave is described by a wave profile $B(t,x)$. $B(t,x)$ is determined by a set of parameters $\alpha^{i,j}$ which are the multipliers appearing in vertical mode functions. In this thesis we have chosen to estimate $B(t,x)$ from the first two terms (first and second order in amplitude) of the asymptotic expansion (4.2) for the density perturbation. Thus B varies with $\alpha^{1,0}$ and with depth, since the coefficients of B and B^2 in (4.13) depend on depth. The KdV and mKdV equations are approximate evolution equations for this approximate wave profile B. The evolution of the wave predicted by the KdV equation is quite sensitive to $\alpha^{1,0}$ since B depends on $\alpha^{1,0}$ and the nonlinear term depends on B. The mKdV equation on the other hand is much less dependent on $\alpha^{1,0}$. The variation of the mKdV equation with changes in $\alpha^{1,0}$ partially compensates for the changes in B. Because of this the evolution predicted by the mKdV equation is much less sensitive to $\alpha^{1,0}$. Hence, the mKdV equation is more accurate than the KdV equation.

In previous research involving comparisons of IGW evolution (e.g., Lee & Beardsley [1974] , Liu *et al.* [1985], etc.), the second-order-accurate mKdV equation has been used, but the compared waves are usually only first-order-accurate in ϵ, i.e., B is obtained from $\eta_a = B\phi$. The error involved could be large since B approximated from

$\eta_d = B\phi$ could be much less accurate than that obtained by using $\eta_d = B\phi + B^2 P^{1,0}$.

In this work, the extracted wave $B(t,x)$ used for the comparisons is second-order accurate in ϵ. To ensure such a wave, a semi-infinite range of $\alpha^{1,0}$ is found, with a critical value $\alpha_c^{1,0}$ as an upper bound. It has been shown that any $\alpha^{1,0}$ which is not too large and around $\alpha_c^{1,0}$ can be selected. It is difficult to find a lower bound for $\alpha^{1,0}$.

Comparisons are made between the model results and the mKdV/KdV theoretical wave patterns by specifying a common initial state. The main results of the comparisons are:

i. The theory reproduces the nonlinear evolution of ICWs from an initial state, with most of the features in good quantitative agreement with the model results, e.g., the steepness of the front, the number of significant ripples in the bore, the phase and amplitude of the first few ripples and the nonlinear propagation speed, etc.

ii. The KdV equation adequately describes the evolution of a wave for ϵ up to about 0.02.

iii. The mKdV equation significantly improves on the KdV equation, especially for large waves. The validity range of the mKdV equation can be extended up to somewhere with ϵ between $0.04 \sim 0.07$.

iv. The theoretical waves can have longer or shorter wavelengths than the model

waves. This accounts for the waves being out of phase at the tail of the undular bore in comparisons. Another problem is larger theoretical amplitudes at the bore tail. Both could be a result of inappropriate nonlinear-dispersive balancing of the theory.

v. A localized depression of small size will develop into a finite number of solitons followed by an oscillating wave train after a long time evolution.

vi. Rotation is important in the early stage of the wave evolution because long wave dispersion reduces the size of the wave front. At later stages when the front is steep, this effect on the front disappears. Long waves trail the front.

vii. The mKdV equation is applicable in the rotating case near the wave front after the wave front is sufficiently steep, at least for the time scale considered here (after a very long time, more long waves will disperse out and this will ruin the agreement).

viii. When a hyperbolic stratification approaches a stepwise one, there is no sudden change in flow patterns.

Apparently, in order to further improve the mKdV theory for larger waves, higher order terms should be included in the theory. In the present study, the terms which are most needed have not been identified.

Bibliography

Apel, J. R., Holbrook, J. R., Liu, A. K. and Tsai, J. J. 1985. The Sulu Sea internal soliton experiment. *J. Phys. Oceanogr.*, 15: 1625-1651.

Bell, J. B., Solomon, J. M., and Szymczak, W. G. 1989b. A second-order projection method for the incompressible Navier-Stokes equations on quadrilateral grids. *AIAA 9th Computational Fluids Dynamics Conference*, Buffalo, NY, June 14-16, 1989.

Bell, J. B., and Marcus, D. L. 1992. A second-order projection method for variable density flows. *J. Comp. Phys.*, 101: 334-348.

Benjamin, T. B. 1966. Internal waves of finite amplitude and permanent from. *J. Fluid Mech.*, 25: 241.

Benney, D. J. 1966. Long nonlinear internal waves in fluid flows. *J. Math. Phys.*, 59: 187-199.

Chereskin, T. K. 1983. Generation of internal waves in Massachusetts Bay. *J. Geophys. Res.*, 88, C4: 2649-2661.

Colella, P. 1990. Multidimensional upwind methods for hyperbolic conservation laws. *J. Comp. Phys.*, 87: 171-200.

Cummins, P. F., and LeBlond, P. H. 1984. Analysis of internal solitary waves observed in Davis Strait. *Atmosphere-Ocean*, 22, (2): 173-192.

Farmer, D. M., and Smith, J. D. 1980a. Tidal interaction of stratified flow with a sill in Knight Inlet. *Deep Sea Res.*, 27A: 239-254.

Farmer, D. M., and Smith, J. D. 1980b. Generation of lee waves over the sill in Knight Inlet. *Fjord Oceanography*, edited by H. J. Freeland, D. M. Farmer, and C. D. Levings, pp. 259-269, Plenum, NY.

Fornberg, B., and Whitham, G. B. 1978. A numerical and theoretical study of certain non-linear wavephenomena. *Philos. Trans. R. Soc. London, Ser. A.*, 289: 373-404.

Gardner, C. S., Green, J. M., Kruskal, M. D., and Miura, R. M. 1967. Method for solving the Korteweg-de Vries equation. *Phys. Rev. Lett.*, 19: 1095.

Gear, J. A., and Grimshaw, R. 1983. A second-order theory for solitary waves in shallow fluids. *Phys. Fluids*, 26: 14-29.

Golub, G. H., and Van Loan, C. F. 1989. *Matrix Computations. Second Edition.* pp. 170-171. The Johns Hopkins University Press.

Halpern, D. 1971a. Observations on short period internal waves in Massachusetts Bay. *J. Mar. Res.*, 29: 116-132.

Halpern, D. 1971b. Semidiurnal internal tides in Massachusetts Bay. *J. Geophys. Res.*, 76: 6573-6583.

Haury, L. R., Briscoe, M. G., and Orr, M. H. 1979. Tidally generated internal wave packets in Massachusetts Bay. *Nature*, 278: 312-317.

Hibiya, T. 1986. Generation mechanism of internal waves by tidal flow over a sill. *J. Geophys. Res.*, 91, C6: 7697-7708.

Hibiya, T. 1988. The generation of internal waves by tidal flow over Stellwagen Bank. *J. Geophys. Res.*, 93, C1: 533-542.

Holloway, P. E. 1987. Internal hydraulic jumps and solitons at a shelf break region on the Australian North West Shelf. *J. Geophys. Res.*, 92, C5: 5405-5416.

Houghton, D. D. 1969. Effect of rotation on the formation of hydraulic jumps. *J. Geophys. Res.*, 74, C6: 1351-1360.

Koop, C. G., and Butler, G. 1981. An investigation of internal solitary waves in a two-fluid system. *J. Fluid Mech.*, 112: 225-251.

Korteweg, D. J., and G. de Vries. 1895. On the change of form of long waves advancing in a rectangular canal and on a new type of long stationary waves. *Phil. Mag., Ser. 5*, 39: 422.

Kubota, T., Ko, D. R. S., and Dobbs, L. D. 1978. Propagation of weakly nonlinear internal waves in a stratified fluid of finite depth. *A.I.A.A. J. Hydronautics*, 12: 157.

La Violette, P. E., Johnson, D. R., and Brooks, D. A. 1990. Sun-glitter photographs of Georges Bank and the Gulf of Maine from the space shuttle. *Oceanography*, April, 1990.

Lamb, K. G. 1993a. Numerical simulations of stratified, inviscid flow over a smooth obstacle. *J. Fluid Mech.* In press.

Lamb, K. G. 1993b. Numerical experiments of internal wave generation by strong tidal flow across a finite-amplitude bank edge. *J. Geophys. Res.* In press.

Lee, C. Y., and Beardsley, R. C. 1974. The generation of long nonlinear internal waves in a weakly stratified shear flow. *J. Geophys. Res.*, 79: 453-462.

Liu, A. K., Holbrook, J. R., and Apel, J. R. 1985. *J. Phys. Oceanogr.*, 15: 1613-1624.

Loder, J. W., Brickman, D., and Horne, E. P. W. 1992. Detailed structure of currents and hydrography on the northern side of Georges Bank. *J. Geophys. Res.*, 97: 14331-14351.

Long, R. R. 1956. Solitary waves in one- and two-fluid systems. *Tellus*, 8: 460.

Long, R. R. 1965. On the Boussinesq approximation and its role in the theory of internal waves. *Tellus*, 17: 46.

Long, R. R. 1972. The steepening of long, internal waves. *Tellus*, 24: 88.

Maxworthy, T. 1979. A note on the internal solitary waves produced by tidal flow over a three dimensional ridge. *J. Geophys. Res.*, 84: 338-346.

Ono, H. 1975. Algebraic solitary waves in stratified fluids. *J. Phys. Soc. Japan*, 39: 1082.

Osborne, A. R., and Burch, T. L. 1980. *Science*, 208: 451-460.

Ostrovsky, L. A., and Stepanyants, Y. A. 1989. Do internal solitons exist in the ocean? *Reviews of Geophysics*, 27: 293-310.

Rayleigh, Lord (J. W. Strutt). 1876. On waves. *Phil. Mag., Ser. 5*, 1(4): 257-279.

Sandstom, H., and Elliott, J. A. 1984. Internal tide and solitons on the Scotian Shelf: A nutrient pump at work. *J. Geophys. Res.*, 89: 6415-6426.

Scott Russell, J. 1837. Report on waves. p. 417, Rep. of the Brit. Ass., London.

Scott Russell, J. 1844. Report on waves. p. 311, Rep. of the Brit. Ass., London.

Segur, H., and Hammack, J. L. 1982. Soliton models of long internal waves. *J. Fluid Mech.*, 118: 285-304.

Smyth, N. F., and Holloway, P. E. 1988. *J. Phys. Oceanogr.*, 18: 947-962.

Stokes, G. G. 1847. On the theory of oscillatory waves. *Trans. Cambridge Phil. Soc.*, 8: 441.

Stokes, G. G. 1880. Supplement to 'On the theory of oscillatory waves'. *Mathematical and Physical Papers 1*, p. 314, Cambridge University Press, London.